EMT model and dynamic power management strategy of an offshore renewable energy hub with local power-to-gas conversion

Jane Marchand

TU Delft

EMT model and dynamic power management strategy of an offshore renewable energy hub with local power-to-gas conversion

by

Jane Marchand

A thesis submitted in partial fulfilment of the requirements for the degree of
Master of Science
in **Sustainable Energy Technology**
at the Delft University of Technology,
to be defended publicly on August 25, 2021 at 9:00 AM.

Student number:	5111250		
Project duration:	November 16, 2020 – August 25, 2021		
Thesis committee:	Dr. ir. J. L. (José) Rueda Torres,	IEPG	Mentor and chairman of the defence
	Dr. A. (Aleksandra) Lekić,	IEPG	Supervisor
	Dr. J. (Jianning) Dong,	DCE&S	External committee member
	Dr. J. (Jochen) Cremer,	IEPG	Committee member
Daily supervisor:	MSc A. (Ajay) Shetgaonkar	IEPG	

This thesis is confidential and cannot be made public until August 25, 2023.

TU Delft Delft University of Technology

Acknowledgement

First and foremost, I would like to thank my supervisor José, who believed in my abilities to tackle the topic of this thesis. He provided me with a lot of support and feedback all along the thesis, and he was always available when necessary. I would also like to thank Aleksandra, who offered wise guidance during the thesis and until the end. My daily supervisor, Ajay, who spent a lot of time helping me in the most hopeless moments of the thesis, deserves a lot of gratitude. Together, Aleksandra and Ajay answered many of my questions. I also owe a large part of my newly acquired knowledge to Arcadio, whom I would like to warmly thank for his unconventional explanations. I am very grateful to Remko too, for providing efficient technical help with the RTDS system at any time. This was extremely helpful for all the simulations I had to run.

Writing this thesis was not only a scientific exercise, it was also a life journey. I would like to thank many people for supporting me during this challenging, sometimes exhausting, but undoubtedly enriching experience: all my flatmates for their liveliness and kind words, José, Daniela, Sanghita, Federica, Andya, Franco, Vishaal for sharing the twists and turns of writing a master's thesis, Leonhard for proofreading my report and much more, Kirsten and Martijn for the relieving yoga classes, and also Priya, Vincent, Mathias, Ali, and the board members of Energy for Refugees.

Last but not least, I am extremely grateful to my parents for supporting me and being always there to listen to me.

Jane Marchand
Delft, August 2021

Abstract

Given the urgency to shift to a cleaner energy mix, offshore wind energy is bound to be quickly deployed on a large scale in the next years. In order to meet the Paris Agreement, the current role-out rate of wind energy in the North Sea, that is 2 GW/year, needs to be increased to an average value of 7 GW/year over the period 2023-2040. This rapid increase of the share of uncontrollable, renewable sources in the energy mix raises a certain number of challenges, among which sustaining energy balance and transient stability. To organise the large-scale deployment of offshore wind in a strategic manner, the concept of hub-and-spoke has been introduced. It envisages modular offshore renewable power generation clusters (a.k.a. offshore hubs) designed to be easily and safely operated and interconnected.

Dealing with large power fluctuations constitutes a major challenge for each offshore hub. To mitigate the variability of power supply, integration of offshore storage systems is an envisioned solution. Offshore power-to-gas conversion for storage purposes has been widely investigated in the literature, under techno-economic or power balance points of view. However, an in-depth analysis of the dynamic performance of the connection of large scale electrolysers in offshore hubs is urgently needed to ascertain the degree of effectiveness of this solution and to safeguard the stability of the hub.

This thesis proposes a real-time simulation model of a 2 GW offshore hub integrating electrolysers in order to investigate their impact on the dynamic active power management of the hub. Two locations for the connection of the large-size electrolysers are studied: i) connection of an electrolyser to the AC common bus of the hub and ii) connection of electrolysers to the DC link of the back-to-back converter of each Type-4 wind turbine of the hub. An Electromagnetic Transient (EMT) simulation based analysis, necessary to capture the fast dynamics of the zero-inertia hub, is performed under different severe disturbances, such as a three phase fault and sudden large wind speed fluctuations.

In a second part, the thesis investigates the connection of the hub to the shore via a bipolar High-Voltage Direct Current (HVDC) link. It has been shown in the literature that bipolar links are more reliable than monopolar ones, as they can still be operated to transfer half of their nominal capacity in case of failure of one cable or converter. However, a method is needed to allocate the generated power among the converters constituting the offshore terminal of the link, according to the needs of the operator (e.g. planned maintenance). The work of this thesis is focused on developing and implementing a power sharing strategy between the two Modular Multi-level Converters (MMCs) constituting the offshore terminal of the link. The power sharing control has been implemented in one of the two offshore MMCs, and can be done using DC voltage or DC current measurements, as well as using a predefined power sharing set-point as input.

Numerical results obtained by EMT simulations show that an effective mitigation of sudden active power imbalance can be achieved by placing the electrolyser locally at each wind turbine, or centrally at the common bus of the hub. In case of fault within the hub, e.g. a three phase short circuit near a wind turbine, the connection of an electrolyser to the DC link of the wind turbines (through a buck converter) is convenient to prevent loss of wind power generation due to the islanding of the turbine.

Regarding the power sharing in the HVDC link, it was observed that in comparison with the strategy based on measured DC voltage, the power sharing based on measured DC current is more effective, faster, and less prone to cause collateral effects (such as undesirable oscillations of DC voltage and current) which jeopardise the stable operation of the link.

Contents

List of Figures vi

List of Tables ix

List of abbreviations x

1 Introduction 1
1.1 Background and Motivations . . . 1
1.2 Literature Review . . . 3
1.2.1 Electrolyser EMT model and integration into the hub . . . 3
1.2.2 Offshore-Onshore HVDC Interconnection . . . 3
1.3 Objectives and Research Questions . . . 4
1.4 Thesis Contributions . . . 5
1.5 Thesis Outline . . . 6

2 Modelling Aspects and Related Background 8
2.1 RSCAD Environment . . . 8
2.1.1 RMS Vs EMT Simulations . . . 8
2.1.2 Hardware and Software . . . 9
2.2 Baseline Model: Topology and Components . . . 10
2.2.1 Topology . . . 10
2.2.2 PMSG . . . 12
2.2.3 MMC . . . 13
2.2.4 Electrolyser . . . 14
2.2.5 Cables and Voltage Levels . . . 14
2.2.6 Connection to the Main Grid . . . 15
2.3 Control Structures Implemented in the Network . . . 15
2.3.1 MSC . . . 15
2.3.2 GSC . . . 15
2.3.3 MMC . . . 15

3 Investigation of the Impact of Electrolysers on the Dynamics of the Offshore Hub 19
3.1 Literature Review . . . 19
3.1.1 Electrolysers Potentialities in Supporting the Network . . . 19
3.1.2 Sizing and Location of the Electrolysers . . . 20
3.2 Investigation Option C1: Connection on the DC links of the Wind Turbines . . . 20
3.2.1 DC link Topology . . . 20
3.2.2 Modelling of the DC-DC Converter . . . 21
3.2.3 Controls . . . 26
3.2.4 Results . . . 30
3.3 Investigation Option C2: Connection on the AC Common Bus . . . 34
3.3.1 Model Topology and Sizing . . . 35
3.3.2 Scaling . . . 37
3.3.3 Control . . . 37
3.3.4 Results . . . 39
3.4 Conclusion . . . 43

4 Development of a Control Strategy for the Offshore-Onshore HVDC Bipolar Link 44
4.1 Literature Review . . . 44
4.2 Upgrade of the Offshore-Onshore HVDC Link to a New Topology . . . 44
4.2.1 Use of a Point-to-Point Bipolar HVDC Link . . . 44
4.2.2 Addition of Onshore MMCs . . . 45

4.3 Control Strategies for the Outer Active Current Loop of MMC-2 . . . 47
4.3.1 Active and Reactive Current (i_d/i_q) Decoupling . . . 47
4.3.2 Direct Power Control and DC Current Control . . . 49
4.3.3 DC Voltage Control . . . 50
4.4 Investigation of the Performance of the Two Control Strategies . . . 53
4.4.1 Wind Speed Variation . . . 53
4.4.2 Active Power Sharing and Unloading of One Pole . . . 54
4.4.3 HVAC Fault . . . 56
4.4.4 Conclusion . . . 57

5 Conclusion 59
5.1 Summary of Findings . . . 59
5.2 Answers to the Research Questions . . . 60
5.3 Future Work . . . 60

Appendices 63

A Guidelines to Initialise and Run the Simulation Files 63
A.1 Simulation Folders and Files . . . 63
A.2 Basic Simulation . . . 64
A.3 Simulation With Wind Speed Profile . . . 66

B PWM in RSCAD 69

C Anti-Windup Mechanism 70

D Generation of Reference Wind Speed Profiles 71

E Racks, Subsystems and Core Assignment in RSCAD 73
E.1 Racks and Subsystems . . . 73
E.2 Core Assignment . . . 73

F MSC Control Scheme 76

G GSC Control Scheme in the Case of Electrolyser Connected to the DC Link of the Wind Turbine 78

Bibliography 80

List of Figures

1.1 Global renewable and wind energy installed capacity in 2019 (Data from [3]) . . . 1
1.2 Challenges of modelling an offshore multi-energy hub . . . 2
1.3 Characteristics of the main DC topologies (the positive features at colored in purple, the negative ones in green) [11] . . . 4
1.4 Thesis workflow . . . 7

2.1 Voltage at PCC in an offshore network, computed with an RMS and an EMT model [27] . . . 9
2.2 Interface block between large time steps and small time steps models in RTDS . . . 9
2.3 RTDS Novacor chassis [28] . . . 10
2.4 RTDS setup [28] . . . 10
2.5 Single line diagram of the baseline model implemented in RSCAD [20] . . . 11
2.6 Hub-and-spoke layout envisioned by the NSWPH consortium [2] . . . 12
2.7 A PMSG wind turbine connected to the grid [29] . . . 12
2.8 Scale-up option in the property window of the small time-step/mainstep interface transformer 13
2.9 Difference in the structure of a 2-level VSC and a MMC half-bridge (only one phase is shown) [30] 13
2.10 MMC topology . . . 14
2.11 Electrolyser stack model in RSCAD . . . 14
2.12 DVC control scheme [20] . . . 16
2.13 Control hierarchy in an HVDC VSC multi-terminal converter (adapted from [32]) . . . 17
2.14 MMC-1 controller [20] . . . 18
2.15 Inner loop of the MMC-2 controller [20] . . . 18

3.1 Electrolysers flexibility compared to electricity market requirements [38] . . . 20
3.2 Different locations of the energy storage device (adapted from [14]). Only locations C2 and C3, highlighted in green, are considered in this thesis. Location C1 was meant for another WT technology, and location C4 was not relevant for an offshore hub. . . . 21
3.3 Connection of four electrolysers on the DC link of the WTs . . . 21
3.4 Switch model in large time-step (1), small time-step (2) and substep (3) in RSCAD (adapted form [42]) (A)=Switch ON / (B)=Switch OFF . . . 22
3.5 Reference circuit of the buck converter (a) and its equivalent circuits according to the state of the switch: switch ON (b) or switch OFF (c) . . . 23
3.6 DC-DC converter and electrolyser model in RSCAD, connected to the DC link of a WT as shown in figure 3.3 . . . 25
3.7 Time response of the buck converter when increasing the switching frequency from 1 to 2 kHz . 26
3.8 Control of the expanded DC link and measurement points . . . 26
3.9 Effect of a wind speed drop on the DC-link voltage of one of the WTs in the baseline model . . . 27
3.10 Chopper schematic and control structure in the case of connection of an electrolyser to the DC link . . . 28
3.10 Chopper schematic and control logic, in the case of connection of an electrolyser to the DC link (cont.) . . . 29
3.11 Buck converter controller . . . 29
3.12 Wind speed input in RSCAD . . . 30
3.13 Time response of DC links 1 and 2 having two different time constants (0.02 s for Ely 1 and 0.01 s for Ely 2) in the inner loop PI, under wind speed step from 9 to 14 m/s . . . 31
3.14 Time response of the DC link of WT-1 under wind speed profile n°2, with electrolysers connected to the DC links of the WTs . . . 32
3.15 Location of the HVAC fault . . . 33
3.16 Time response of DC link 1 (graphs b and d) and DC link 2 (graphs c and e) under islanding due to three-phase fault on HVAC-1 (graph a) . . . 34

3.17 Connection of the electrolyser on the AC common bus of the hub . . . 35
3.18 Electrolyser model with its rectifier, buck converter and transformers, for connection to the AC bus of the hub . . . 35
3.19 Transmission line block and parameters in RSCAD draft file, interfacing subsystems n°1 and 3 . 36
3.20 Schematic of the damper in the interface transformer . . . 37
3.21 Control of the buck converter for the electrolyser connected to the AC common bus . . . 38
3.22 Tuning method of the cascaded PI controllers in the buck converter controller, using incremental variation of the time constant and gain values . . . 39
3.23 Hub response to a 1 MW power consumption step of the electrolyser connected to the common bus . . . 40
3.24 Hub response to a wind speed step from 11 to 15 m/s, with an electrolyser connected to the common bus . . . 41
3.25 Hub response to a the wind speed profile n°2, with an electrolyser of capacity 800 MW connected to the common bus . . . 42

4.1 Common HVDC topologies (adapted from [11]) . . . 45
4.2 Implemented topology of the HVDC link . . . 46
4.3 RSCAD component used to model the Alternative Current (AC) source representing an equivalent of an onshore power system ($R = 1.0\Omega$), and its property window . . . 46
4.4 Summary of the distribution of the different parts of the network among the NocaCor chassis . 47
4.5 Outer and inner loop control scheme . . . 48
4.6 Selector for MMC-2 outer loop in Runtime . . . 49
4.7 Outer loop of MMC-2 for AC power control (in green) or DC current control (in orange) modes . 49
4.8 MMCs time responses when operating under I_{DC} and P_{AC} control strategies for active current reference generation in MMC-2, under wind speed downward step from 15 to 10 m/s . . . 50
4.9 Outer loop of MMC-2 for DC voltage control mode . . . 51
4.10 Power-Voltage graph for MMC-2 control . . . 52
4.11 Flowchart of the generation process for the P-V graph used in the V_{DC} control method (WS = *Wind Speed*) . . . 52
4.12 MMCs time responses when operating under I_{DC} and V_{DC} control strategies, under a wind speed step from 10 to 15 m/s . . . 53
4.13 MMCs time responses when operating under I_{DC} and V_{DC} control of MMC-2, under unloading of MMC-1, at constant wind speed of 10.5 m/s . . . 54
4.14 MMCs time responses when operating under I_{DC} and V_{DC} control of MMC-2, under re-loading of MMC-1, at constant wind speed of 10.5 m/s . . . 55
4.15 P Vs V_{DC} trajectory when re-loading MMC-1 with a step set-point. The green arrows indicate the evolution of the trajectory in time . . . 56
4.16 Location of the applied fault on HVAC-1 . . . 57
4.17 MMCs time response under three-phase fault on HVAC cable 1, at constant wind speed of 16 m/s 57

A.1 The three simulation folders . . . 63
A.2 Connection to the TU Delft ESP lab VPN . . . 64
A.3 RSCAD software icon . . . 64
A.4 RSCAD software window . . . 64
A.5 Draft (.dft) file tool bar . . . 65
A.6 Running the initialisation script in the Runtime (.sib) file . . . 65
A.7 Process to follow to run the simulation in RSCAD . . . 66
A.8 Selection of the wind profile in the draft (.dft) file . . . 67
A.9 Modification of the plotting time in the Runtime (.sib) file in RSCAD . . . 68
A.10 Starting the reading of the wind profile data in the Runtime (.sib) file in RSCAD . . . 68

B.1 PWM in RSCAD - (A) Two-switch system (B) Triangular and modulation waves (C) Output voltage (D) Triangular wave and firing pulse generators in RSCAD .dft file (adapted from [42]) . . . 69

C.1 PI controller with limited output and back-calculation anti-windup mechanism . . . 70

D.1 Location 51.95926N 2.94236E for the wind speed data . . . 71

D.2 Graphs of the wind speed scenarios 72
D.3 Scheduler component in the draft (.dft) file in RSCAD 72

E.1 RTDS racks used to run the simulation and corresponding part of the network assigned to each rack, in the model implementing electrolysers on the DC links of the WTs 74
E.2 RTDS racks used to run the simulation and corresponding part of the network assigned to each rack, in the model implementing an electrolyser on the AC bus of the hub 74
E.3 Core assignment for the model implementing an electrolyser on the AC common bus of the hub 75

F.1 Control scheme of the MSC in the baseline model [20] 77

G.1 Adapted control logic for the active power control in the outer loop of the GSC in the case of electrolyser connected to the DC link 79

List of Tables

3.1 Control parameters used for the simulation (unless stated otherwise). Parameters related to the buck converter, Grid Side Converter (GSC) and chopper can be visualised in figure 3.11, G.1 and 3.10 respectively. 30
3.2 Summary of the main parameters used in the electrolyser system model 38

D.1 The three selected wind speed samples 71

List of abbreviations

AC Alternative Current.

BoP Balance of Plant.

CapEx Capital Expenditure.

DC Direct Current.

DVC Direct Voltage Control.

EMT Electromagnetic transients.

ESP Electrical Sustainable Power.

GSC Grid Side Converter.

HVAC High Voltage Alternative Current.

HVDC High Voltage Direct Current.

IGBT Insulated-Gate Bipolar Transistor.

LCC Line-Commutated Converter.

MMC Modular Multi-level Converter.

MPPT Maximal Power Point Tracker.

MSC Machine Side Converter.

MTDC Multi-Terminal Direct Voltage.

NSWPH North Sea Wind Power Hub.

OpEx Operational Expenditure.

P2G Power-to-Gas.

PCC Point of Common Coupling.

PEM Proton Exchange Membrane.

PI Proportional Integral.

PLL Phase Lock Loop.

PMSG Permanent Magnet Synchronous Generator.

PWM Pulse-Width Modulation.

RMS Root Mean Square.

RTDS Real Time Digital Simulator.

TSO Transmission System Operator.

VPN Virtual Private Network.

VSC Voltage-Sourced Converter.

WT Wind Turbine.

1

Introduction

This chapter gives an overview of the motivation, scope, overall approach and contributions of this thesis. The main research gaps from existing related literature are summarized, whereas a more elaborated literature review is provided at the beginning of each subsequent chapter.

1.1. Background and Motivations

In order to meet Paris Agreement [1] and limit global emissions, we need to accelerate the shift of electricity production to cleaner sources. Wind energy is already largely contributing to this clean energy mix as it represents one fourth of the global renewable energy capacity, as shown in figure 1.1, and is bound to increase in the near future. Among this production, offshore wind energy accounts for 4.5 % in terms of installed capacity. Offshore production has several advantages, such as less land use and better opportunities to benefit from high wind speeds. Hence researchers, along with Transmission System Operator (TSO)s, are focusing on planning the roll-out of large scale offshore energy hubs. For instance, the North Sea Wind Power Hub (NSWPH) consortium specifically aims at managing this roll-out, as stated in [2].

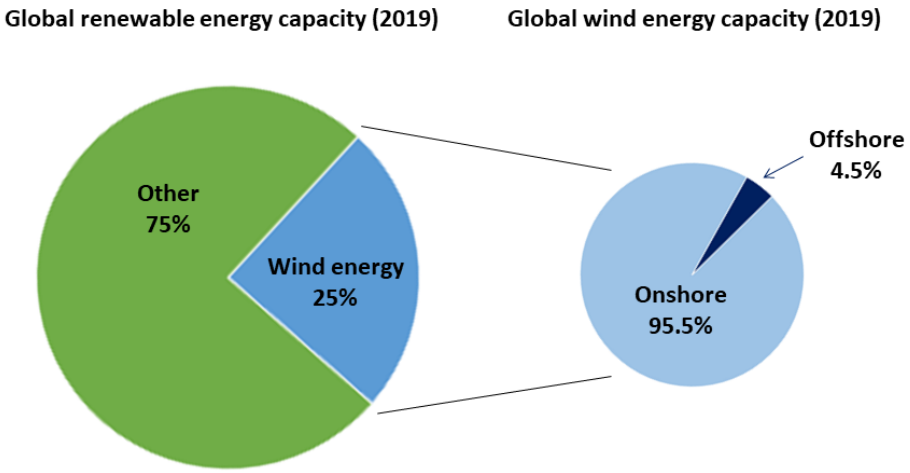

Figure 1.1: Global renewable and wind energy installed capacity in 2019 (Data from [3])

This progressive but swift deployment of intermittent renewable sources ineluctably calls for a matching deployment of storage solutions, in order to continue to ensure security of supply of electricity all day long and all year round. Along with large scale offshore wind hubs comes the topic of large scale seasonal storage. One of the most feasible and investigated option for such long-term storage is the power-to-gas solution, as can be read in [4]. For example, part of the offshore power could be converted into hydrogen, stored in tanks

or salt caverns [5], and either used as such or converted back into electricity when needed. Multiple studies reveal that in such a scenario, directly converting the electricity into hydrogen offshore is beneficial: complete analysis were carried out in [6] and [7], highlighting economical advantages, social acceptance, flexibility for TSOs and offshore large scale gas storage option. Other studies focus on one advantage, such as economic benefits [8] or geological storage potential [9].

Another advantage of producing hydrogen offshore is that electrolysers can provide ancillary services to the offshore hub, as investigated in [10]. Because offshore energy hubs are zero-inertia networks, they are very vulnerable to disturbances. Ancillary services such as frequency and voltage support are of great importance in this kind of networks. Large scale multi-MW electrolysers, along with their converters and appropriate control functions, could become a provider of such services in an offshore hub.

Furthermore, the roll-out of such large production units needs to be organized wisely in order to serve the network as best as possible in the future. The approach of the NSWPH consortium is to organise wind turbines into hubs connected to the shore and interconnected between each other. In this configuration, the high voltage transmission links connecting the offshore hubs to the shore will be key elements. The choice of High Voltage Direct Current (HVDC) links for transmission of power from offshore wind farms has become the preferred option, since this technology has been proven to be more fit than High Voltage Alternative Current (HVAC) for long-distance, bulk transfer of power. Mainly, it generates less losses and has the potential to offer embedded provision of ancillary services, which can be used to manage fast power fluctuations and different types of disturbances [11]. In the following section, a concise literature review has been carried out to determine which type of HVDC link would be more suitable in the present case.

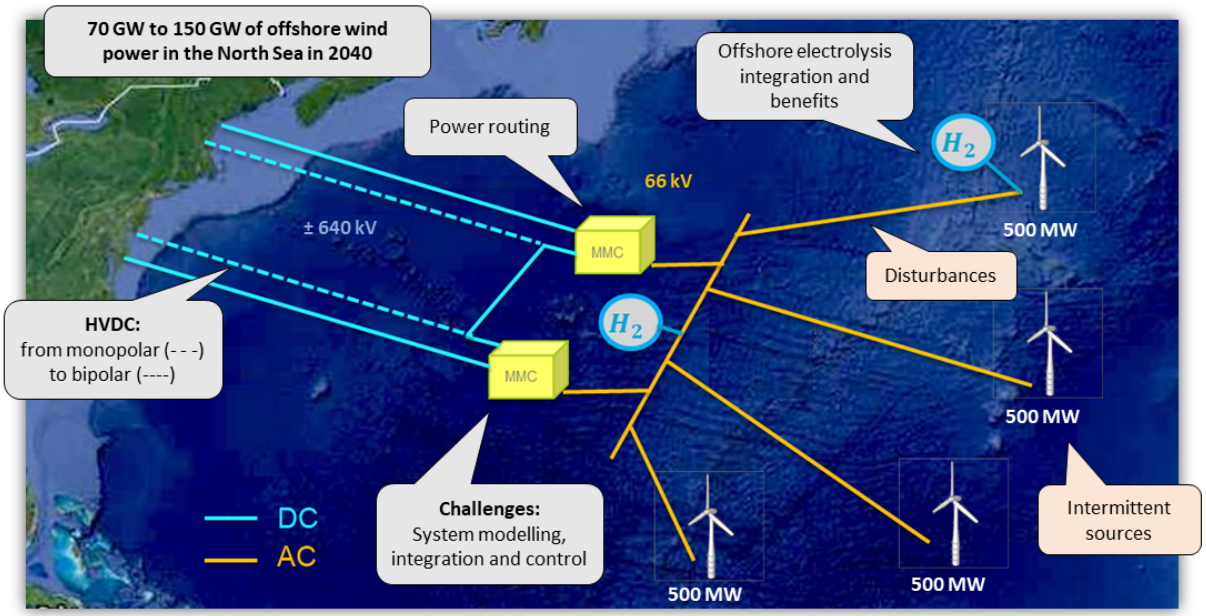

Figure 1.2: Challenges of modelling an offshore multi-energy hub

A hub implementing the features described above would look like the one pictured in figure 1.2. However, in practice, there is a lack of real-time simulation models available which implement bipolar Voltage-Sourced Converter (VSC)-HVDC links and/or offshore electrolysers, and which aim at analysing the impact of disturbances (such as three-phase short circuits and sudden wind speed variations). The following section presents a review of the most recent existing offshore HVDC and electrolyser Electromagnetic transients (EMT) models, and highlights the gap between those models and the aim of the present work.

1.2. Literature Review

1.2.1. Electrolyser EMT model and integration into the hub

Electrolyser EMT Models

In spite of the multiple studies claiming the benefits of offshore electrolysers, no plug-and-play model was found of an electrolyser stack, with its converters and controllers, which could be connected to an offshore hub in RSCAD.
In [12], the first EMT model of a multi-MW scale electrolyser for real-time simulation in RSCAD was developed for stability studies of onshore systems. In this model, the Proton Exchange Membrane (PEM) stack itself is modelled as a constant voltage source in series with a resistance. The stack is then connected to the grid through a buck converter (Direct Current (DC)-DC converter), a rectifier and a transformer. All those components are modelled in the small time step environment (cf. section 2.1). The Balance of Plant (BoP) components are modelled as a constant voltage source, representing a load of about 10 % of the total electrolyser power demand. The advanced control scheme implemented in [12] to monitor the electrolyser has two main objectives: maximizing the hydrogen production, and enabling ancillary services capabilities in a stable manner.
However, the above-mentioned model was tested under connection to a strong grid. In order to connect it to the zero-inertia offshore hub at stake in this thesis, the model had to be largely modified.

Electrolyser Integration into the Hub

Aside from the model development, the location of the conversion process in the energy transmission network should be considered. No studies on the physical performance based on detailed EMT models of a large scale electrolyser connected to an offshore hub have been reported so far. Some preliminary techno-economic studies have been done, using very simplified models and considering several possible locations for the conversion process, such as in [13]; some similar techno-economic studies considering various locations has been done in [14], with another type of energy storage, namely superconducting magnetic energy storage.

Parallel to model development, the first pilot projects of wind-turbine connected electrolysers are in progress. The first platform for offshore green hydrogen production has been commissioned in 2019 and is being built in the North Sea as part of the PosHYdon project [15]. Additionally, the first pilot project of a wind turbine (3 MW) connected to an electrolyser (400 kW) and capable of operating in islanded mode is currently being tested in Denmark, with the project Brande Hydrogen [16]. The effect of fluctuating power input on the operation of the electrolyser is one of the main stake of the study. Offshore hydrogen production is already a medium-term goal for the industry [17], full-scale wind turbine-integrated electrolyser demonstrators being planned for 2026 [18].

1.2.2. Offshore-Onshore HVDC Interconnection

HVDC Link Characteristics

Hereinafter a literature review of the main characteristics of state-of-the-art HVDC links is presented.

Among the HVDC technologies, VSC is preferred over Line-Commutated Converter (LCC) because it offers additional capabilities such as synthetic inertia or voltage control [11]. The Modular Multi-level Converter (MMC) is one particular topology of VSC, in which several hundreds of sub-modules are connected in series, therefore generating a sinusoidal voltage with low harmonic distortion [19]. The MMC topology also has other advantages, for example the possibility to control active and reactive power independently. It also offers black-start capabilities [19]. For these reasons, MMC has become the preferred technology for HVDC transmission system converters.

Furthermore, several topologies exist for VSC-HVDC links. The advantages and drawbacks of the main topologies are summarized in figure 1.3. As can be seen on the figure, monopolar configurations do not offer redundancy and therefore provide very low reliability of the network. In order to satisfy reliability criteria such as the N-1 criterion, the network should be duplicated, which would induce very high costs. On the contrary, true bipolar configurations (independent converters for each pole) ensure some redundancy in the network:

for example, the failure of one pole or converter still allows for the transmission of half the rated capacity via the other pole, since one pole can be operated independently of the other. The last column of figure 1.3 also highlights that bipolar configurations enable higher transmission capacity than monopolar configurations.

Topology	Costs	Redundancy (availability)		Environmental impact		Transmission capacity
		Line	Converter	Earth current	Number of lines	
Bipole	high	yes (medium/high)[6]	yes (medium)	low	high	high
Rigid bipole	medium	no (low)	yes (medium)	low	medium	high
Asymmetrical monopole (MR)	medium	no (low)	no (low)	low	medium	low
Asymmetrical monopole	low	no (low)	no (low)	high	low	low
Symmetrical monopole	medium	no (low)	no (low)	low	medium	low

Figure 1.3: Characteristics of the main DC topologies (the positive features at colored in purple, the negative ones in green) [11]

Models and Studies of Offshore Hubs

Many models for real-time simulation of HVDC links are present in the literature, but few of them gather the different requirements of this thesis.

One example of an HVDC link model is the model of a symmetrical monopole developed in RSCAD and presented in [20], which is also the baseline for the model developed in this thesis, even though it was upgraded to a bipolar topology. This model is further described in chapter 2.
In [21], a point-to-point, bipolar with dedicated metallic return HVDC link model has been developed in PSCAD for the purpose of fault discrimination. In [22] a bipolar two-level VSC-HVDC system is designed for voltage re-balancing after pole-to-ground fault. Recently, in [23], an EMT model of a 400 MW offshore hub is used to study black-start capabilities. The hub is connected to the shore via a ±320 kV monopolar HVDC link. Contrary to the model used in the present work, the offshore HVDC terminal is grid-following and the wind turbines are grid forming. Another difference is that the wind turbines DC link is modeled as a voltage source, and no dynamic operation (varying wind speed) are studied.

One open challenge is to achieve a controllable sharing of the power flowing through each MMC station, while ensuring the coordination between the different control modes (islanded or non-islanded modes). However, none of the studies found focuses on the power routing between the two poles of the bipolar link. This research gap is addressed in this thesis, by developing a strategy to flexibly manage the power flow in each pole according to the operator's needs, allowing for example to unload one of the pole in case of planned maintenance. This mode of operation, in which the current flowing in the positive and negative pole is not equal, is called asymmetric mode [24].

1.3. Objectives and Research Questions

The general objective of this thesis is to develop a model of a four Wind Turbine (WT) offshore hub which outstrips the latest models developed for this type of network as of today. This is done by building up on an existing model by adding power-to-gas conversion units (represented by electrolysers) and studying the transfer of the power from offshore to onshore.
First, several electrolysers are integrated to the model as a storage solution. Second, the connection between the offshore hub and the shore is modified, and the control strategy of the corresponding converters is also revised. The following research questions constitute the guidelines of this thesis work.

- **What are the major numerical issues which should be solved when connecting electrolysers at different locations of the hub to ensure a detailed and trustworthy simulation of the developed model, and how to solve them?**

Introducing variable loads (here electrolysers) can possibly generate instabilities and resonances in the network, depending on the location of the connection. Additionally, several representations of switches are available in RSCAD, and some of them might lead to flawed computation (e.g. unrealistic losses). Simulations have to be performed to track undesirable behaviours and if need be, adequate modifications should be implemented.

- **How can electrolysers contribute to manage challenging real-life conditions (e.g. three-phase faults or highly-fluctuating wind profiles), and what are their benefits according to the location where they are connected?**
  Typical challenging offshore real-life conditions can be for example three-phase faults or highly-fluctuating wind profiles. Beside the common wind speed step tests, the behaviour of offshore hubs should also be assessed under such real-life conditions. To this end, historical data were selected to represent the conditions of interest, such as a very high wind speed gradient. These wind profiles, as well as three-phase to ground short-circuit faults, are simulated in two different hub scenarios, corresponding to two different locations of the electrolysers. The potential of each scenario to support the network is then assessed.

- **What are the major drawbacks of a monopolar HVDC link between the offshore hub and the shore, and how to modify it to allow for reliable and flexible power exchange in the future?**
  Even if they have lower investment costs than bipoles, monopoles are not the best choice for HVDC links in terms of reliability and flexibility, and the potentialities of bipolar links are highlighted in the literature. In this thesis, the monopolar link implemented in the baseline model is changed to a bipolar link. To assess the stability of the new transmission link, two MMCs are connected to the shore side of the line and simulations are performed.

- **What is a conceptually simple and effective strategy to implement power sharing capabilities among the offshore converters?**
  The power flow in each of the two poles of the bipolar HVDC link connecting the offshore hub to the shore can be managed independently by the two offshore MMCs. Being able to control the link to operate in balanced conditions (same current in each pole), or to completely unload one of the poles for example, would allow for more flexibility regarding power transmission. During planned maintenance for example, one of the poles could be unloaded by the converters, thus reducing the use of massive DC breakers. Two types of power of such a power sharing strategy are developed in this thesis and implemented in offshore MMC-2. The two strategies are then compared under different scenarios.

A summary of the answers to the above-listed questions is provided in section 5.2.

1.4. Thesis Contributions

The main contributions of this thesis to the ongoing research in the field of study are listed below.

The first main contribution was the development in RSCAD of a generic model of a 2 GW offshore energy hub including offshore power-to-gas conversion, and a modelof the same hub including a bipolar HVDC link connecting the hub to the shore. An EMT simulation method has been chosen to capture the fast dynamics of the zero-inertia hub, with a view to the second contribution. More detailed contributions are:

- Implementation of a computationally efficient and accurate method to model the behaviour of an offshore-connected electrolyser, thanks to the substep environment in RSCAD;
- Upgrade of the hub model presented in [20], from monopolar HVDC link to bipolar HVDC link, and addition of two onshore MMCs.

The second contribution was to produce some analysis giving some insights about the dynamic performances of the hub under different scenarios and conditions. More detailed contributions are:

- Investigation of the influence of the location of the electrolyser(s) in the offshore hub (central or distributed location);
- Analysis of the hub performance under different wind speed patterns and fault scenarios.

The third contribution was the development and comparison of two power sharing strategies for the offshore MMCs, enabling the offshore terminal to operate in balanced conditions or to unload one of the poles.

- EMT simulation for the comparison of two different locations for the connection of an electrolyser in an offshore wind energy hub;
- Substep model in RSCAD of a PEM cell and its associated converter;
- RSCAD model of a bipolar point-to-point HVDC link ;
- Comparison of two control strategies enabling power sharing between the two offshore MMCs of a bipolar HVDC link.

1.5. Thesis Outline

This thesis is organised as follows:

- Chapter 2 contains a presentation of the digital tool used for the simulations, as well as a detailed summary of the baseline model which was used as the starting point for the present work. The main components of the model are described, along with their control strategies;
- Chapter 3 presents the research that has been done regarding the modelling and connection of a multi-GW electrolyser to the network. Two possible locations for the connection are investigated;
- Chapter 4 focuses on the HVDC link between the offshore hub and the shore. The link is first upgraded from a monopolar to a bipolar topology, after which different control strategies are developed and compared;
- Chapter 5 concludes this work by providing a summary of the main findings, as well as a short answer to each research question. Suggestions for future work are also given in this chapter.

After an initial learning part, the work has been divided into two main blocks: integrating electrolysers in the model, and implementing a new HVDC structure and control. Once those two tasks were achieved, the final model has been updated with the previous work, and a conclusion has been drawn.

The workflow of the thesis is represented in the flowchart visible in figure 1.4.

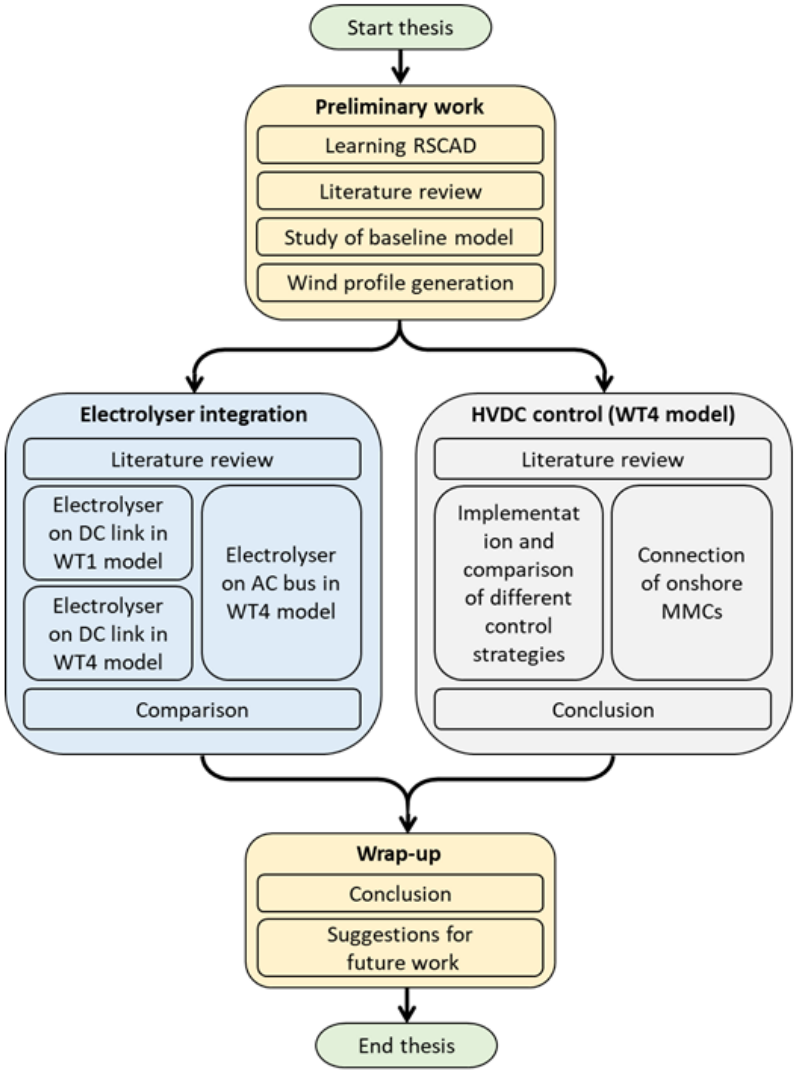

Figure 1.4: Thesis workflow

2

Modelling Aspects and Related Background

In this chapter, the real-time simulation software used in this thesis and the network on which the simulations is based are described. The model of the baseline network and its control strategies has been developed and explained in [20]. The model of the electrolyser and its converters has been developed on the basis of the work done in [12] and [25].

2.1. RSCAD Environment

In this section, a justification for the use of EMT simulations rather then Root Mean Square (RMS) simulations is given; the tool used to perform these simulations in the thesis is then introduced.

2.1.1. RMS Vs EMT Simulations

Two types of models can mainly be used to simulate power systems: RMS models and EMT models. These models present some differences and therefore the choice of one or the other needs to be considered carefully.

RMS models use a phasor simulation method, in which the network is simulated with fixed complex impedances instead of differential equations. It is an average model, convenient to study power system stability in the case of large interconnected systems, including electro-mechanical oscillations (small-signal stability), rotor-angle stability of synchronous generators and voltage and frequency stability. In this kind of models, the network is assumed to operate in perfectly balanced conditions, therefore only the positive sequence components is non-zero, so it is the only component considered. Fast switching transients, as well as controls with very small time constants, are ignored [26]. As a results, RMS simulations are able to model power exchanges accurately, but fail to capture the transients and dynamics after a fault [27].

EMT models solve the differential-algebraic equations representing a three phase electrical network (in the Real Time Digital Simulator (RTDS), the Dommel algorithm is used). Contrary to RMS models, they are able to capture the dynamics of zero-inertia or high inertia systems [27]. If electro-magnetic transients, frequency dependence of network components, harmonics, unbalanced networks, etc. are of interest, an EMT model should be used [26]. However, it should be noted that RMS models are much faster than EMT models, the latter ones often requiring excessive computational efforts [27].

As an illustration, the comparison of the analysis of an offshore wind hub connected to the shore via VSC-HVDC links with the two models has been conducted in [27]. The outage of one of the DC links has been simulated. Figure 2.1 clearly shows that the RMS model fails to detect the peak deviation and the hight frequency oscillations of the voltage at Point of Common Coupling (PCC). The same applies to the active power [27].

To conclude, since the fast transients are precisely the phenomena at stake in this thesis, the decision has been made to conduct the analysis necessary in this thesis with an EMT model. The RTDS tool, available at TU Delft, has been selected to perform the EMT simulations in real time.

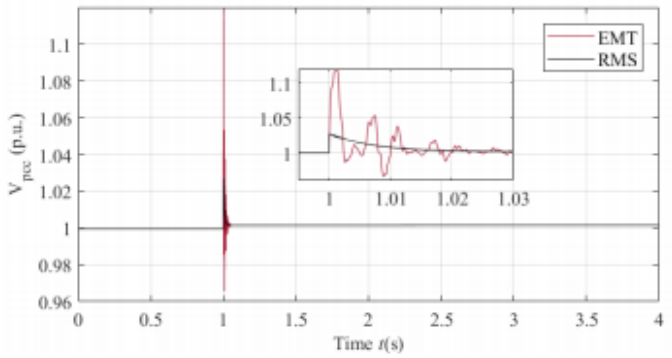

Figure 2.1: Voltage at PCC in an offshore network, computed with an RMS and an EMT model [27]

2.1.2. Hardware and Software

The RTDS simulator is the world's leader among real time power system simulators [28]. In order to be considered real-time, a simulator needs to achieve the computation of one time step in a time less than or equal to the time step itself. The RTDS can perform EMT calculations over a frequency range from 0 (DC circuit) to 3 kHz. It is typical for EMT programs to work with a time step of $25-50\mu s$, the so-called large time step. Since the fast switching power electronic devices present in today's converters require more detailed computations, the RTDS also provides a small time steps library, which work with a time step of $1-4\mu s$. In order to connect a large time steps with a small time steps model, a VSC interface block needs to be inserted. This block is represented in figure 2.2.

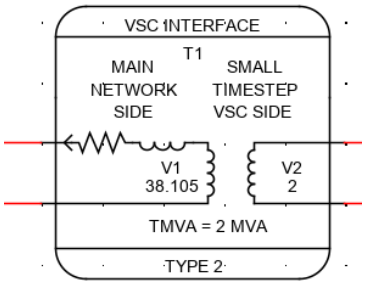

Figure 2.2: Interface block between large time steps and small time steps models in RTDS

The RTDS hardware consists of racks and chassis containing respectively PB5 cards and multi-core processors. The RTDS facility at TU Delft has six racks with PB5 cards and three NovaCor chassis (see figure 2.3), the latter being the most recent technology. The hardware is interfaced with the user via the RSCAD software, which has been designed to create a comfortable working environment for power system engineers. The user can easily perform all of the necessary steps to prepare simulation files, run them, and analyse simulation results.

Figure 2.3: RTDS Novacor chassis [28]

The full setup can be seen in figure 2.4. The software is divided into several modules. The two main modules used in this thesis are the *draft* module, used to design the system (saved in a .dft file), and the *Runtime* module, used to perform the simulations and get the results (dashboard saved in a .sib file). The dashboard of the simulation file allows the user to tune the different parameters of the model thanks to sliders, switches and dials. It is also possible to run simulations from a script, which enables batch mode operation. The script can either be written in a text file, using the RSCAD scripting language, or RSCAD can be interfaced with another platform such as Python or Matlab.

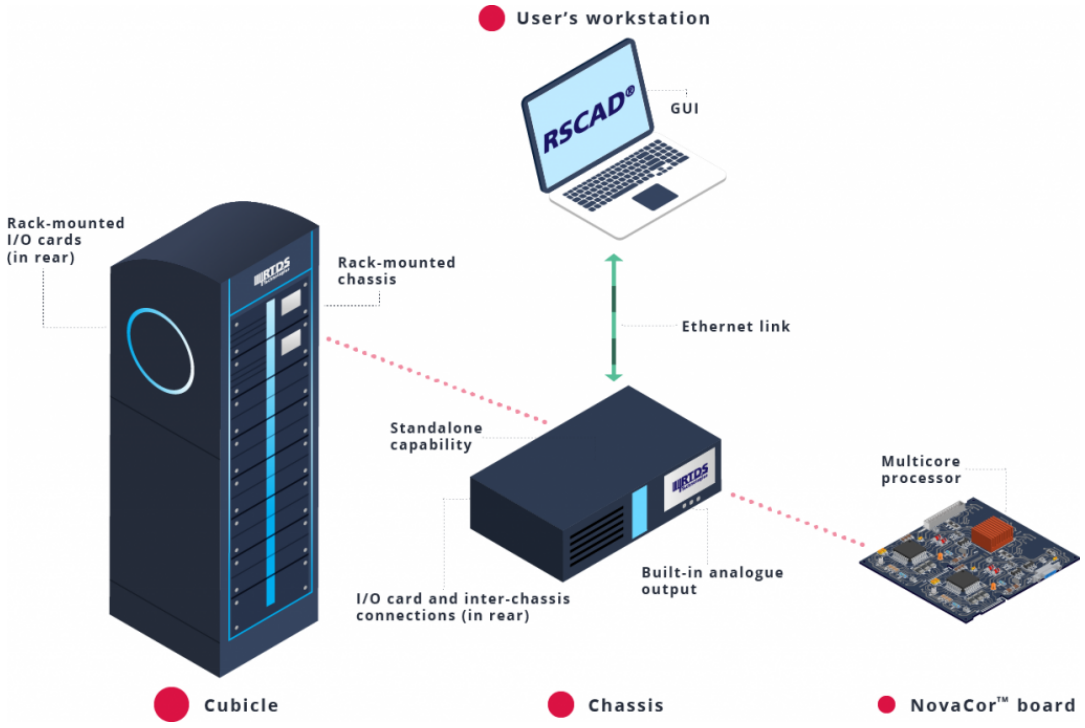

Figure 2.4: RTDS setup [28]

2.2. Baseline Model: Topology and Components

This section first describes the general layout of the offshore hub model taken as starting point for this thesis. Then the most important components of the hub are introduced.

2.2.1. Topology

The network studied in this thesis, which has been depicted in figure 1.2, consists of four offshore wind turbines, each rated at 500 MW, and two MMCs rated at 1 GW each. The rating of the MMCs is in line with the current maximum power rating available for a single MMC, which is 1.2 GW [20]. A more detailed diagram of this baseline model can be seen in figure 2.5. Each WT is connected to a common bus via a back-to-back converter, a transformer and an AC cable. Each MMC forms a monopolar link, which is connected to an ideal

voltage source representing the grid.

In this thesis, electrolysers were connected at different locations, as explained in chapter 3. In addition, the monopolar topology and the voltage sources have been replaced respectively by a bipolar topology and onshore MMCs, as explained in chapter 4. MMC-2 was then used to implement a power sharing strategy. The main contributions of the thesis are indicated in orange in figure 2.5.

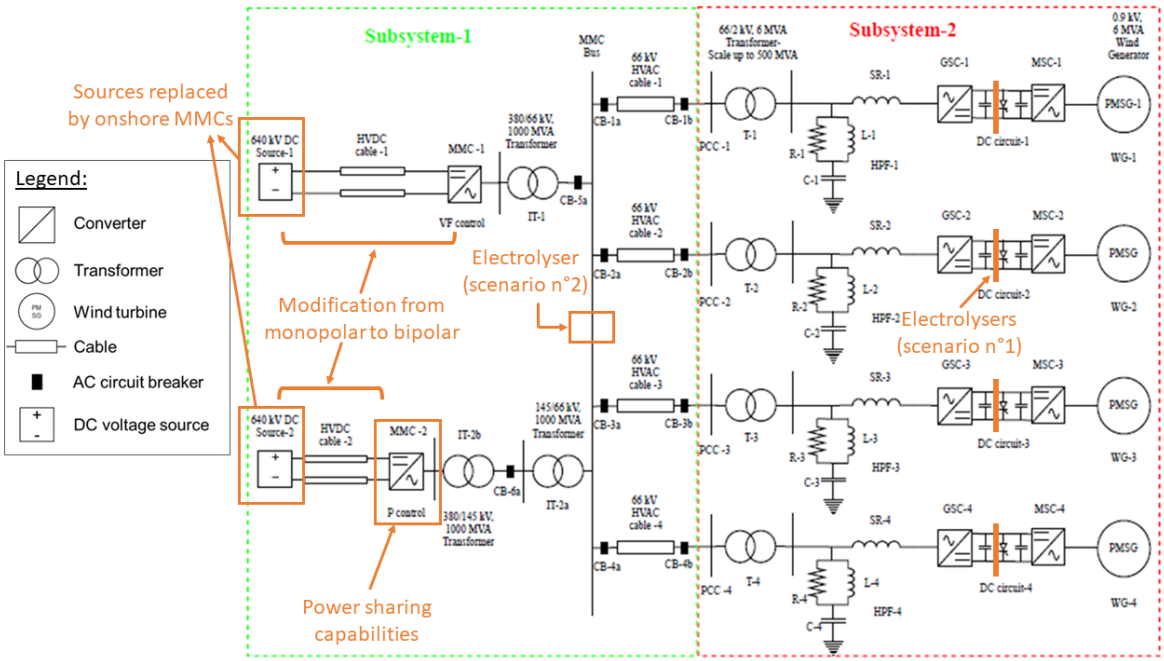

Figure 2.5: Single line diagram of the baseline model implemented in RSCAD [20]

The initial layout of the network stems from the hub-and-spoke concept pictured in figure 2.6. The principle of this layout, which is to be deployed in the North Sea, is to organise the offshore WTs in modular clusters (called "hubs"). The hubs are then linked to each other, as well as to the shore of bordering North Sea countries, thanks to interconnectors (the "spokes"). Hub sizes of 10 to 15 GW are expected to enable optimal economy of scale [2]. A hub can be an artificial sand island, a caisson island, or a platform. According to the NSWPH consortium, this modular layout will enable a cost-effective, step-by-step ramp-up of wind power, while offering flexibility regarding the needs of each offshore location and the energy system (interconnectors, sector coupling with Power-to-Gas (P2G), etc.) [2].

After the modification of the two monopolar links to one bipolar link has been done (chapter 4), the model could be seen as a hub with one single spoke. Adding other spokes is outside of the scope of this thesis, but it could be done in future work, in two different ways: either by connecting more spokes to the AC common bus of the hub, or by converting the point-to-point bipolar link to a Multi-Terminal Direct Voltage (MTDC) link.

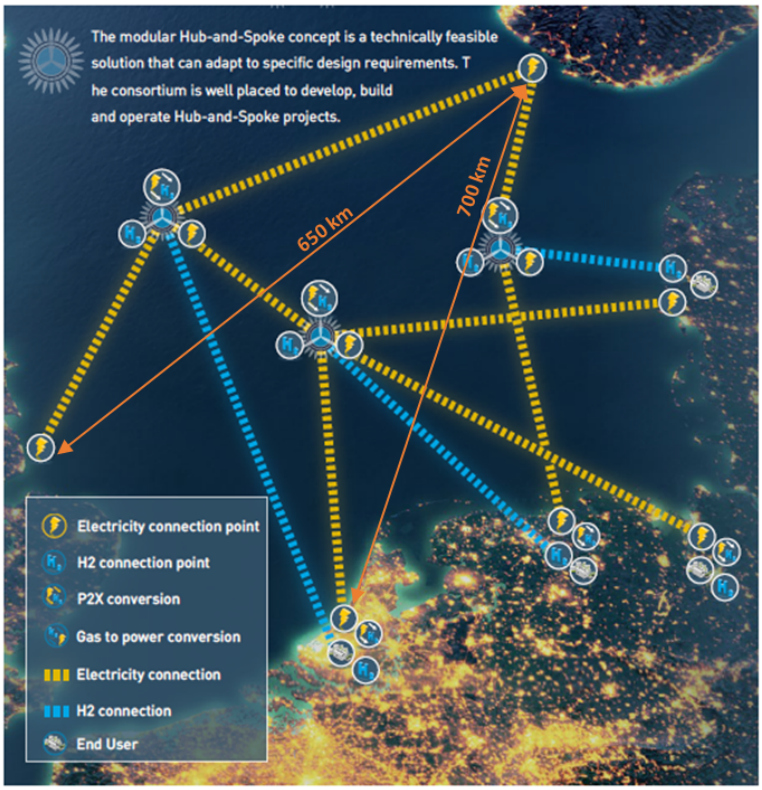

Figure 2.6: Hub-and-spoke layout envisioned by the NSWPH consortium [2]

2.2.2. PMSG

Among the different existing WT technologies, the one used in this thesis is the Type IV WT, which refers to the Permanent Magnet Synchronous Generator (PMSG) technology. As can be seen in figure 2.7, the PMSG is connected to the grid via a back-to-back converter, without the need of a gear box. The gear box is a component prone to wear and tear; its omission is thus of particular interest for offshore applications, where the cost of maintenance is higher than it is onshore. Having no gear box also reduces the weight and dimension of the equipment, and lowers mechanical losses [29].The fact that the turbine is interfaced with a converter allows the PMSG to contribute to grid voltage support, by providing reactive power. One of the drawbacks of this technology is the need for a full-scale converter (that is, the converter is rated to the same power as the turbine), which induces some additional costs and losses. However, this does not prevent the PMSG from being the preferred technology for offshore applications [29].

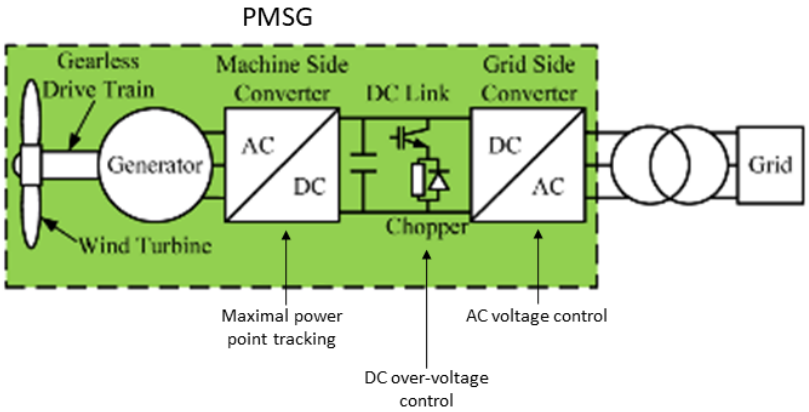

Figure 2.7: A PMSG wind turbine connected to the grid [29]

The baseline model comprises four PMSG WTs, each feeding a rated power of 500 MVA to the hub. However, in RSCAD, the WT's components are rated at 6 MVA, a realistic size for large WT. The power is then scaled up using a scaling factor to multiply the output current of the small time-step/mainstep interface transformer, as shown in figure 2.8. A slider allows to scale up the power step by step during the initialisation process of the simulation.

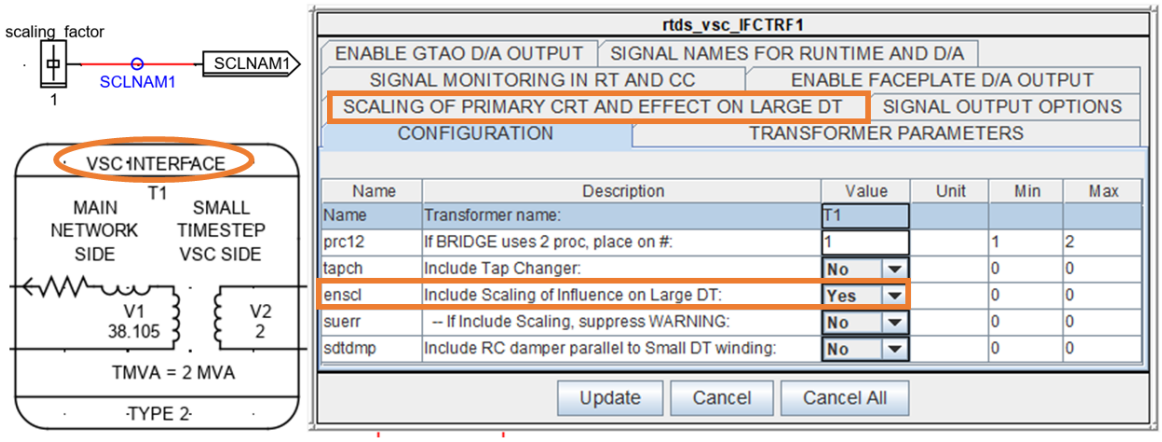

Figure 2.8: Scale-up option in the property window of the small time-step/mainstep interface transformer

2.2.3. MMC

MMCs are currently the state-of-the-art technology for VSC HVDC transmission. Hence, it is the technology which has been chosen for this network. The structural difference between a classical 2-level converter and a MMC can be seen in figure 2.9: each arm of a MMC half-bridge is composed of a series of sub-modules. Each sub-modules can be controlled independently, and either be inserted or bypassed. Such a level of precision allows to closely approximate a sinusoidal waveform, and consequently drastically reduce the level of high frequency harmonics, compared to the 2-level converter [30].

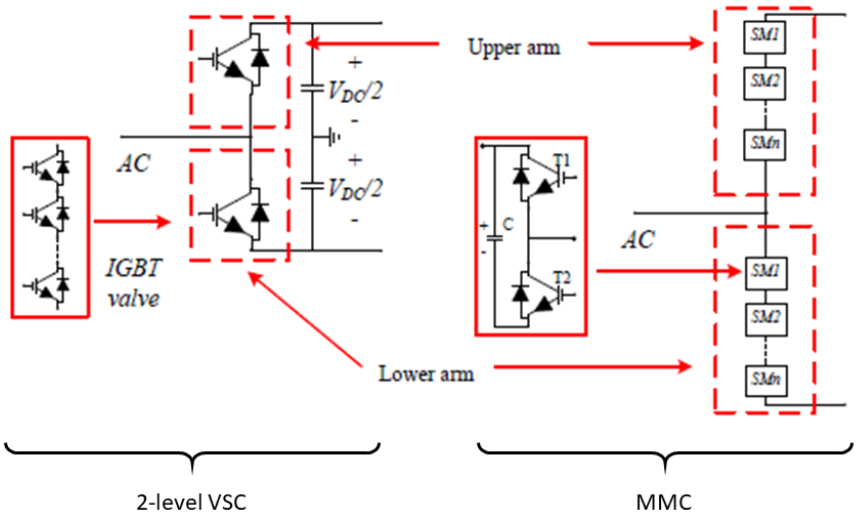

Figure 2.9: Difference in the structure of a 2-level VSC and a MMC half-bridge (only one phase is shown) [30]

In the present model, each MMC is made up of six half-bridge RSCAD modules of type rtds_vsc_MMC5, available in the RSCAD small-step environment library. Each module counts 320 sub-modules, hence creat-

ing the voltage of ±320 kV required for the 640 kV symmetrical monopole transmission cable [20]. A scheme of one of the MMC used in this thesis, along with its transformer, can be seen in figure 2.10. The control strategy is described in the next section.

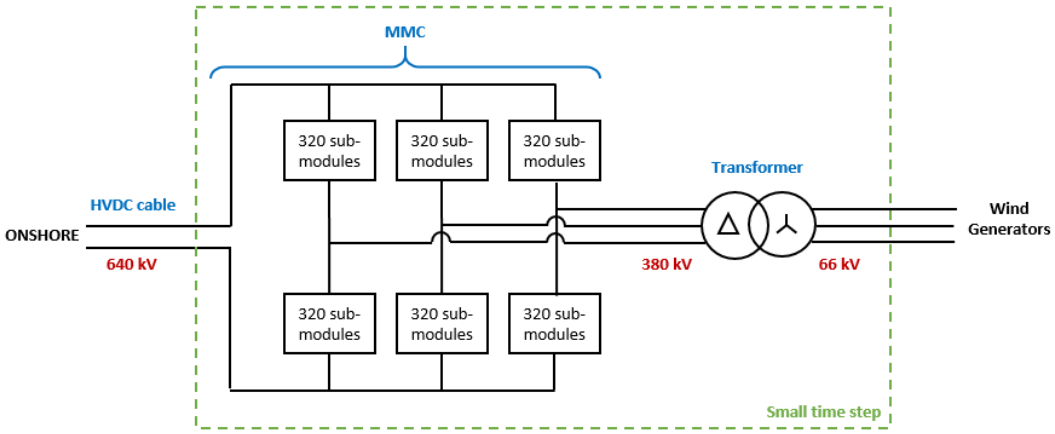

Figure 2.10: MMC topology

2.2.4. Electrolyser

The electrolyser model is divided into several components: a cell, and a buck converter. For some types of connection, a rectifier and a transformer are also required.

The electrolysis technology considered is the PEM technology. The electrolysers used in the present work are modeled as electrolysers rated at 1 or 2 MW, and then scaled up to a larger rating using the RSCAD VSC transformer scaling option.
In the model, the electrolyser stack itself is modeled as a resistor connected in series with a voltage source, as proposed in [12]. This model is shown in figure 2.11. This simplified model is an equivalent model to the actual stack, which is composed of multiple cells connected in series and in parallel. The corresponding parameters, that is, the equivalent resistance value and the equivalent open voltage value, can therefore be adapted by modifying the number of cells connected respectively in parallel and in series. A more detailed description of the electrolyser model is available in chapter 3.

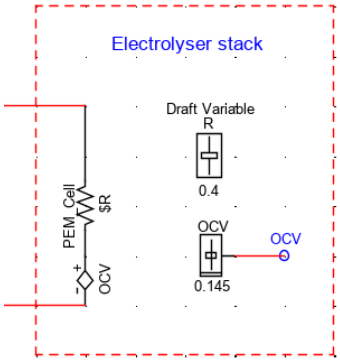

Figure 2.11: Electrolyser stack model in RSCAD

2.2.5. Cables and Voltage Levels

There are two main transmission modes in the network considered: AC cables rated at 66 kV and HVDC lines rated at 640 kV.

AC Network

Usually, offshore wind farms are connected using 33 kV cables. However, it is expected that in the future 66 kV cables will be used. Therefore, the choice has been made to connect the wind turbines of this model to the MMCs using 30 km-long, 66 kV cables.

DC Network

The offshore hub is connected to the shore via a HVDC link. In the initial model, a 640 kV, symmetric monopole configuration is used for each MMC. This configuration is then changed for a bipolar configuration with ground return (rigid bipole), in chapter 4 of this thesis.

2.2.6. Connection to the Main Grid

In the initial model, a simplification has been made regarding the connection of the hub to the shore. The assumption is that the two onshore MMCs can be represented by two equivalent constant DC voltage sources. In chapter 4 of this thesis, those two voltage sources have been replaced with two MMC models in order to allow for the study the control interaction between the onshore and offshore MMCs.

2.3. Control Structures Implemented in the Network

2.3.1. MSC

The control scheme used for the control of the Machine Side Converter (MSC) is a conventional current control. It can be divided into two loops. In the outer loop, the actual speed of the WT is compared to the optimal speed provided by the Maximal Power Point Tracker (MPPT), in order to calculate reference currents in the d/q frame. The reference currents are then sent to the inner loop, where they are compared with the measured currents to define the reference d/q voltages. Finally, the reference voltages are used to compute the modulation parameters of the Pulse-Width Modulation (PWM) scheme controlling the Insulated-Gate Bipolar Transistor (IGBT) bridge [20]. More details about the PWM scheme implementation in RSCAD can be found in appendix B, while the RSCAD implementation of the MSC control strategy can be found in F. The parameters used for the controller can be found in the annex of [20].

2.3.2. GSC

At the grid side, the control strategy adopted is the one of Direct Voltage Control (DVC). This control strategy has been developed and explained in [31] to make up for two shortcomings of the traditional current control scheme. The two flaws of the former scheme are the following:

- In islanded mode, current injection is not possible in a system that does not count any load;
- After the fault, a voltage rise is observed in the DC link. It is due to the integral component of the controller, which is fed with non-zero current reference while the current is being blocked and therefore the measured current is equal to zero.

The solution proposed in [31] consists in removing the Proportional Integral (PI) block of the controller, and replacing it by a properly tuned wash-out filter, in red in figure 2.12. The wash-out filter is a high-pass filter which has been selected to damp the transient signals. The parameters used for the controller can be found in the annex of [20].

2.3.3. MMC

There are two MMCs in the model, each playing a different role. Therefore, the control strategy implemented in each of them is different. They are described in the two following paragraphs. Figure 2.13 gives an overview of the general MMC control hierarchy, picturing the potential addition of other MMCs (left column) in the case of a multi-terminal mesh. The part of the controller studied in chapter 4 is highlighted in the figure.

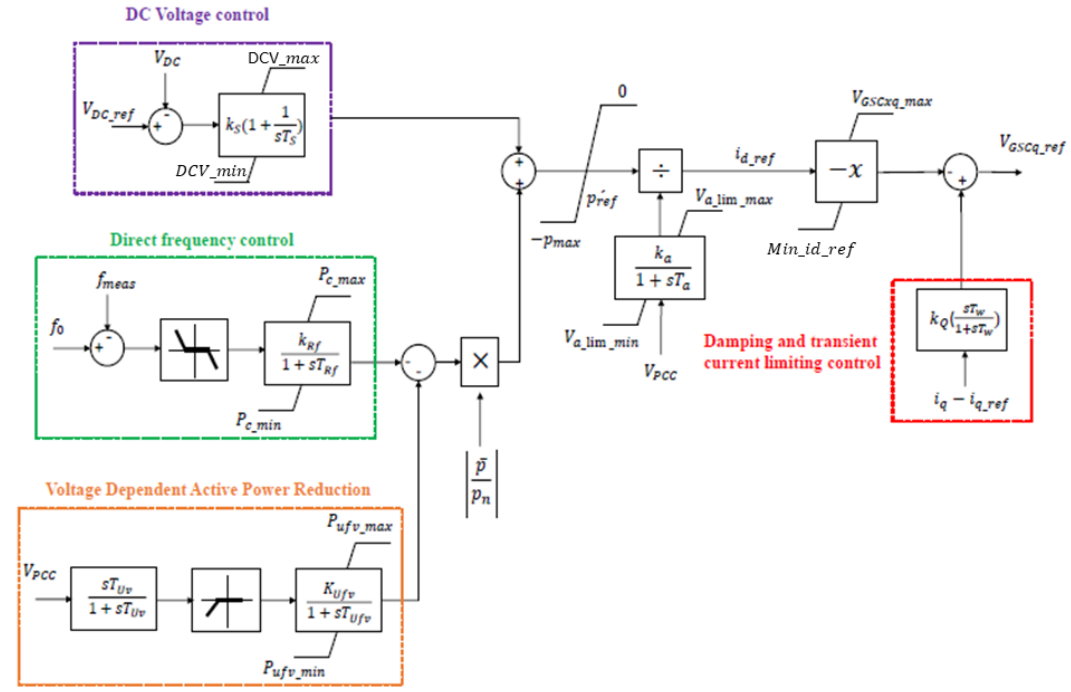

(a) GSC active power control loop

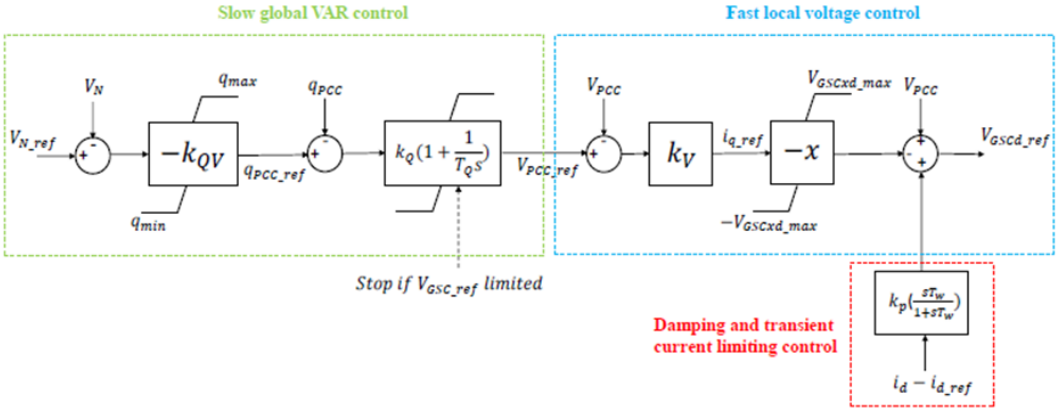

(b) GSC reactive power control loop

Figure 2.12: DVC control scheme [20]

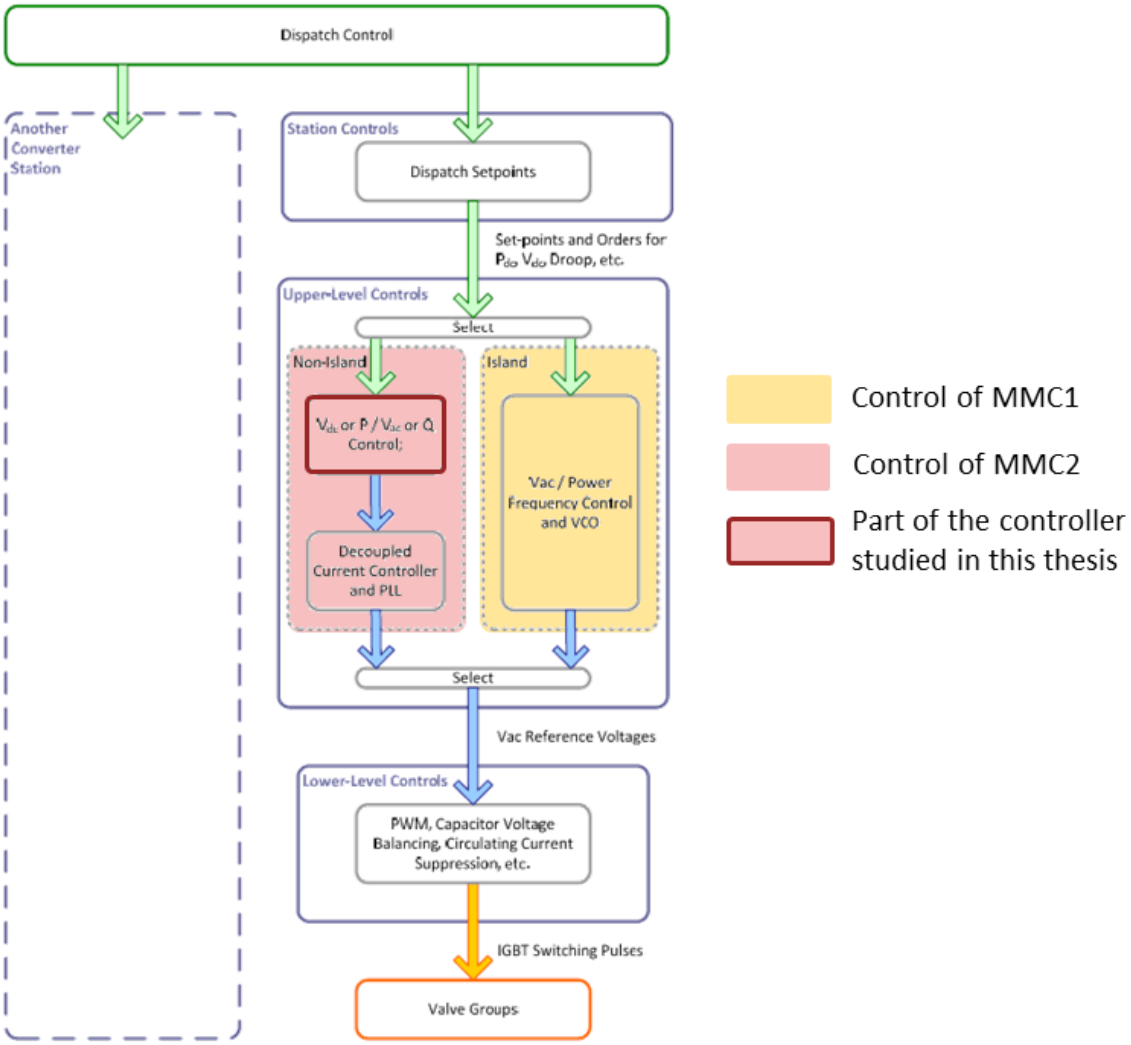

Figure 2.13: Control hierarchy in an HVDC VSC multi-terminal converter (adapted from [32])

MMC-1

The offshore network is a weak grid. Therefore, one of the MMCs needs to set the voltage and frequency references. This responsibility is taken over by MMC-1, which operates in island mode control (V/F control). MMC-1 is therefore a grid forming component. A PI controller takes as input the difference between the reference and measured voltage at PCC. The output of the PI controller is the direct voltage reference of MMC-1, which is then converted to the abc frame to generate the modulation waveforms of the converter. This control scheme can be seen in figure 2.14 [20].

MMC-2

MMC-2 is grid following component, corresponding to non-island mode control. Its controller is derived from the conventional inner/outer loop current controller. However, because it operates in parallel with the V/F controller of MMC-1, the outer loop had to be modified, as there can be only one converter controlling the voltage of the common bus.

In the initial model, the reference current i_d and i_q sent as input to the inner loop are manually set by the user [20], and there is therefore no outer loop. The architecture of the inner loop can be seen in figure 2.15.

In chapter 4 of this thesis, an outer loop is created to generate the i_d reference, therefore enabling a tunable power sharing between the two MMCs.

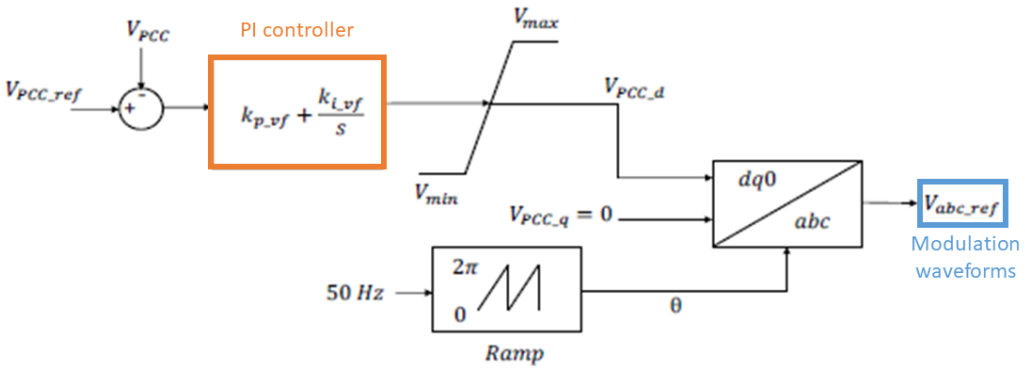

Figure 2.14: MMC-1 controller [20]

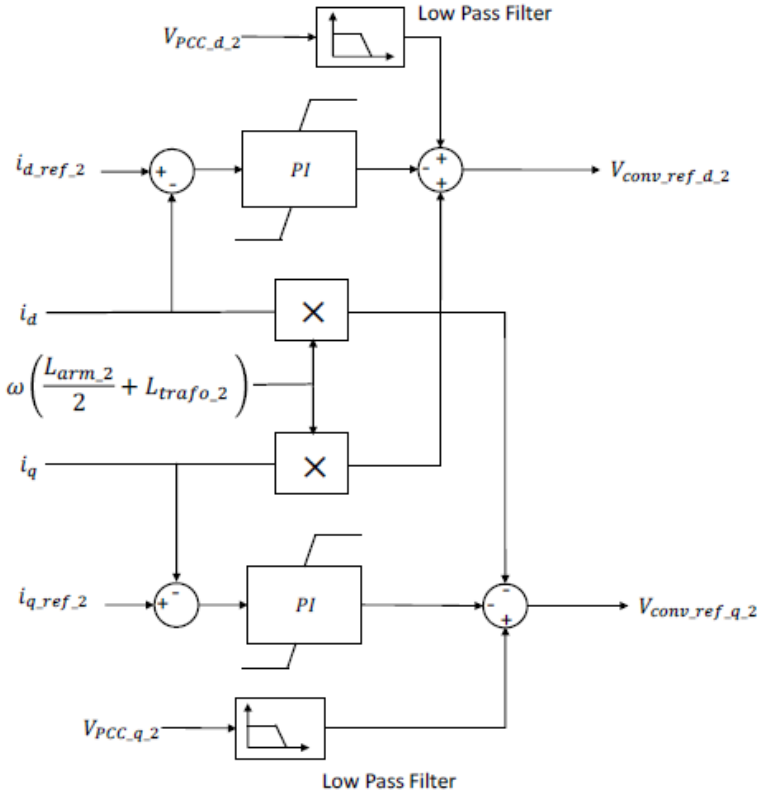

Figure 2.15: Inner loop of the MMC-2 controller [20]

3

Investigation of the Impact of Electrolysers on the Dynamics of the Offshore Hub

Electrolysers have the potential to become a game changer for energy storage and network support in offshore energy hubs, as explained in section 1.1. Promising results can be found in the literature, but at the same time a lack of simulations of the dynamic performance of a zero inertia hub featuring electrolysers is observed. In this chapter, a review of the results found in the literature is first presented. It is followed by a case study comparing two different possible ways of connecting electrolysers to the offshore hub: in the first case, four smaller electrolysers are connected directly to the DC links of the WT via a buck converter; in the second case one larger electrolyser is connected to the AC common bus via a buck converter and a transformer.

3.1. Literature Review

3.1.1. Electrolysers Potentialities in Supporting the Network

As discussed in section 1.1, the need for storage technologies in today's electrical network does not need to be proven anymore. Focus is nowadays given to the choice of the technology which should be adopted, how to implement it, and how to scale it up. In offshore hubs, the absence of local electrical load makes the question of storage even more relevant.
Electrolysers are the option discussed in this thesis. One of their main advantages is that, contrary to battery or super-capacitor storage options, the product of electrolysis is an easily-transportable energy carrier. The transport of hydrogen from offshore hubs to shore has been broadly studied from a techno-economic point of view, as mentioned in chapter 1. For instance in [6], the authors note that former gas pipelines could be reused to transport the hydrogen produced offshore to the shore. They claim that pipeline transport requires much less Capital Expenditure (CapEx) and Operational Expenditure (OpEx), and generate less losses than electricity cable transport. Hydrogen can also be stored with extremely low self-discharge, which makes electrolysers a very good candidate for long-term energy storage applications [4]. Literature shows results from techo-economic assessments which qualitatively suggest the potential of the coupling of the offshore electricity and gas network: in [33], it is shown that such a coupling would increase the cost-competitiveness of offshore wind power.

Studies also highlight the very good response performances and flexibility of electrolysers, such as in [34]. In [35], a model of a large-scale electrolyser has been developed in RSCAD in order to compare simulation results and field measurements. Very fast ramp-up and ramp-down times, as well as frequency support potential, have been observed. In [36], different frequency support control methods for a 300 MW electrolyser have been compared, concluding that the best results were obtained with the Virtual Synchronous Power (VSP) controller. Beyond-requirement response times of electrolysers are illustrated in figure 3.1.

It should be noted that even thought the hydrogen produced by the electrolyser could theoretically be turned back into electricity by a fuel cell and re-injected into the grid for further support, this last conversion step has not been considered in this thesis. This does not mean that up-regulation is not possible: as stated

in [37], it is economically optimal to run the electrolyser at about 50 % of its maximal capacity if using it as primary reserve, thus providing the remaining capacity as upward reserve.

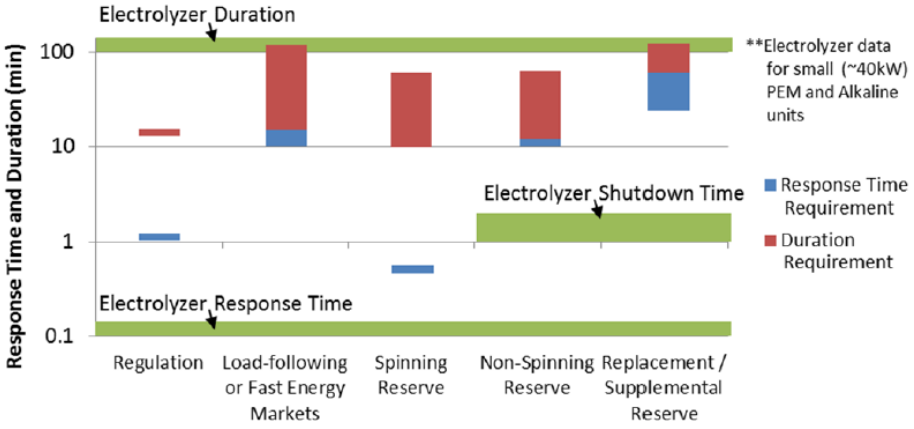

Figure 3.1: Electrolysers flexibility compared to electricity market requirements [38]

3.1.2. Sizing and Location of the Electrolysers

Sizing and connecting the electrolyser(s)[1] in the optimal way are not straight-forward. Optimal electrolyser rated capacity has been estimated to be close to 30 % of the wind turbine rated capacity in both [39] and [13]. This ratio has been adopted for the work done in this thesis. The choice of the optimal ratio is outside of the scope of this thesis.

Regarding the location, in [13] as well as in [14], three main locations are considered for the electrolyser (see figure 3.2): C1) in-turbine at the DC link of the PMSG WT, C2) next to the HVDC substation (common bus), C3) behind the squirrel cage induction generator WT, and C4) onshore. Location C3 is specific to another technology of WT and location C4 is not relevant in this work as the focus is on the offshore hub. Therefore, in this thesis, only the two offshore locations C1 and C2 are considered, and will be developed in the next sections.

3.2. Investigation Option C1: Connection on the DC links of the Wind Turbines

3.2.1. DC link Topology

Connecting a storage element to the DC link of the back-to-back converter of a PMSG WT is an idea recurrently found in the literature. Two publications have been selected as an example:

- In [40], a system composed of a battery, a fuel cell and an electrolyser is connected to the DC link of a PMSG wind turbine in a stand-alone configuration. The storage system is controlled in order to support the variations of the loads or wind speed and to limit the DC link voltage of the full-scale power converter in a small range. However, in this study the fuel cell-electrolyser is considered to have slow dynamics, whereas the PEM electrolyser technology considered in this thesis has been chosen for its notably fast [10];

- In [41], a supercapacitor is connected to the DC link of a PMSG WT via a buck-boost converter. The storage system allows for fault ride-through capabilities as well as mitigation of power fluctuation of the grid-connected system. However, the system is not designed to operate in islanded mode as it does not have any long-term energy storage or dissipation, contrary to what is proposed in the present thesis.

In this work, four 2-MW electrolysers have been integrated in the model. Each electrolyser is connected to the DC link of the back-to-back converter of one of the 6-MW WTs. The network layout can be seen in figure 3.3.

[1] According to the scenario (3.2 or 3.3), one or four electrolysers were integrated in the network

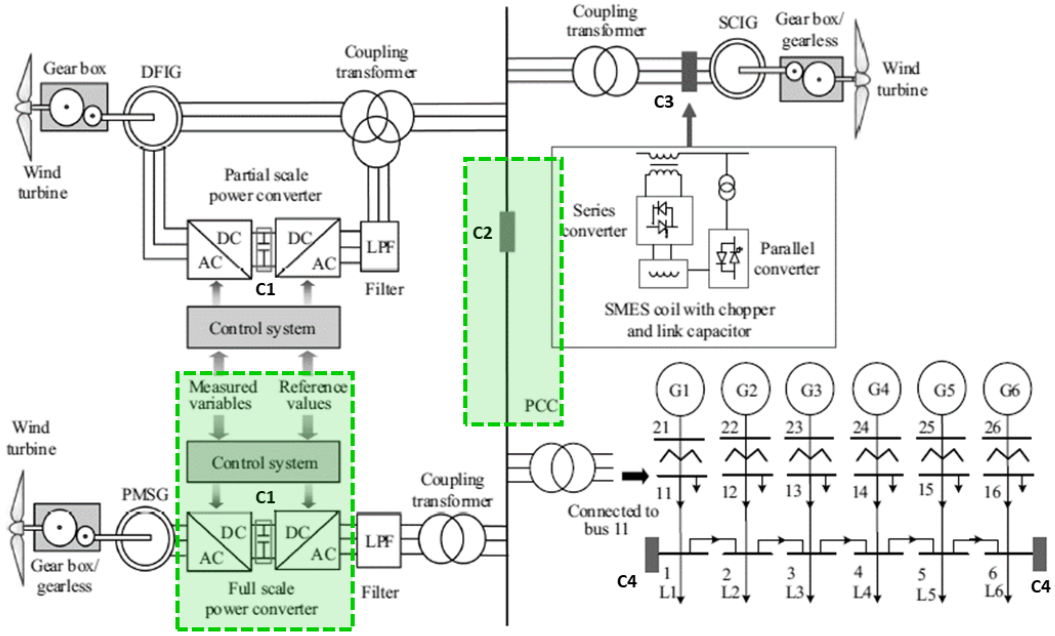

Figure 3.2: Different locations of the energy storage device (adapted from [14]). Only locations C2 and C3, highlighted in green, are considered in this thesis. Location C1 was meant for another WT technology, and location C4 was not relevant for an offshore hub.

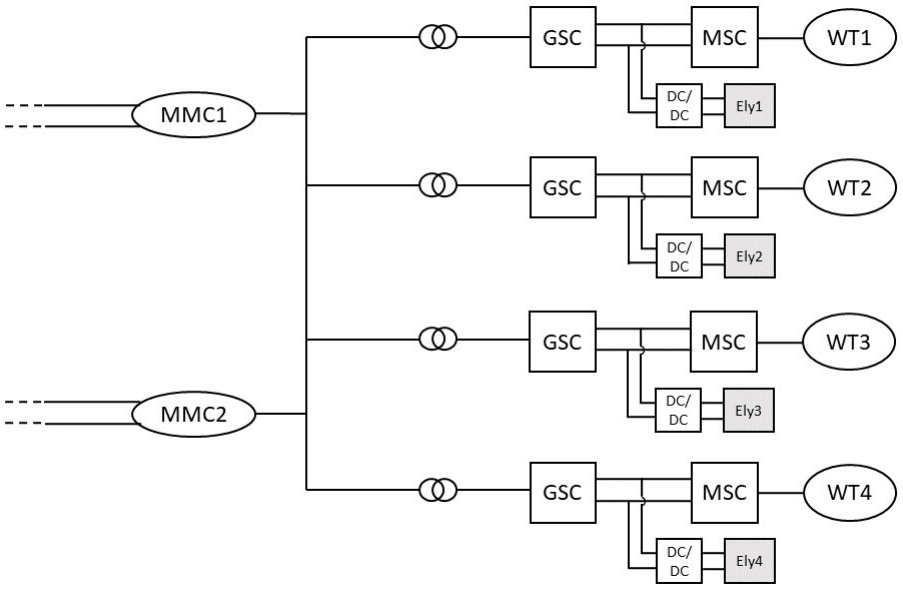

Figure 3.3: Connection of four electrolysers on the DC link of the WTs

3.2.2. Modelling of the DC-DC Converter

RSCAD Environment

The DC-DC converter used to connect the stack to the DC link is a buck (i.e. step-down) converter, developed in [12]. Since the WTs and their back-to-back converter are modelled in the small time-step environment, the most natural option was to model the buck converter in the small time-step environment as well. However, unexpectedly high losses were observed with this model. They can be explained by looking at how switches

are modelled in RSCAD.
In the mainstep environment, the conductance matrix changes each time a switch is turned On or Off, which leads to unfeasible computing times for real-time simulations. Therefore, a different approach has been adopted with the small time-step environment: instead of modelling an open circuit as a small conductance, it is modeled as a series connected resistor (R) and capacitor (C); and instead of modelling a short circuit as a large conductance, it is modeled as an inductor (L). In turn, the L, R, C components are modeled as their Norton equivalent (parallel connected current sources and conductances), using the Dommel algorithm and trapezoidal rule of integration. The parameters L, R and C are chosen so that the Dommel conductances are equal: $g_{oc} = g_{sc}$ (cf. figure 3.4), which alleviates a lot the computation costs [42].
The main drawback of this model is higher than expected converter losses, due to artificial switching losses associated with abrupt switching from a small inductor (switch On) to a small capacitor (switch Off). This problem has been observed during this thesis. Another drawback is the confusion that the user can experience when asked to fill in some parameters (base current, voltage, dynamic factor). It is not possible for the user to directly specify the amount of losses of the converter [42]. An improved converter model developed by RTDS is introduced in section 3.2.2.

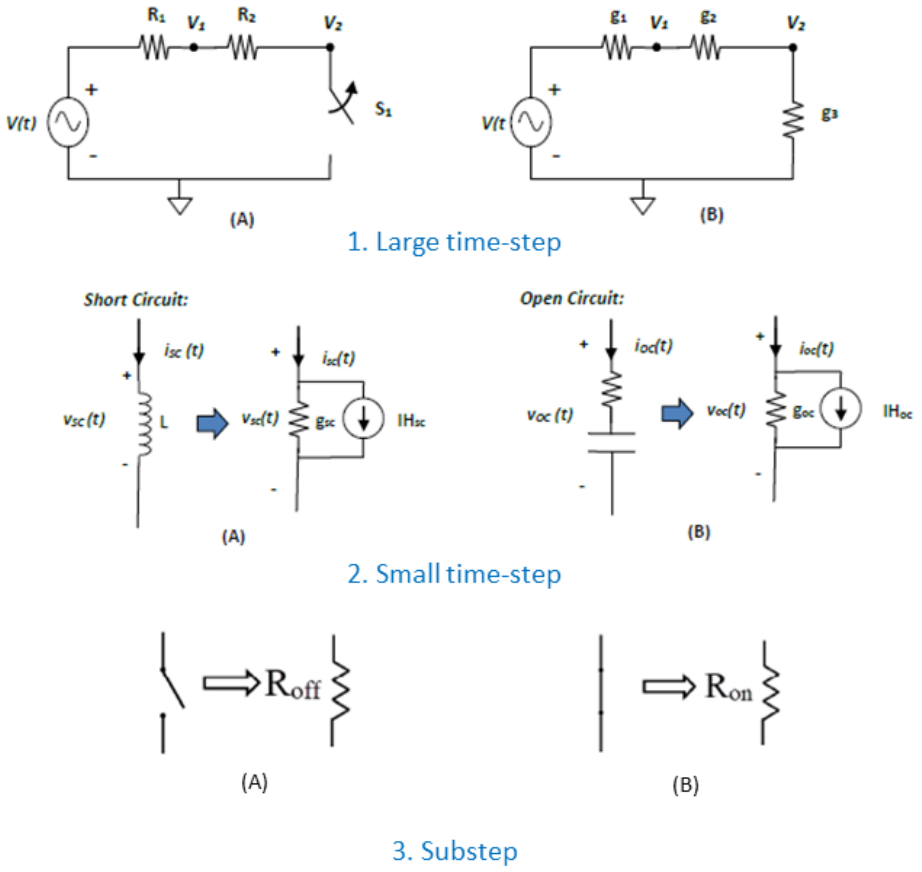

Figure 3.4: Switch model in large time-step (1), small time-step (2) and substep (3) in RSCAD (adapted form [42])
(A)=Switch ON / (B)=Switch OFF

Interfacing a component placed in a substep environment with a WT placed in the small time-step environment would have generated other numerical issues. Hence, for this thesis it was decided not to focus on the above-mentioned issues because the focus of the analysis is on the effect of the integration of electrolysers in the hub, and not on the efficiency of the electrolyser system. A thorough analysis of the numerical solutions is suggested as future work. However, the substep environment has been used to model the electrolyser connection option in section 3.3, as interfacing the substep environment with the mainstep environment was not leading to additional issues as in the case of the small time-step environment.

Equation of the Buck Converter

In this section, the equations used to derive the fundamental relation of the buck converter are detailed.

The following notations are adopted:

- i_L, i_R, i_C: current through the inductor, resistor, capacitor respectively;
- V_L, V_R, V_C: voltage across the inductor, resistor, capacitor respectively;
- V_{in}, V_{out}: input and output voltages;
- V_{OC}: open circuit voltage of the electrolyser stack;
- L, R, C: value of the inductor, resistor, capacitor respectively;
- $T_s = \frac{1}{f_{sw}}$: period of one operation cycle of the switches of the converter, equals to the inverse of the switching frequency;
- D: duty ratio (ON-time of the switch divided by T_s)

The operation of the buck converter in continuous mode can be described by dividing one operation cycle into two phases, as shown in figure 3.5:

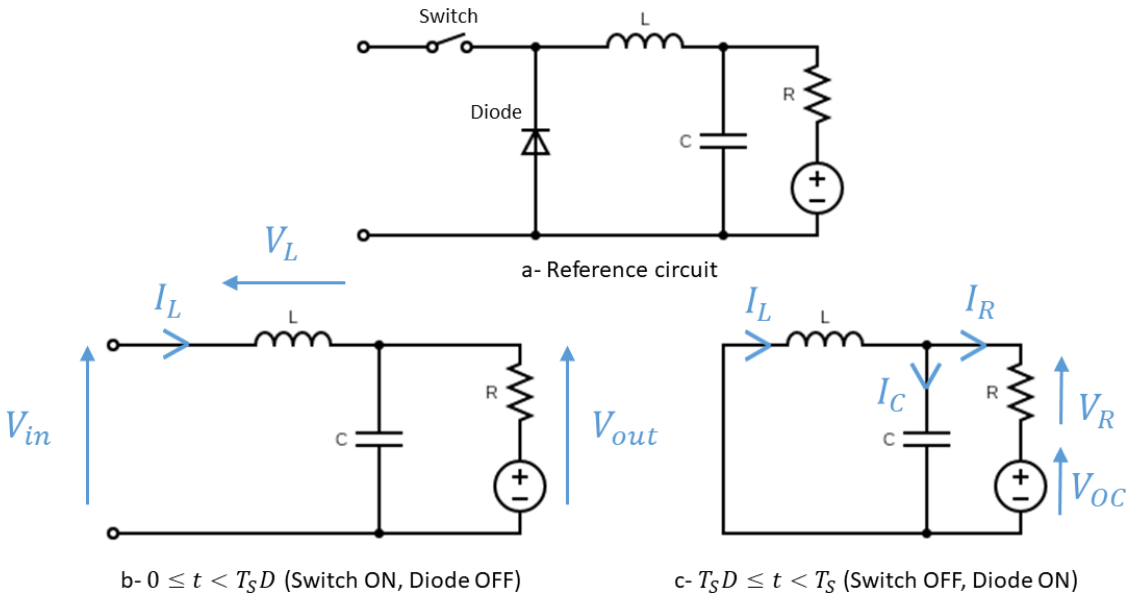

Figure 3.5: Reference circuit of the buck converter (a) and its equivalent circuits according to the state of the switch: switch ON (b) or switch OFF (c)

Case 1: $0 \leq t < DT_s$

During this interval of time, the switch is closed and the diode is blocking. The equivalent circuit can be seen in figure 3.5(b).

From figure 3.5(b), the expression of the inductance voltage gives the variation of the inductance current:

$$V_L = L\frac{\mathrm{d}i_L}{\mathrm{d}t} = V_{in} - V_{out}, \tag{3.1}$$

$$\frac{\mathrm{d}i_L}{\mathrm{d}t} = \frac{V_{in}}{L} - \frac{V_{out}}{L}. \tag{3.2}$$

Considering the switching frequency is high, the assumption can be made that V_{in} and V_{out} are constant over the considered time period T_s. By integrating 3.2 over the whole period T_s we obtain:

$$\Delta i_L = \frac{DT_S}{L}(V_{in} - V_{out}). \tag{3.3}$$

Case 2: $DT_s \leq t < T_s$
During this interval of time, the switch is open and the diode is passing. The equivalent circuit can be seen in figure 3.5(c).
The expression of the inductance voltage gives:

$$V_L = L\frac{\mathrm{d}i_L}{\mathrm{d}t} = -V_{out}, \tag{3.4}$$

$$\frac{\mathrm{d}i_L}{\mathrm{d}t} = -\frac{V_{out}}{L}. \tag{3.5}$$

Using the same assumption as for the first interval of time, we obtain by integrating 3.5:

$$\Delta i_L = -\frac{(1-D)T_S}{L}V_{out}. \tag{3.6}$$

Finally, since no energy is stored in the inductor over time, the sum of the inductor current variations in both intervals of time (given by 3.3 and 3.6) must be equal to zero:

$$\frac{DT_S}{L}(V_{in} - V_{out}) = \frac{(1-D)T_S}{L}V_{out}. \tag{3.7}$$

By rearranging equation 3.7, the following relation is obtained:

$$V_{out} = DV_{in}. \tag{3.8}$$

The equation 3.8 is the fundamental relation used in the controller of the buck converter. Since V_{in} (voltage of the DC link) is maintained constant by the GSC (cf. section 3.2.3), by controlling D, it is possible to control V_{out} (electrolyser stack voltage). Moreover, the current of the electrolyser stack can be considered to be a function of its voltage (assuming constant temperature and pressure) [12]. Therefore the power consumed by the electrolyser is a function of V_{out} and can be controlled by controlling the duty ratio D of the buck converter.

Interleaved Model

For high current applications which require low output current ripple, the interleaved mode of operation is used. This means that an inductor is connected to three branches of switches, connected in parallel as shown in figure 3.6, and with a relative phase shift (but the same duty ratio [2]). This method is known to reduce the output current ripple: a reduction of the current ripple by 20 % was achieved by using an interleaved topology in [43]. Motivated by this approach, three DC-DC converters have been connected in parallel in [12] to realise high output currents.

[2] The duty ratio (or duty cycle) is the fraction of the operation cycle during which the switch of the converter is turned On.

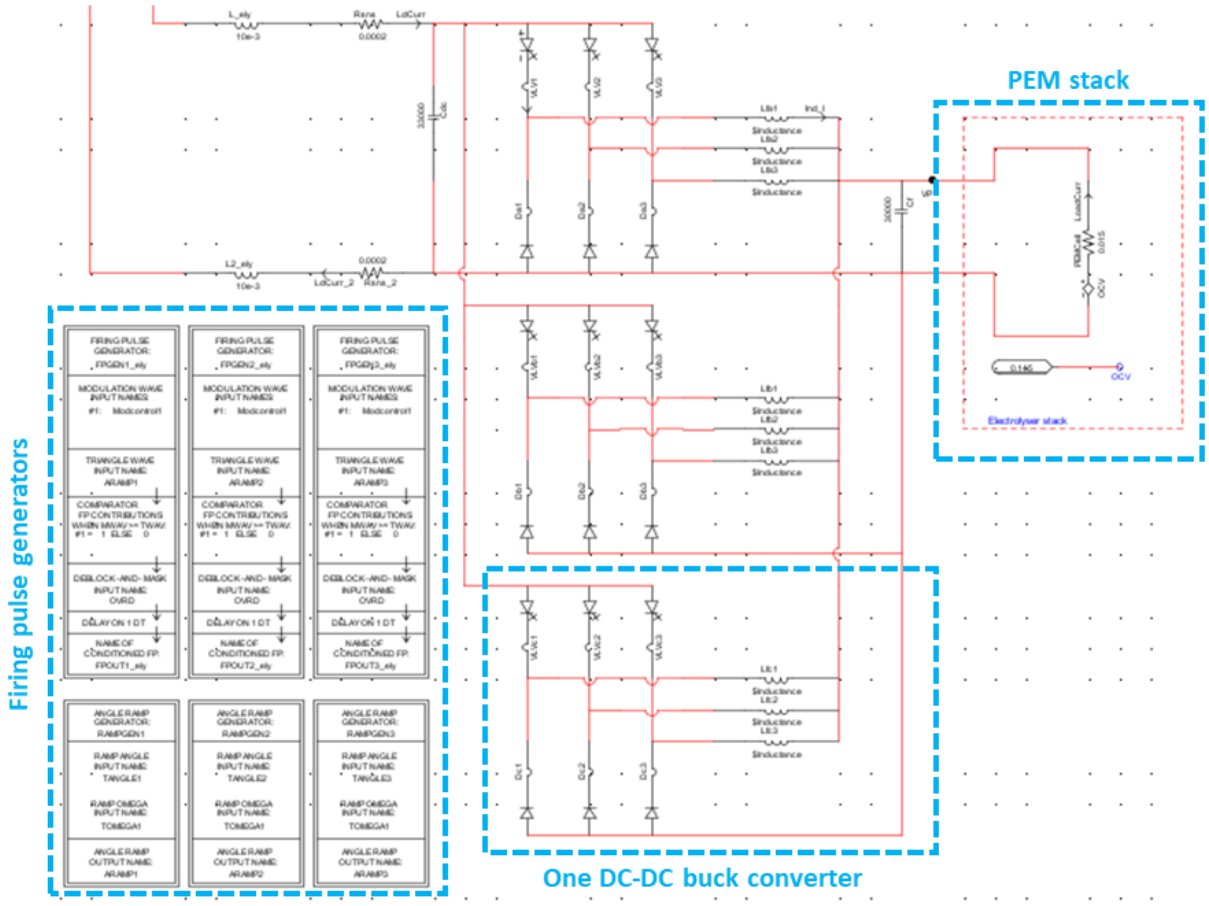

Figure 3.6: DC-DC converter and electrolyser model in RSCAD, connected to the DC link of a WT as shown in figure 3.3

Switching Frequency

Operating the buck converter at high switching frequency can be beneficial because it improves the transient responses. However, it has also the drawback of lowering the efficiency of the converter in the RSCAD model, because losses inside the converter are increased. It was found that a suitable switching frequency at which the buck converter can be operated to ensure a minimal efficiency of at least 75 % is $f_{sw} = 1kHz$. In figure 3.7, the effect of increasing the switching frequency from 1 to 2 kHz can be observed. When $f_{sw} = 1kHz$, at 0 s, the efficiency is 79 %, while when $f_{sw} = 2kHz$, after stabilisation at 10 s, the efficiency has dropped to 64 %.

However, the switching losses observed are actually artificial losses due to the L/C switching representation used in the RSCAD software 3.2.2. The substep environment can help reduce those artificial losses, but it cannot be interfaced easily with the small time-step environment. The Universal Converter Model (UCM) which is developed and has been very recently released by RTDS could be a solution to this artificial losses problem in the future [44]. At the moment, the UCM is only available in the main-step and substep environments. In the main-step environment, the UCM represents converter performances accurately in the 3 kHz range [44].

Therefore, the switching frequency of $f_{sw} = 2kHz$ was chosen, because it gives a better control accuracy.

[2]For tuning purposes, the modulation ratio was set manually for this figure (the PI controllers were bypassed). In normal operation the response of the electrolyser is smoother thanks to the PI controllers.

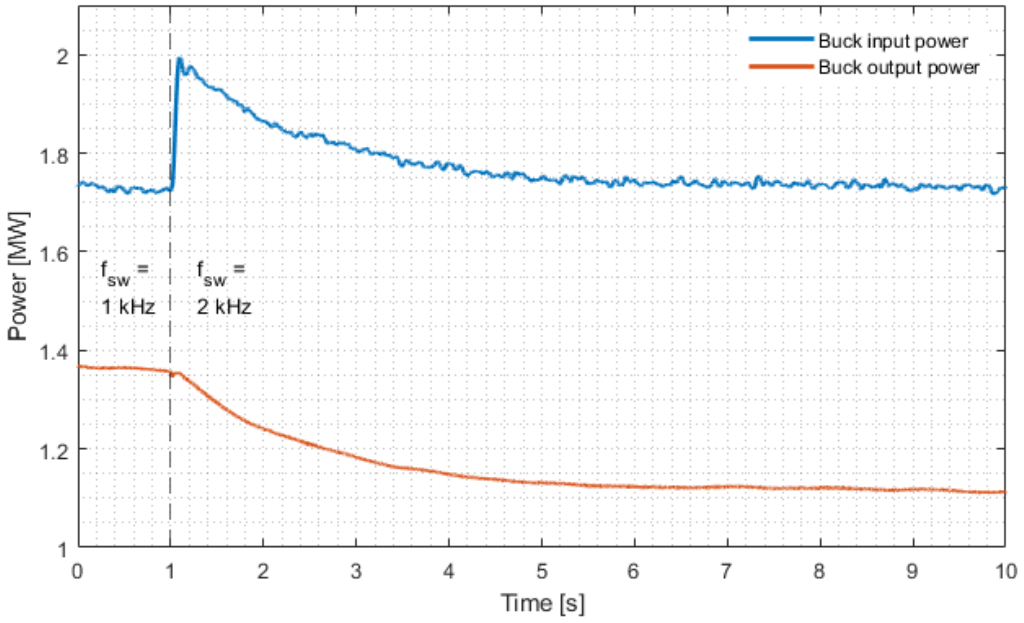

Figure 3.7: Time response of the buck converter when increasing the switching frequency from 1 to 2 kHz

3.2.3. Controls

An overview of the proposed control of the expanded DC link can be seen in figure 3.8. The main aspects of the control strategy and control parameter tuning of the GSC, DC link chopper and buck converter are detailed in this section.

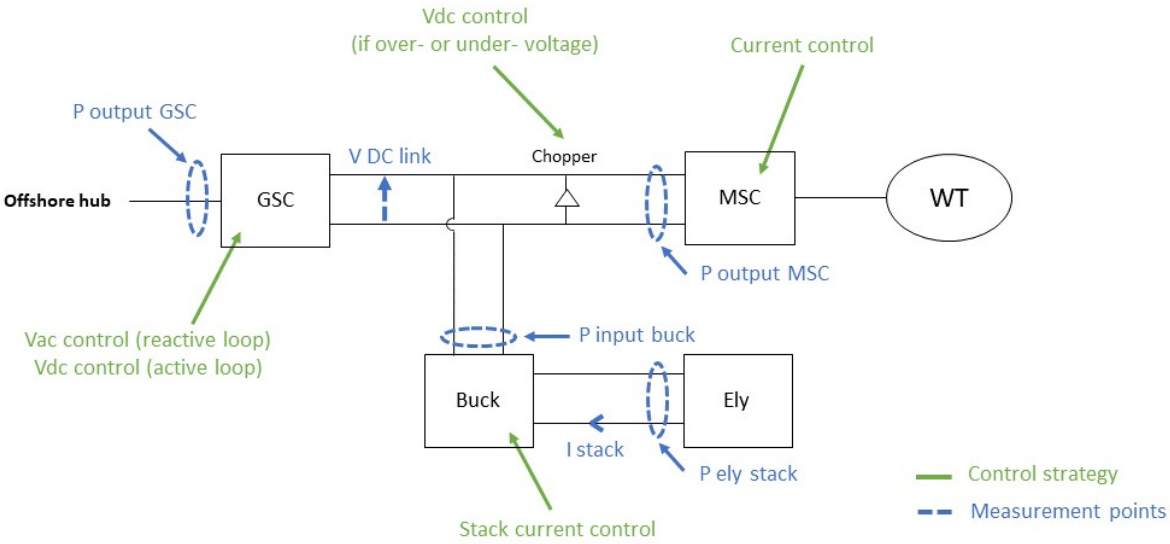

Figure 3.8: Control of the expanded DC link and measurement points

GSC

The GSC is mainly responsible for the regulation of the DC voltage, as previously shown in figure 2.12(a). In order to achieve a faster and more accurate voltage control, especially under varying wind speed, some parameters of the active power loop of the DVC control have been modified compared to the baseline model described in section 2.3.2.

In the baseline model, a voltage drop of more than several pu was observed at the DC link when the wind speed was dropping, as shown in figure 3.9. It was found that the drop was due to a saturation of some

of the control parameters. In order to prevent such a voltage drop, the boundaries of some of the limiters in the GSC active power control loop were enlarged compared to the baseline model. The boundaries of the limiters were incrementally increased (upper boundary) or decreased (lower boundary) until no more saturation of the control parameters occurred, while no drawback due to enlarged boundaries was observed. The parameters which have been modified are indicated in the summary table 3.1 at the end of this section.

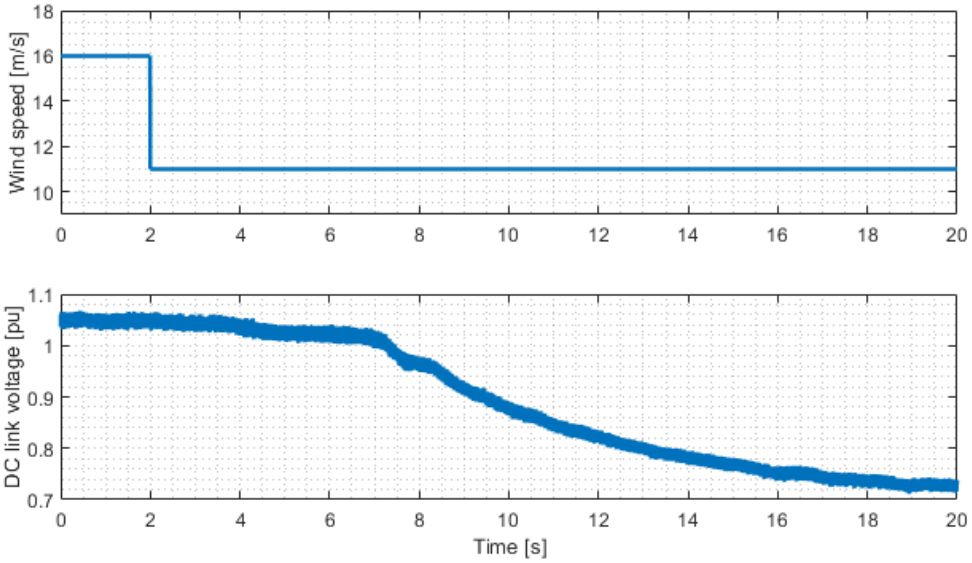

Figure 3.9: Effect of a wind speed drop on the DC-link voltage of one of the WTs in the baseline model

Chopper

The chopper consists of a switch in series with a large resistor, connected across the two poles of the DC link, as shown in figure 3.10(a). When the switch is turned on, a short-circuit is created across the link, thus lowering the voltage, as explained in [20].

The chopper contributes to maintaining the DC link voltage stability in case of over-voltage, which happens mainly during faults. The control of the chopper is done in two steps, represented by the two red blocks in figure 3.10(a).
In the first step, an activation (ON/OFF) signal is generated by a flip-flop table, as shown in figure 3.10(b). The chopper is turned ON when the voltage of the DC link becomes higher than the maximal value Max_chop, and turned OFF when the same voltage falls below the minimal value Min_chop. Parametric sensitivity analysis was performed to determine the most suitable values for the activation boundaries of the chopper. It was found that the values $Max\_chop = 1.3pu$ and $Min\_chop = 0.98pu$, undesirable action of the chopper (e.g. over-reaction preventing the flow of power to the electrolyser) is prevented, while the DC voltage is maintained between satisfactory values.
Parallel to this first control action, the magnitude of the chopper firing signal is calculated based on the deviation of the DC link voltage from its reference. A first order filter (with gain G_chop and time constant S_chop) is used to generate the chopper modulation wave magnitude from this deviation, as can be seen in figure 3.10(c).
In the second step, the switching signal and the magnitude signal are combined to generate the references for the firing pulses of the chopper, as shown in figure 3.10(d). Finally, the references for the firing pulses are transformed into firing pulses by a firing pulse generator block in RSCAD.

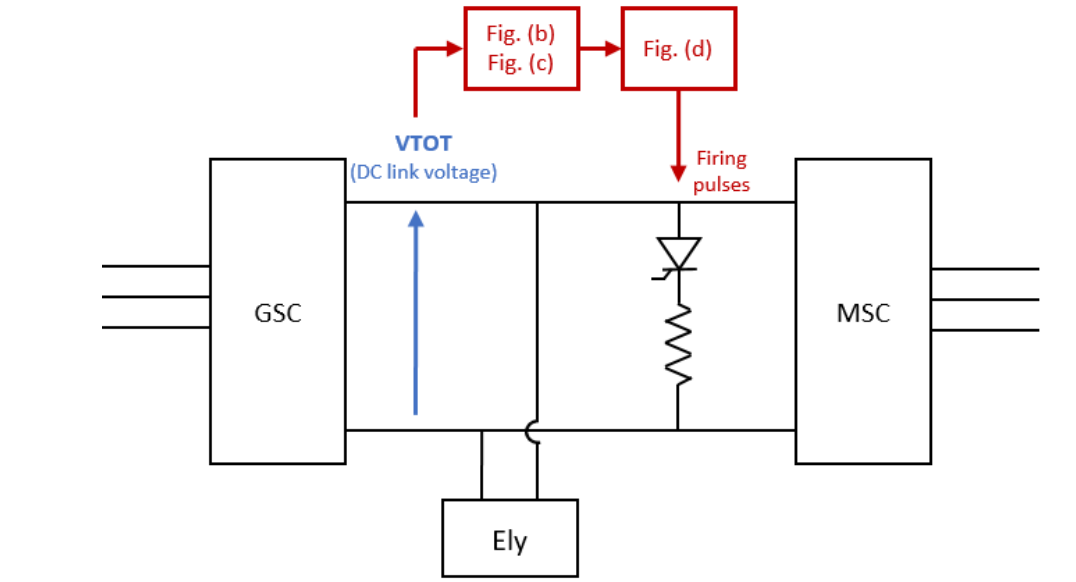

(a) Chopper schematic

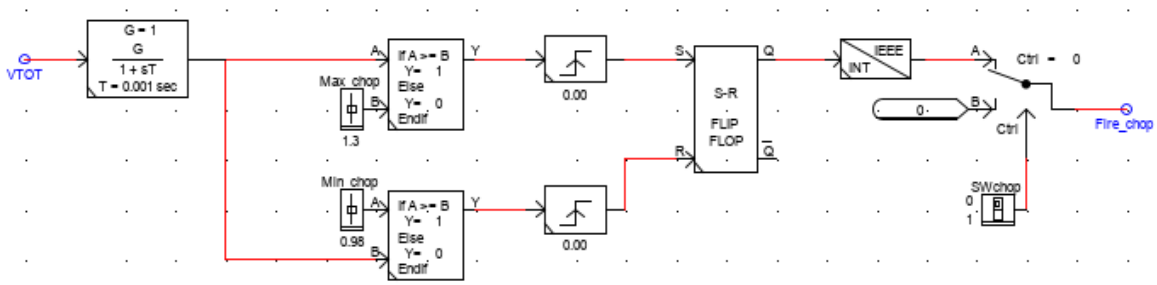

(b) Chopper ON/OFF control

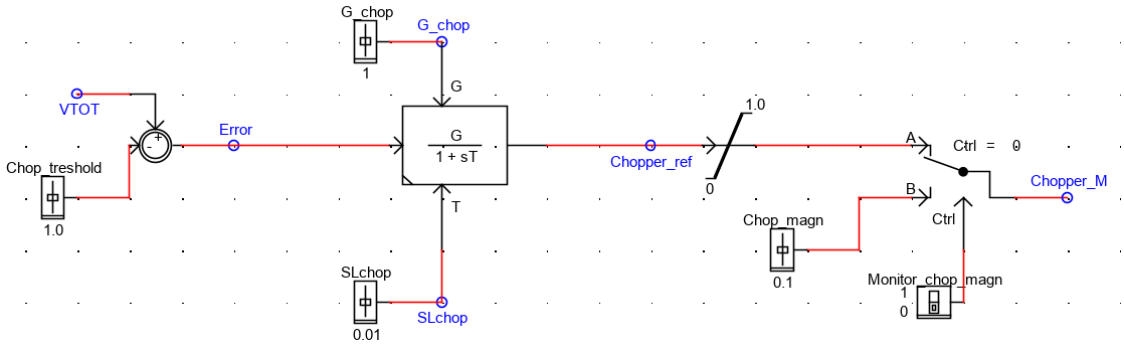

(c) Chopper magnitude control

Figure 3.10: Chopper schematic and control structure in the case of connection of an electrolyser to the DC link

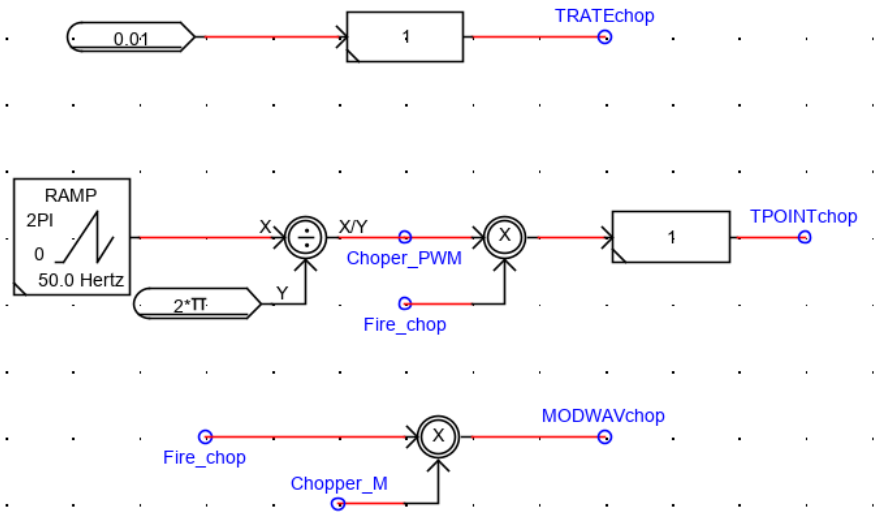

(d) Chopper firing pulses generation

Figure 3.10: Chopper schematic and control logic, in the case of connection of an electrolyser to the DC link (cont.)

Buck Converter

The buck converter controller is composed of two loops, as shown in figure 3.11 [3] :

- The outer loop is responsible for limiting the output power of the GSC to 4 MW. The electrolyser will absorb the surplus power coming from the wind turbine. In case of fault (*SWD2A* signal in figure 3.11), the buck converter is controlled to absorb all the power generated by the wind turbine, limited by its rated capacity. The output of the outer loop is the stack current set-point, given as input to the inner loop;
- The PI in the inner loop outputs the modulation wave which is given as input to the firing pulse generator. The time constants are set so that the outer loop is 10 times slower than the inner loop, as advised in [45]. Indeed, the action of the outer loop should not overlap with the action of the inner loop, and enough time should be given to the inner loop to adjust to the new set-point send by the outer loop.

The MSC control has not been modified. The MSC regulates the DC current, as described in section 2.3.1. The main parameters used for simulation in RSCAD can be found in table 3.1 [4] [5].

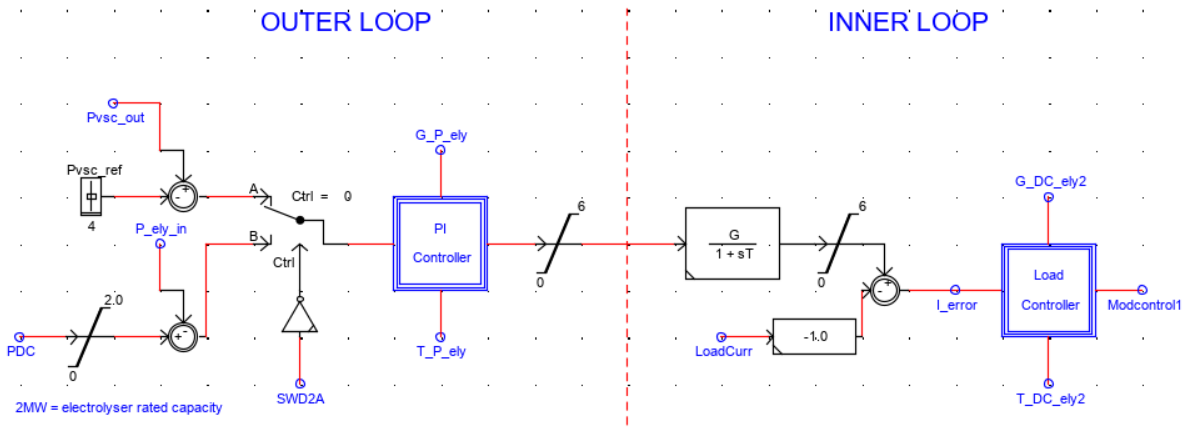

Figure 3.11: Buck converter controller

[3] In figure 3.11, the input parameters for the outer loop are defined in figure 3.8. In addition, *LoadCurr* is the current at the electrolyser stack, and *Modcontrol1* is the reference signal for the firing pulse generator of the buck converter.
[4] During the initialisation, T_VDC = 8 as proposed in the baseline model [20].
[5] The same parameters are used for the four electrolysers.

Buck converter		GSC		Chopper	
Parameter	**Value**	**Parameter**	**Value**	**Parameter**	**Value**
T_P_ely	0.5 s	VDCR	1.0 pu	SLchop	0.05 s
G_P_ely	0.001	T_VDC	0.02 s	G_chop	1
T_DC_ely2	0.02 s	G_VDC	10		
G_DC_ely2	0.005	Max_DVC	6.5		
		Min_ID_Ref_set	-0.6		
		Min_VTQ	-0.6		

Table 3.1: Control parameters used for the simulation (unless stated otherwise). Parameters related to the buck converter, GSC and chopper can be visualised in figure 3.11, G.1 and 3.10 respectively.

3.2.4. Results

Two events are analysed in this section: a step in the wind speed, and islanding due to a HVAC fault. These events have been chosen so that the reaction of the model to the most abrupt and critical events can be tested.

Wind Speed Step

First, a wind speed step from 9 to 14 m/s [6] is applied to the hub. As shown in figure 3.12, a filter with time constant 0.5 s is used to avoid any numerical issue that might appear due to the discontinuity of the wind speed step. The slider *G1WIND* is used to manually define the wind speed, while the two variables *WindSpeedSource* and *Wind_Profile* are used to input a predefined wind speed profile, as explained in appendix A.3.

The resulting behaviour of the network is shown in figure 3.13: the power has been measured at the output of the MSC, at the output of the GSC and at the input of the electrolyser buck converter. Power measurements are shown on the second graph of the figure. They are expressed in MW before the interface transformer, so they are not scaled up. Additionally, measurements of the DC-link voltage and electrolyser stack current are shown on the third and fourth graphs of figure 3.13 respectively. All the measurement points are indicated in figure 3.8.

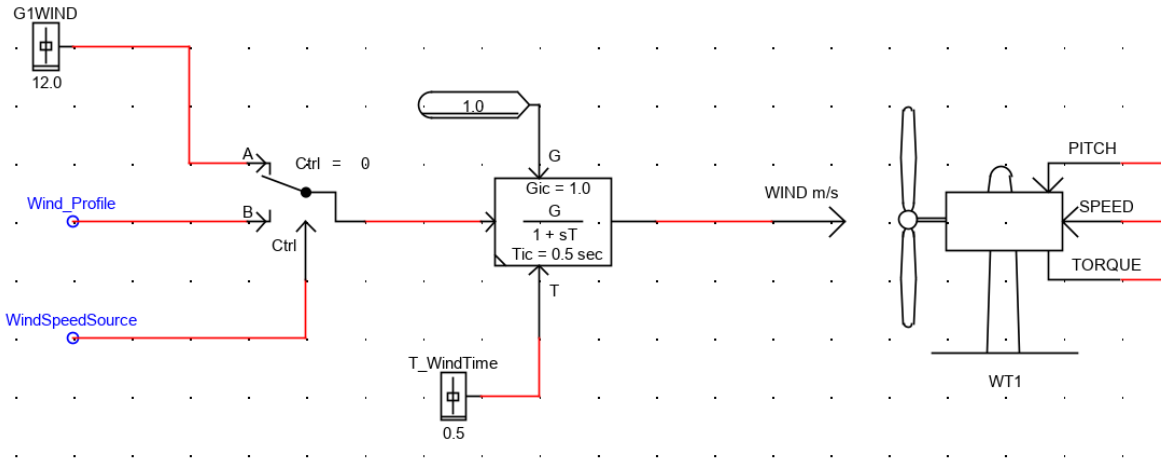

Figure 3.12: Wind speed input in RSCAD

The second graph of figure 3.13 shows that the control strategy presented in figure 3.11 is respected for both electrolyser 1 and 2: as soon as the output of the GSC reaches 4 MW (at 5 s), each electrolyser starts to absorb the surplus power coming from the WT, thus maintaining the output power to the stable value of 4 MW. It should be noted that in this scenario, the power output of the four WT was the same by design of the network (see figure 2.5), hence for the sake of clarity only the output of WT-1 has been plotted, with the caption "single MSC output".

After 10 s, the WT output keeps increasing, while the electrolyser reaches its rated capacity (2 MW). Therefore

[6] This represents an extreme wind speed step, in line for example with the wind speed time series proposed in [46].

the output of the GSC also increases over 4 MW.

Furthermore, attention was given to the choice of the control parameters. The time constant and gain of the PI controllers (starting with the inner loop PI) were changed incrementally in a predefined range until a satisfying behaviour was achieved. The system presented a minor sensitivity to changes of the gain values, but a considerable sensitivity to changes of the time constant values. In order to show the effect of different settings of the PI parameters, a sample comparison is presented in figure 3.13. Two different values of the inner PI controller time constant have been implemented: the electrolyser connected to WT-1 has a time constant $T\_DC\_ely2 = 0.02s$ (orange line) while the electrolyser connected to WT-2 has a time constant $T\_DC\_ely2\_2 = 0.01s$ (green line). Those two values have been selected because they represent a threshold in the behaviour of the system.

The third graph shows that for electrolyser 1 and 2, the DC-link voltage is effectively maintained close to 1 pu by the GSC, thanks to the modifications mentioned in section 3.2.3 (modification of the signal limiter boundaries). The chopper is not activated during this time, so its power consumption is null and has not been plotted.

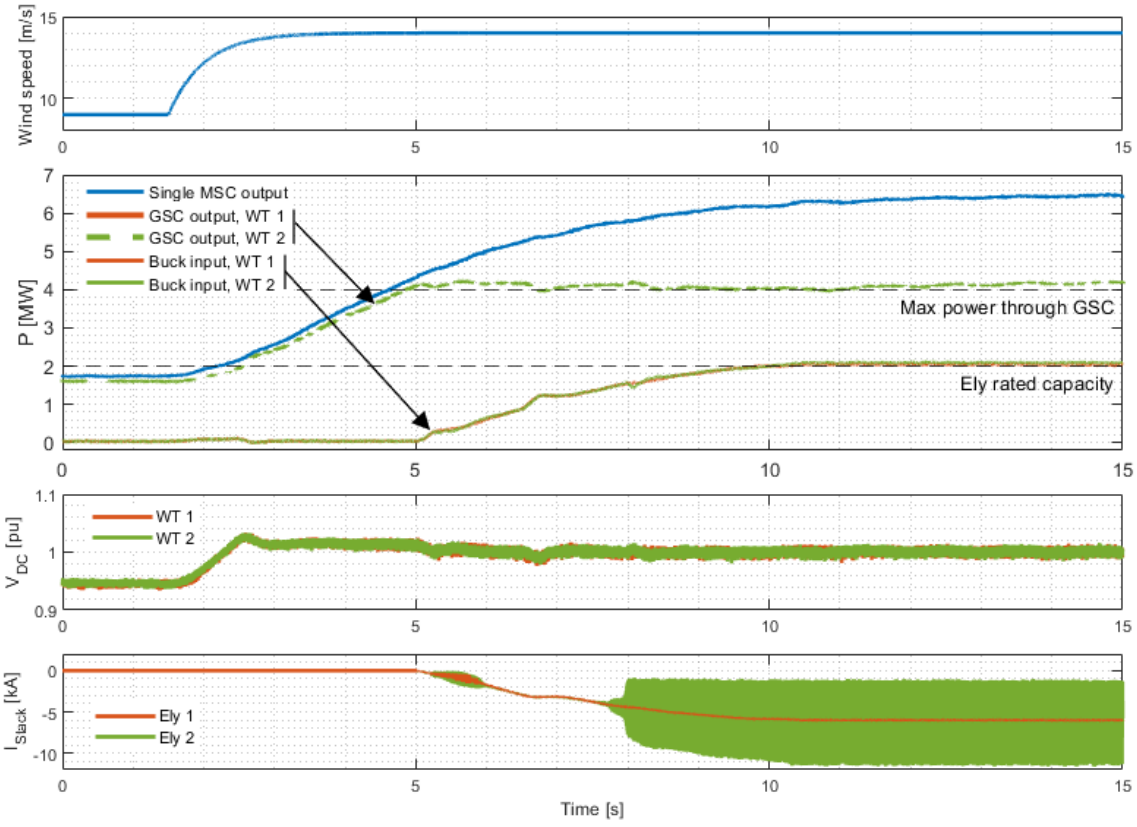

Figure 3.13: Time response [7] of DC links 1 and 2 having two different time constants (0.02 s for Ely 1 and 0.01 s for Ely 2) in the inner loop PI, under wind speed step from 9 to 14 m/s

The last graph shows that the current going through the electrolyser stack exhibits a significant oscillatory behavior. The stability of the DC link is not jeopardised, only the output of the buck converter (flowing to the electrolyser stack) is affected. The main outcome of this comparison is that if the time constant of the PI is too small, the system becomes too sensitive as the integral component reacts too fast (compared to the system response time) when trying to correct the static error. Consequently, the current flowing through the electrolyser stack is not stable: these oscillations are not acceptable for the electrolyser.

[7] Power measurements have been filtered through a first order filter with time constant 0.02 s, voltage and current measurements are not filtered

However, if the time constant of the PI controller is too high, the response time of the electrolyser will be lengthened, as the integral part of the controller will be too slow (compared to the dynamics of the system) in trying to correct the static error. As a result, the control rule will be met with a delay.
Therefore a compromise has to be found between speed and stability of the system. Lowering the time constant of the PI leads to a faster response, until a certain threshold where oscillations appear. Figure 3.13 shows that this threshold is located between 0.01 and 0.02 s for the PI of the inner loop. Hence a time constant of 0.02 s was selected, as can be read in table 3.1. It can be noticed that the time constant of the outer loop PI controller has been chosen more than 10 times higher than the time constant of the inner loop PI controller, in order to avoid interference between the control actions of the loops.

Wind Speed Profile n°2: High Gradient

In this section, the same simulation is run, with the best time constant (0.02 s) set for all electrolysers. The only difference is that the wind speed step is now replaced by the wind speed profile n°2 selected in appendix D. This wind speed profile has been extracted from a set of historical offshore wind speed data, on the criteria of the steepest wind speed gradient.

The performance of the DC link of the WT and of the electrolyser system under these real life conditions is shown in figure 3.14. The results being the same for all four WT, only the measurements for WT-1 has been plotted.
As can be seen on the graphs, the network behaves as expected. The power output of the GSC is limited to 4 MW as long as the rated capacity of the electrolyser allows it. When the generated power becomes too high, the electrolyser cannot increase its consumption anymore so the output power increases.

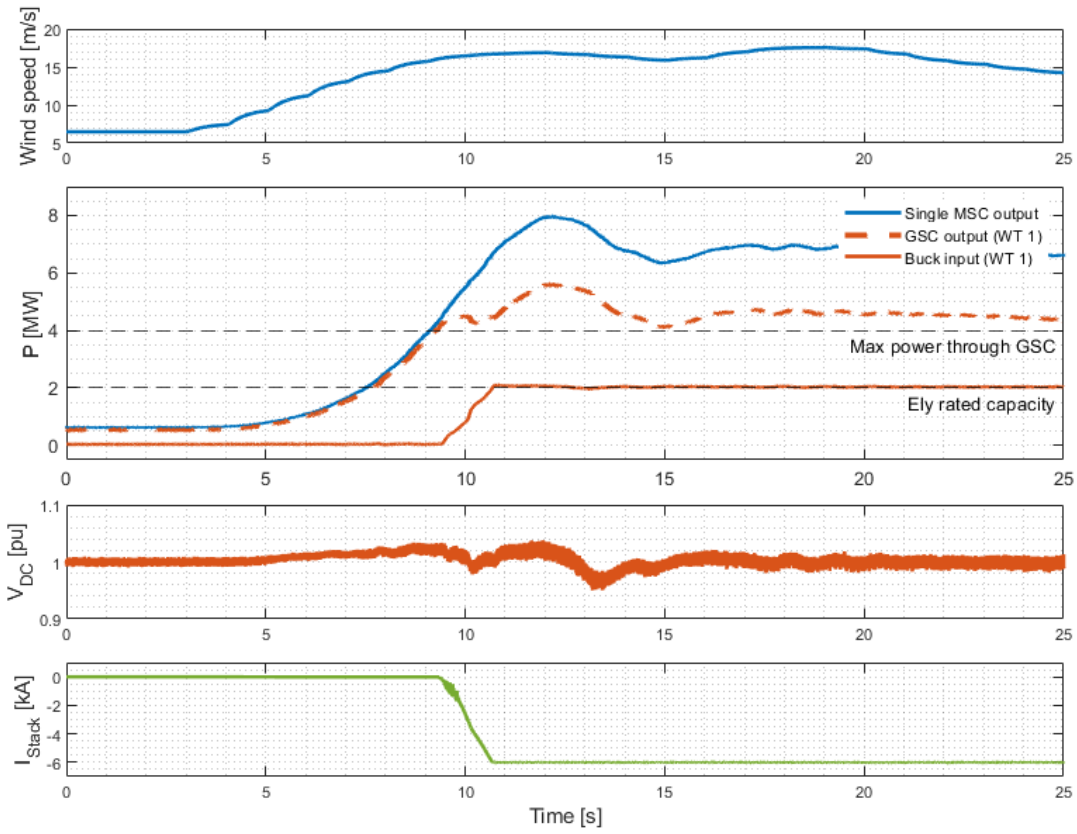

Figure 3.14: Time response of the DC link of WT-1 under wind speed profile n°2, with electrolysers connected to the DC links of the WTs

Islanding Due to HVAC Fault

Due to a permanent three-phase to ground fault on HVAC cable 1, the AC breaker on this cable is opened (no reclosing scheme is activated) and WT-1 is islanded. The location of the fault and of the circuit breaker can be seen in figure 3.15. During this event the wind speed is kept constant at 13 m/s, and the breakers on the other HVAC cables are de-activated.

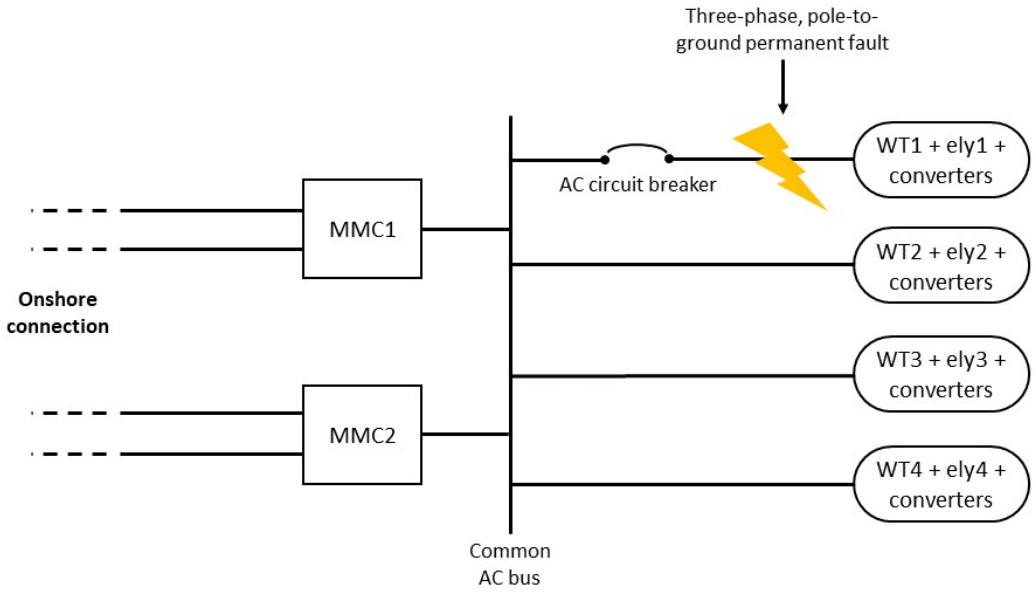

Figure 3.15: Location of the HVAC fault

The results are presented in figure 3.16, and the corresponding measurement points can be seen in figure 3.8. Only the measurements taken at WT-1 (graphs b and d) and WT-2 (graphs c and e) are shown, since the measurements for WT-3 and WT-4 were similar to the ones for WT-2.
Initially, the WTs produce a steady power of 5.8 MW (blue line on graphs b and c). The buck converters of the electrolysers are consuming 1.6 MW (purple line on graphs b and c), so that the GSC outputs are maintained at 4 MW (red line on graphs b and c), as required by the control scheme described in 3.2.3. The green line on graphs b and c shows the electrolyser power consumption. To understand why it is lower than the buck converter power consumption, refer to section 3.2.2.

At 0.5 s, the short-circuit fault on HVAC-1 is triggered (figure 3.16, graph a, which produces a drop in the GSC output power. As a consequence, the electrolyser on WT-1 enters the fault mode described in section 3.2.3 and starts to increase its consumption, which will reach the rated capacity of 2 MW at 3.5 s, after an over-consumption peak immediately after the fault (graph b). On the contrary, the electrolyser on WT-2 does not enter fault mode so it decreases its consumption along with the power output drop of the GSC (graph c).

In the meantime, the choppers are expected to dissipate the surplus power, thus maintaining the DC-link voltage close to 1 pu. It can be seen in figure 3.16, graph b, that chopper-1 is activated immediately after the fault to dissipate the power coming from WT-1 which cannot be absorbed by the electrolyser. Chopper-2 is activated only for a very short time at the end of the event (graph c).

The breaker on the faulty cable (HVAC-1) opens 100 ms after the fault has been triggered, as shown on figure 3.16, graph a. The output of GSC-1 expectedly falls to zero as no power can be transmitted through HVAC-1 anymore (graph b). WT-1 enters what is called an islanded mode of operation. It can be seen that the voltage of DC-link-1 rises to reach the natural voltage of the islanded system, close to 1.29 pu (graph d). The other WTs come back to the pre-fault state of operation 0.4 s after the fault has been triggered (graphs c and e) due to two reasons: i) the circuit breakers on HVAC cables 2, 3 and 4 were disabled, as mentioned

previously in this section; ii) the WTs 2, 3 and 4 were able to withstand the fault thanks to the control action implemented in the network (in the GSCs and MMCs) [20].

Due to the extreme character of the event, which is causing a sudden power imbalance in the network, the DC voltage is experiencing abrupt variations (cf. figure 3.16, graphs d and e). This causes major swings for 0.3 to 0.5 s in the buck converter input power, as can be seen on graphs b and d of figure 3.16 (purple line). These large power oscillations look at first sight like a potential danger for the electrolyser. However, the same graphs show that the power swings at the input of the converter are not passed on to the output (green line). Therefore, the power input of the electrolyser (equal to the power output of the buck converter) remains free of chattering during the islanding process and in the islanded mode. The buck converter is decoupling the electrolyser cell from the DC link, which can typically be expected from a DC-DC converter.

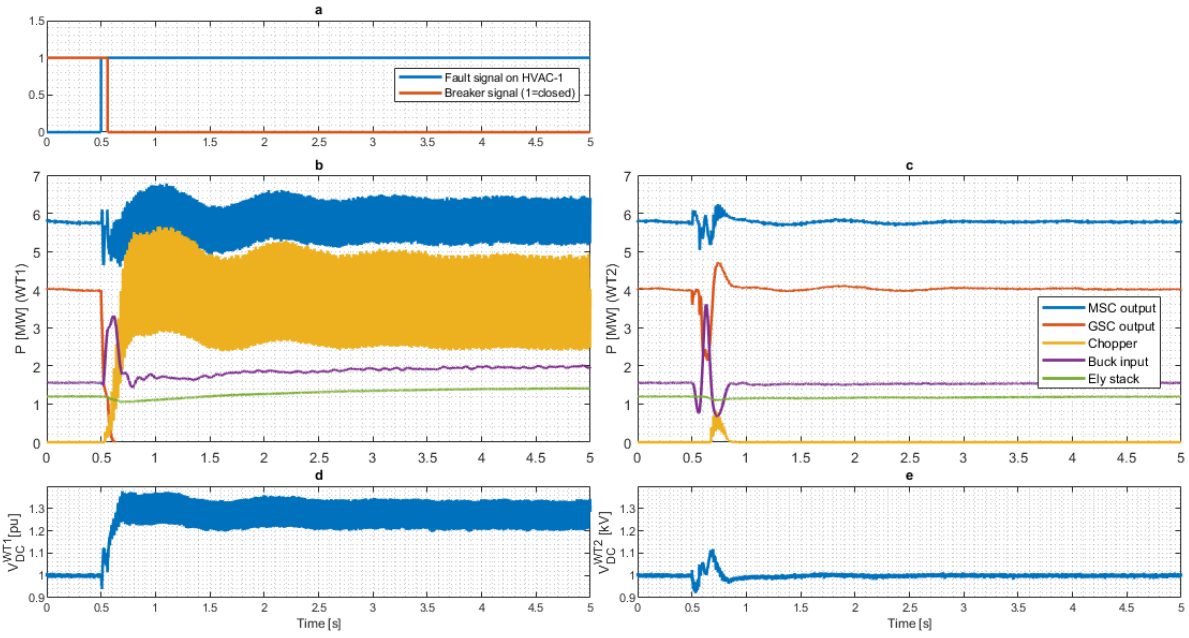

Figure 3.16: Time response of DC link 1 (graphs b and d) and DC link 2 (graphs c and e) under islanding due to three-phase fault on HVAC-1 (graph a)

3.3. Investigation Option C2: Connection on the AC Common Bus

An electrolyser is now connected to the AC common bus of the hub, between the two MMCs, as can be seen in figure 3.17. The model is designed on the basis of a model developed by RTDS Technologies and described in [25]. The initial model was featuring a photovoltaic farm, connected to the grid via a boost converter, a rectifier, a transformer and an interface transformer. The model was implemented in the substep environment and rated at 1 MW.

The main design and control parameters of the electrolyser system of interest in this thesis are summarized at the end of this section, in table 3.2. More details about the other parameters can be found in [25].

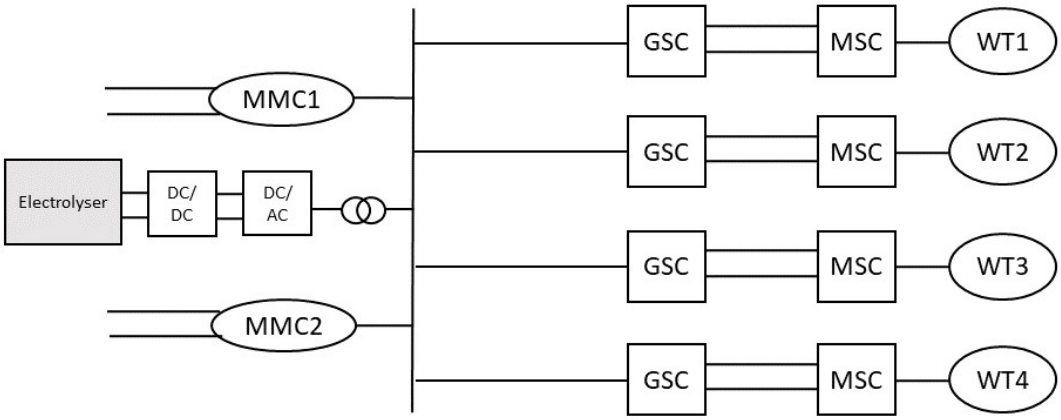

Figure 3.17: Connection of the electrolyser on the AC common bus of the hub

3.3.1. Model Topology and Sizing

The model mentioned above (provided by RTDS Technologies) has been adapted to enable the connection of an electrolyser. When connecting an electrolyser instead of a photovoltaic farm, the power flow is reversed in the system. The voltage of the DC link, set at 0.8 kV, needs to be stepped down to feed the electrolyser. For this purpose, the boost converter initially present in the model is replaced by a buck converter. The layout of the system in depicted in figure 3.18.
In the paragraphs below, some of the main design choices of the buck converter are further explained.

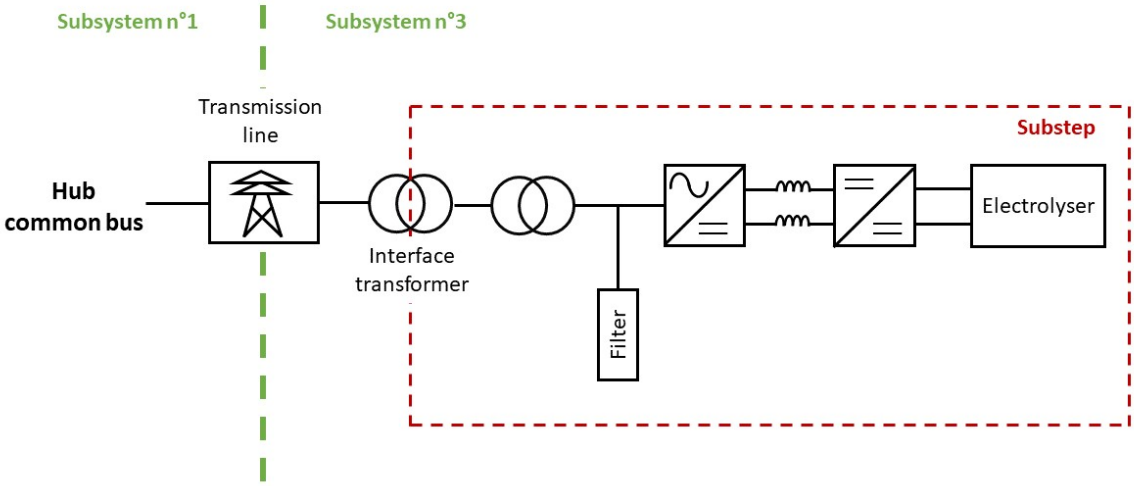

Figure 3.18: Electrolyser model with its rectifier, buck converter and transformers, for connection to the AC bus of the hub

Transmission Line

First of all, an important point is that the electrolyser could not be modeled in subsystem n°1 because the cores available on rack 7 were already fully loaded. Therefore a third subsystem was created to compute the electrolyser system; this subsystem was connected to the main hub via a transmission line E.

The same 15-km transmission line model as the one used to connect the wind turbines to the hub was used. Since the purpose of this line is only to connect subsystems n°1 and 3, there is no desire to introduce some length to the line (and therefore some losses). Consequently the length of the line was set at 1 % of

its total length. However, by doing so, the travel time in the line becomes smaller than the simulation time (50 μs). In this case two options are available [42]:

- Using a Pi section model instead of a travelling-wave model (parameter *alwpi* in figure 3.19): this option is available only if both the sending and the receiving ends of the transmission line are located in the same subsystem, which is not the case here;

- Artificially raising the travel time (parameter *Raistt* in figure 3.19): this option has been selected. However, [42] warns that this will artificially increase the length of the line and can have a significant impact on simulation results. Indeed, a power loss of approximately 3 % is measured between both ends of the line.

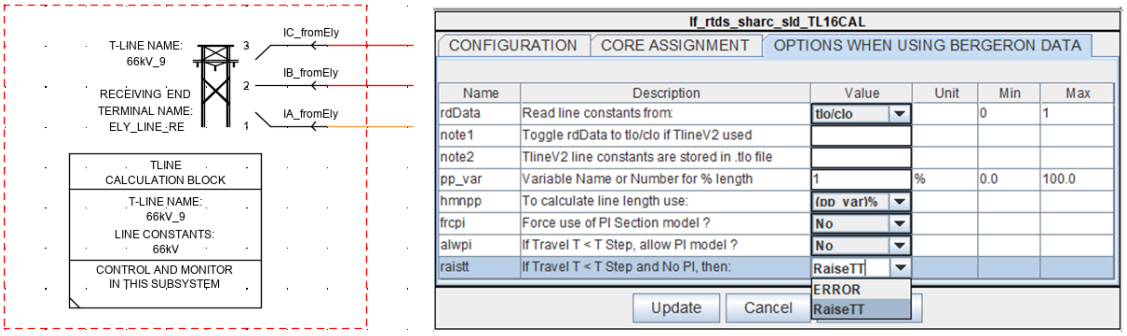

Figure 3.19: Transmission line block and parameters in RSCAD draft file, interfacing subsystems n°1 and 3

Additional Inductance

At first, alternating values of the DC link current were observed. In order to oppose those undesired oscillations, an inductor was connected to each pole of the DC link. An inductor value of 5 mH has been found to lead to the smoothest DC current.

RC Damper

It has been shown that variable impedance systems are prone to oscillations and instabilities. Impedance variations can be due to variable renewable energy production [47] or constant power load components [48]. This common issue can be solved by different types of damping methods. The two main categories of damping strategies are passive methods, which make use of passive components such as capacitors, resistors and inductors, and active methods, based on changes in the control structure of the system [49]. Passive methods might generate more losses that active ones, but they are also much easier to implement. In [47] and [48] the RC parallel passive damping method is investigated.
In this thesis, a resonant behaviour has been observed when connecting the electrolyser system to the common bus of the hub. The issue could be solved by using a RC parallel damper on the substep side of the interface transformer, following the schematic shown in figure 3.20.

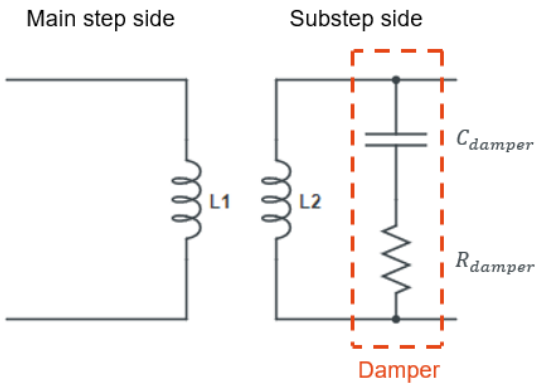

Figure 3.20: Schematic of the damper in the interface transformer

Since the damper parameter tuning methods found in the literature are specific to different topologies from the one used in this work, as a first approximation the following tuning rules were applied:

$$\tau_d = RC = 2 * t_{step} = 100\mu s, \tag{3.9}$$

$$Z_d = 10^3 to 10^4 * Z_{network}. \tag{3.10}$$

Equation 3.9 specifies that the time constant of the damper should be equal to twice the main time step, while equation 3.10 requires that the impedance of the damper is a few thousand times higher than the impedance of the network.

If $Z_d = R_d + \frac{1}{j\omega C_d}$ is the impedance of the damper, Z_0 the impedance of the network and Z_{tot} the impedance of the damped network, we have:

$$Z_{tot} = \frac{Z_0}{1 + \frac{Z_0}{Z_d}} \tag{3.11}$$

It can therefore be seen that the smaller the damper impedance with respect to the network impedance is, the higher the damping effect will be.

The above-mentioned two rules were applied and the parameters $C_d = 1\mu F$ and $R_d = 100\Omega$ were found. However, experimental trials lead to select a smaller value of R_d as specified in 3.2.

3.3.2. Scaling

The electrolyser system in substep environment is rated at 1 MW. To achieve a system rated at 600 MW (i.e. 30 % of the hub rated power), a scaling factor is used. The scaling parameter is located in the substep/mainstep interface transformer, similarly to what has been done previously to scale up each wind turbine with the small time-step/mainstep interface transformers (see section 2.2.2).

3.3.3. Control

The controller of the buck converter is made of two cascaded PI controllers: in figure 3.21 PI-a constitutes the inner loop while PI-b constitutes the outer loop. A third loop is added (PI-d, with output signal $V_{correction}$), in order to maintain the DC link voltage to its rated value of 0.8 kV.

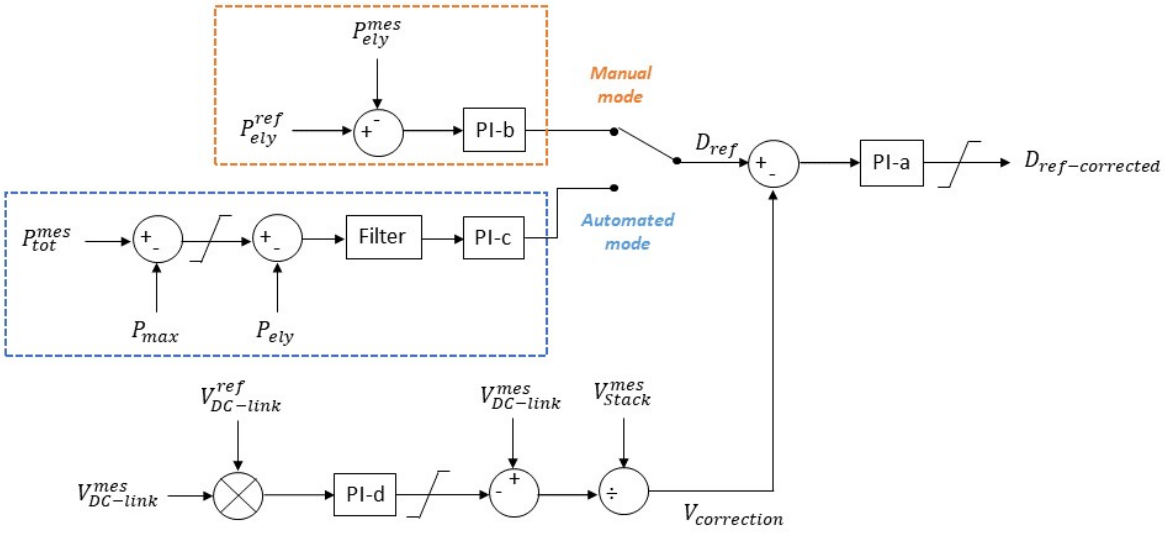

Figure 3.21: Control of the buck converter for the electrolyser connected to the AC common bus

In order to tune the two cascaded PI controllers PI-a and PI-b, a two-stage heuristic method, presented in figure 3.22, is applied. Sensitivity analysis is performed to properly tune each PI controller. The same method is applied in automated control mode to tune PI-c. The tuning of PI-d was done separately beforehand, also with a heuristic method.

As can be seen in figure 3.21, the buck converter can be controlled in two different modes:

- A **manual mode**, in which a power consumption reference is given by the user via a slider in the Runtime interface;
- An **automated mode**, in which the electrolyser is controlled to absorb the power coming from the wind turbine when it exceeds a fixed limit P_{ref}^{max}. This limit can be set by the user via a slide in the Runtime interface.

Damper	**Outer PIs and filter**	**PI-b and c output range**
$C_{damper} = 1\mu F$	$T_b = 0.16s$	0.226 to 1.12
$R_{damper} = 5\Omega$	$G_b = 1.5$	**PI-a output range**
Inner PI	$T_c = 0.4s$	0.22 to 0.99
$T_a = 0.06s$	$G_b = 1.9$	**DC-link inductance**
$G_a = 1$	$T_{flt} = 0.04s$	$L_{DC-link} = 5mH$
Buck switching frequency	$T_d = 1s$	**Electrolyser stack**
$f_{sw} = 2kHz$	$G_d = 1$	$R_{stack} = 0.4\Omega$
Buck capacitors	**Scaling factor**	$V_{OC} = 0.155kV$
$C_{out} = 30mF$	$S_{ely} = 600$	
$C_{in} = 32mF$		

Table 3.2: Summary of the main parameters used in the electrolyser system model

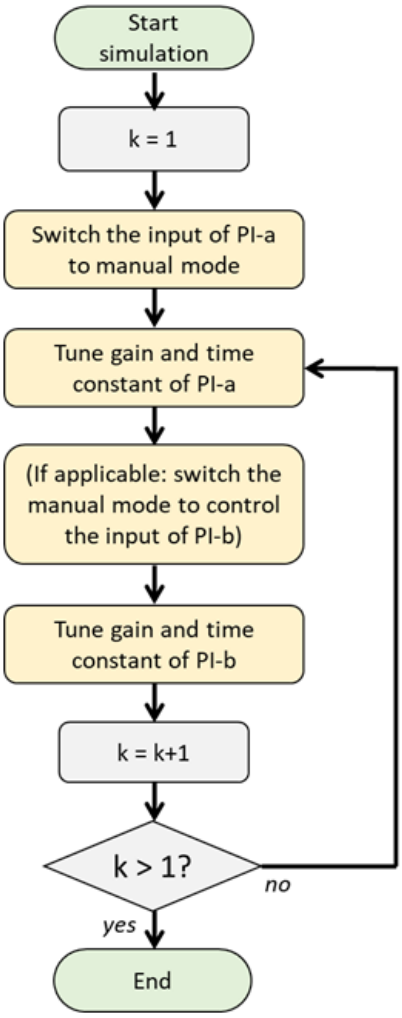

Figure 3.22: Tuning method of the cascaded PI controllers in the buck converter controller, using incremental variation of the time constant and gain values

3.3.4. Results

Two simulations have been performed with the electrolyser system connected on the AC bus: first a unit power consumption step was applied to the electrolyser in manual mode, secondly a wind speed step is applied to the hub while the electrolyser is in automatic mode.
For the figure presented in this section, power measurements, as well as AC voltage measurements, were filtered with a time constant of 0.01 s. DC current and voltage measurements are not filtered.

Power Step

In this section, the hub wind speed is fixed to the rated speed of 16 m/s and the electrolyser is put in manual mode. Initially the power reference sent to the electrolyser is 0. The power reference is then increased to 1 pu (equals to 1 MW in the non-scaled substep model) as can be seen on the blue curve on the first graph of figure 3.23. It is important to note that here, a step function was chosen as it represents an extreme scenario. In reality, a ramp would be applied.

To evaluate the response of the network to this power step, power and voltage measurements were plotted in figure 3.23. The red curve on the first graph represents the power measured at the electrolyser stack itself (output of the buck converter). It can be observed that the power first increases sharply for a few milliseconds, before the PI input stabilizes. The settling time, which is the time needed for the power output to increase

from 10 % to 90 % of the set-point, can be calculated: it is equal to 0.35 s.

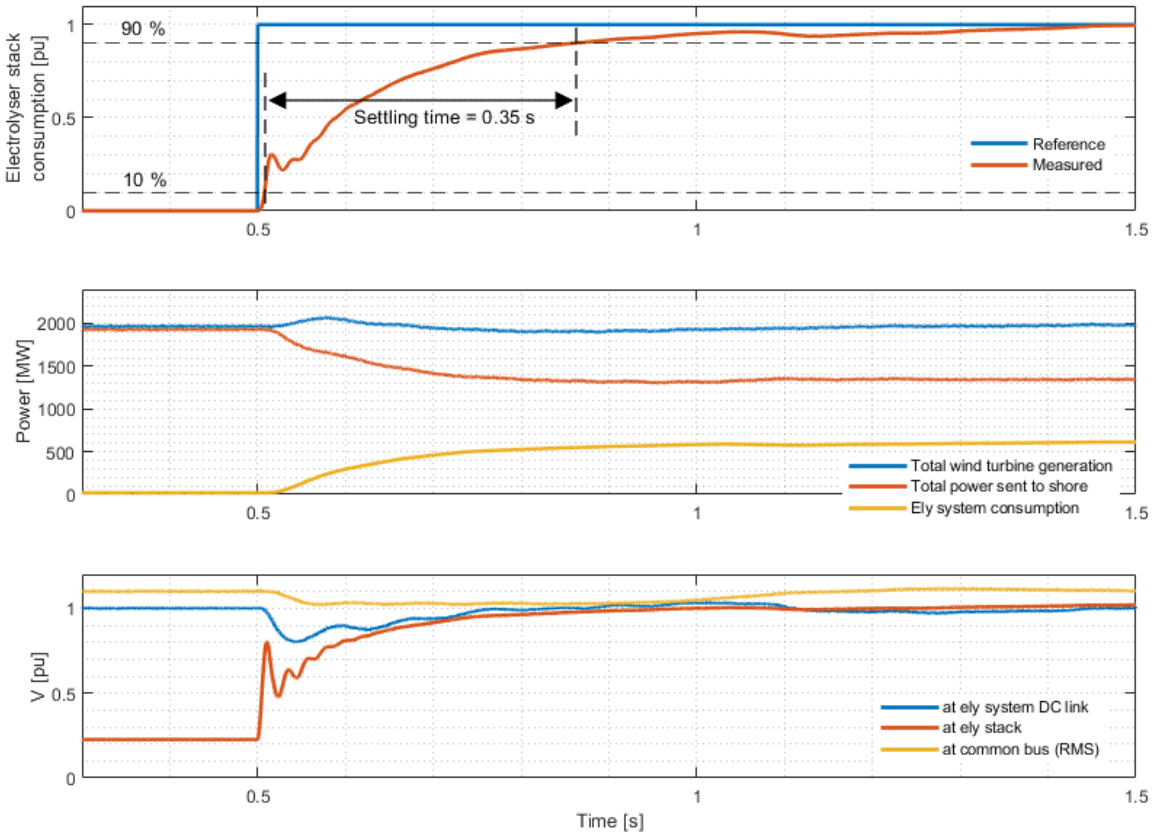

Figure 3.23: Hub response to a 1 MW power consumption step of the electrolyser connected to the common bus

The power flow in the hub can be understood thanks to the second graph of figure 3.23. All measurements are done at the feeders connected to the common bus. The blue line shows the total power generated by the wind turbines; the red line is the power going through the HVDC transmission link to the shore; the yellow line shows the power absorbed by the complete electrolyser system, including converters and transformers. Initially, the power generated is entirely transferred to the shore, except for 40 MW which are consumed by the electrolyser. Indeed, at this stage the circuit breaker between the electrolyser and the common bus is closed, so even though the power reference is 0, a small amount of power is still consumed by the electrolyser system. Half of this power (20 MW) is lost in the transmission line as explained in 3.3.1. The balance $P_{gen} = P_{HVDC} + P_{ely}$ is respected at all times.

On the third graph, different voltage measurements can be seen. The blue line represents the voltage at the DC link of the electrolyser system (between buck and GSC). This voltage is maintained constant thanks to the GSC controller and the additional PI-d loop in the buck controller. It can be observed that apart from a small dip when the step is applied, it remains fairly constant at 1 pu.

On the same graph, the yellow curve shows the RMS value of the AC common bus voltage. This voltage is maintained as close as to 1 pu as possible by MMC-1. Nevertheless, a small increase of the voltage of 0.2 pu is observed when the wind speed increases.

Finally, the voltage of the electrolyser stack (in red on the third graph) is stepped up from the open-source voltage value to its nominal value. This is the expected effect of the buck controller logic.

Wind Speed Step

In this section, the hub wind speed is initially fixed at 11 m/s. At t=1 s, the wind speed is stepped up to 15 m/s. A first order filter with time constant T=0.5 s is applied. The resulting input wind speed is shown on the first graph of figure 3.24. It should be noted that the same wind speed input is applied to all wind turbines.

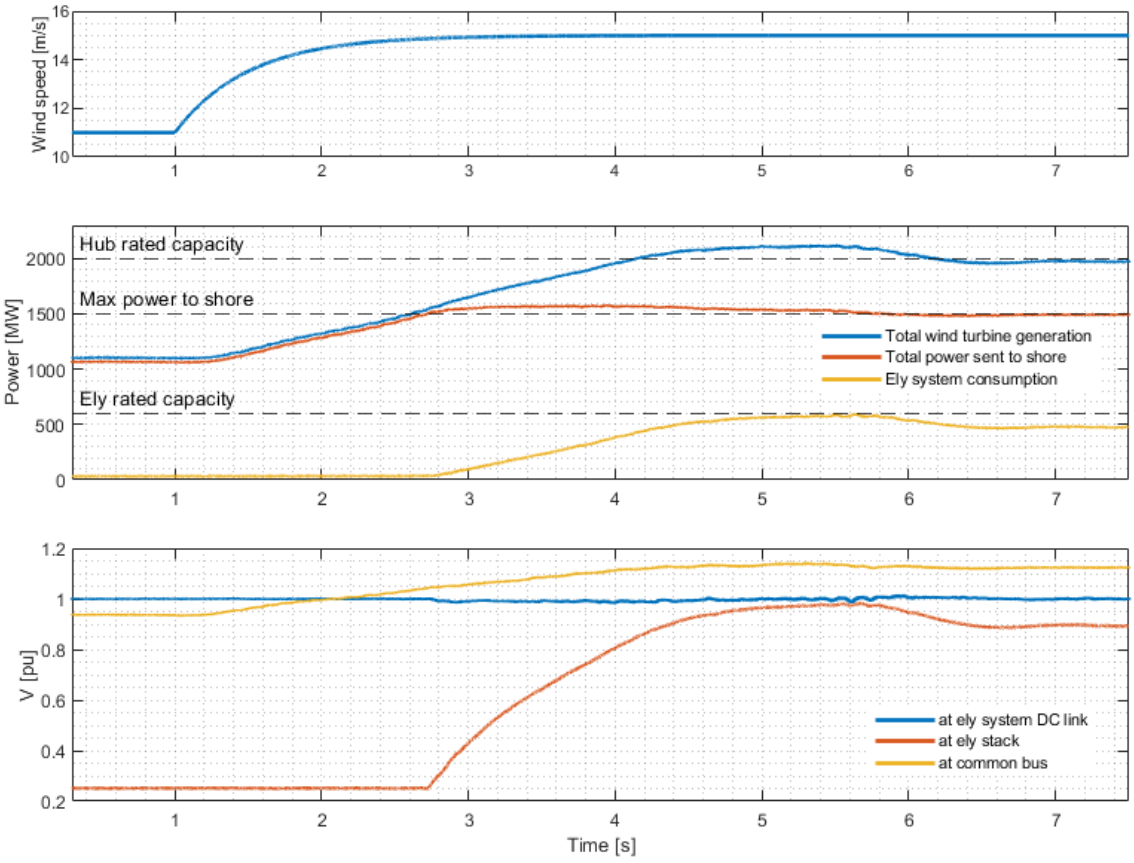

Figure 3.24: Hub response to a wind speed step from 11 to 15 m/s, with an electrolyser connected to the common bus

Moreover, the electrolyser is now in automated mode. This is done thanks to a switch in the buck controller, as can be seen in figure 3.21. In automated mode, the logic of the buck controller is the following:

$$P_{ref,ely} = \begin{cases} 0 & if\, P_{gen} \leq P_{max} \\ P_{gen} - P_{max} & if\, P_{gen} > P_{max}, \end{cases}$$

where P_{gen} is the total power generated by the wind turbines and P_{max} is the maximal power which should be transmitted to the shore. This parameter can be selected by the user and was set to 1500 MW in this section.

On the second graph of figure 3.24, the power measurements of the feeders connected to the common bus have been plotted. When the generated power reaches 1500 MW, the electrolyser starts to consume power, with a delay of about 0.2 s. This delay causes an overshoot of about 100 MW in the power transmitted to the shore, after which the electrolyser consumption settles in a steady-state. In the steady-state the power transmitted to the shore is exactly 1500 MW, as expected.

On the third graph of figure 3.21, voltage measurements have been plotted. It can be seen that the buck input voltage (in blue) is maintained to its rated value. The RMS of the AC voltage at the common bus of the hub increases from 0.95 to 1.15 pu. This behaviour was also observed when the electrolyser was not

connected and is due to the increase in the generated power. The controller of MMC-1 is responsible for the AC voltage control. Since it fails to maintain it at rated value, another loop (for example a reactive power loop in MMC-2) could be implemented.

Wind Speed Profile

In the previous section, a standard wind speed step was applied the network. In this section, the goal is to test the system under real-life conditions. For this purpose, several sample wind profiles have been selected in appendix D. Here the results under the most challenging profile (profile n°2, high wind speed gradient) are presented in figure 3.25. Once again the electrolyser is in automated mode. In this simulation, the capacity of the electrolyser was increased to 800 MW to be able to cope with the challenging wind speed. This was done by adjusting the electrolyser scaling factor in the Runtime file. All control parameters were kept identical to the previous case, except for the gain of the outer PI in the buck controller, which was set to $G_d = 0.85$.

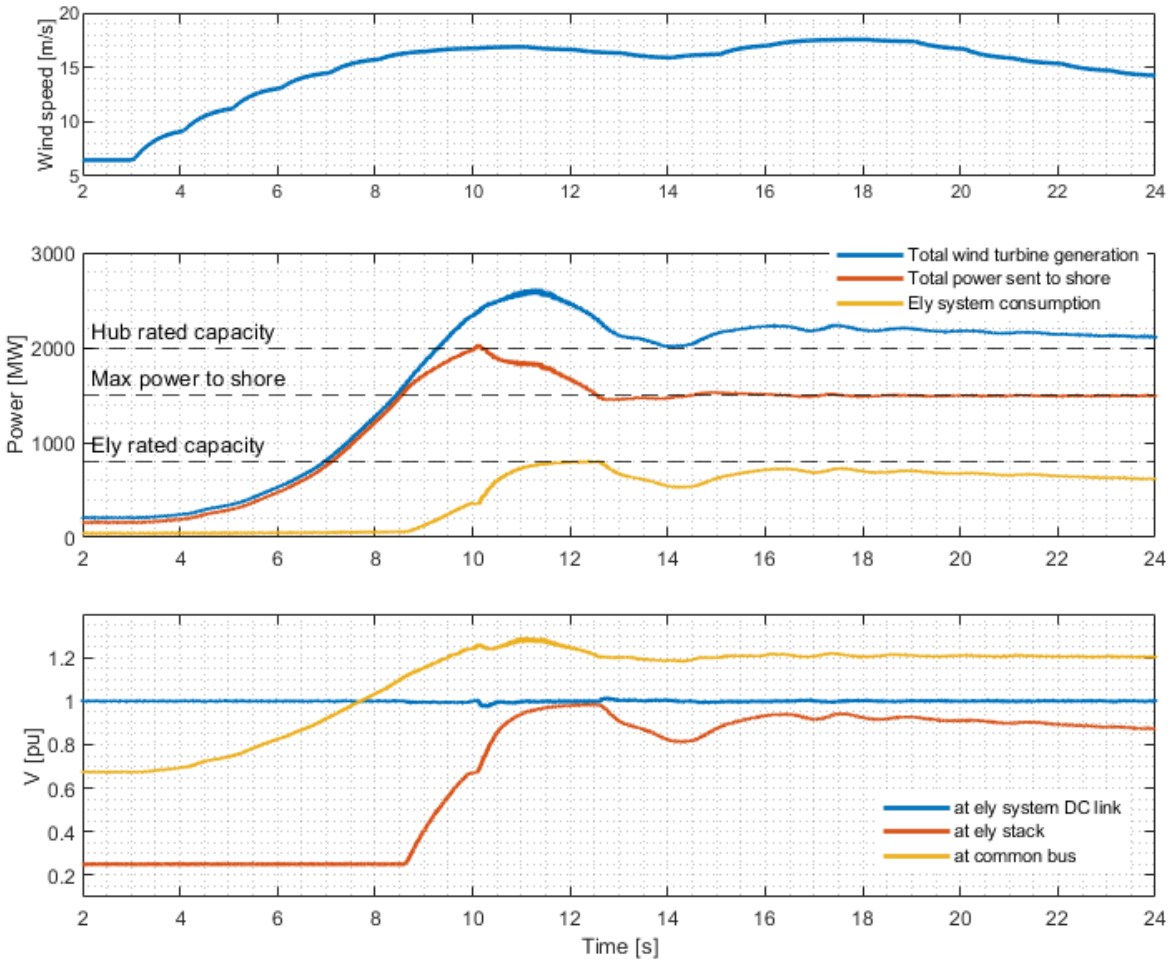

Figure 3.25: Hub response to a the wind speed profile n°2, with an electrolyser of capacity 800 MW connected to the common bus

As a reminder, in automated mode, the electrolyser should consume excess generated power, so that the power transmitted to the shore does not exceed 1500 MW (indicated by a dotted line on the second graph in figure 3.25). It can be seen that between 9.5 s and 13.5 s, this rule is not respected. There are two reasons for this mismatch. First, between 9.5 s and 11.5 s, the power in the HVDC link crosses the limit of 1500 MW because the rise time of the electrolyser is too slow to cope with the high wind speed gradient of 1.59 m/s^2. Secondly, from 11.5 s to 13.5 s, the electrolyser consumption is saturated at its rated capacity. During this interval, the total power from the wind turbines is higher than the hub rated capacity, because the high wind

gradient produces a generation overshoot. Once the generation becomes stable again, from 13.5 s, a steady amount of power is transferred to the shore. Particularly at 15 s, the electrolyser adjust its consumption to match the wind profile. However, the electrolyser capacity is limited and cannot follow the small fluctuations of power between 16 s and 19 s.

As can be seen on the third graph of the same figure, the voltage of the DC link between the electrolyser rectifier and buck converter (blue line) is maintained at its nominal value even under the high wind speed gradient.

3.4. Conclusion

In this chapter, two different locations for the connection of the electrolyser have been investigated.

In the first option, an electrolyser was connected to the DC link of the back-to-back of each WT. Connecting electrolysers locally at each WT proved to be a great advantage to mitigate power variations flowing to the common bus of the hub, due to increasing wind speed. More simulations shall be carried out to further study this option under different possible patterns of wind speed fluctuations. The simulation also showed interesting results when a wind turbine had to be islanded due to an AC fault. In this case, the electrolyser could consume some of the power produced by the islanded WT.

In the second option, an electrolyser was connected to the common bus of the hub. In this case, some resonance phenomena were first observed between the electrolyser system and the rest of the network. After a damper was added, the electrolyser showed promising results both in manual and automated mode of operation. The parameters of the controllers could be optimally tuned to match experimental response-time data of a PEM electrolyser stack.

It can be concluded that both connections show interesting features. Connecting an electrolyser to each wind turbine would require more converters (one for each turbine) while only two converters (rectifier and buck) would be necessary if the electrolyser is connected to the common bus of the hub. The first option could however be less space-consuming as electrolysers can be placed inside the structure of the turbines, like in the project described in [16]. It would also be useful in case of islanding of one of the turbines, contrary to the second option.

4

Development of a Control Strategy for the Offshore-Onshore HVDC Bipolar Link

As seen in chapter 2 (section 2.2.5), in the initial model, the hub is connected to the shore via two symmetrical monopolar HVDC links. In this chapter, the topology of the HVDC link is changed to a bipolar link with ground return, as the later topology proved to be more reliable and flexible than the former one [11]. In the new model with bipolar topology, each pole is formed by one MMC on each side, which results in a total of two onshore and two offshore MMCs. Monitoring the share of power flowing through each pole of a point-to-point bipolar link is an interesting feature which has not been covered in literature so far. It would be useful especially to handle maintenance events or failures on one of the poles. In order to enable power sharing capabilities between the two poles of the bipolar link, in this chapter, a new control strategy is implemented in the outer loop of the controller of one of the offshore converters. It is then investigated if the expected performances of the control strategy are met.

4.1. Literature Review

VSC-HVDC transmission links are a key technology for the development of a reliable sustainable power grid. Not only can they help to reduce losses in long-distance transmission configuration, but they can also participate to provide diverse ancillary services, such as reactive power injection and black-start capabilities, and therefore support the grid [11]. Unlike LCC technology, VSC technology is also able to operate when connected to a very weak AC grid [11]. Knowing that offshore wind hubs are considered as weak grids, this is a determine criteria for the choice of the technology. However, the VSC technology is very costly and recent, hence a lack of operational experience and standardisation. It is stated in [50] that in 2019, no operational experience of networks of capacity above 2 GW and voltage above ±500 kV was available.

Even though examples of VSC bipolar links remain scarce, some examples of HVDC links already in use can be mentioned: BritNet between the United Kingdom and the Netherlands (two LCC monopoles); SAPEI between Sardinia and Italy (LCC bipole); INELFE between France and Spain (two VSC monopolar links) [11]. However, it should be noted that the above-mentioned links are interconnectors operating between two countries, which can be considered as strong grids. There is a lack of knowledge about the performance of such interconnectors (especially for the bipolar configuration) when they are connected to a weak grid, such as an offshore wind farm. Some aspects of this research gap are investigated in the present work.

4.2. Upgrade of the Offshore-Onshore HVDC Link to a New Topology

4.2.1. Use of a Point-to-Point Bipolar HVDC Link

A HVDC link can be either in a point-to-point configuration (two terminals connected together) or in a multi-terminal configuration (at least three terminals connected together). In this thesis, due to the focus of the research on the power transfer control between an offshore hub and an onshore power system, only point-to-point configurations are investigated.
In the model taken from [20], two offshore MMCs were connected to the shore via two independent pairs of

HVDC cables. This topology is called a symmetrical monopole (cf. figure 4.1-e). The adjective symmetrical refers to the fact that one cable has a positive voltage and the other a negative voltage, both with the same absolute value. Contrary to an asymmetrical monopole, none of the poles is connected to the ground (cf. figure 4.1). Even though this topology has lower investment costs than the bipolar topology, it is not suitable for interconnecting offshore hubs with the shore due to its low flexibility and redundancy, and its lower transmission capacity compared with bipolar links [11].
Links with a bipolar topology, in which two MMCs are connected at each side of the HVDC link, are mainly developed nowadays because this topology has several advantages. First, in case of a converter outage or a line outage, half of the total capacity can still be transmitted by switching to a monopolar type of operation [51].
Moreover, this topology allows for more operational margin to safeguard a certain transfer capacity: in case of unavailability of one pole, it is still possible to transfer half of the total rated capacity by using the user pole [51], [11]. For example, in case of planned maintenance on one pole, this pole could be unloaded thanks to an appropriate control strategy, to allow for an isolation of the cable without the use of expensive, bulky DC circuit breakers. The next section focuses on such a control strategy.

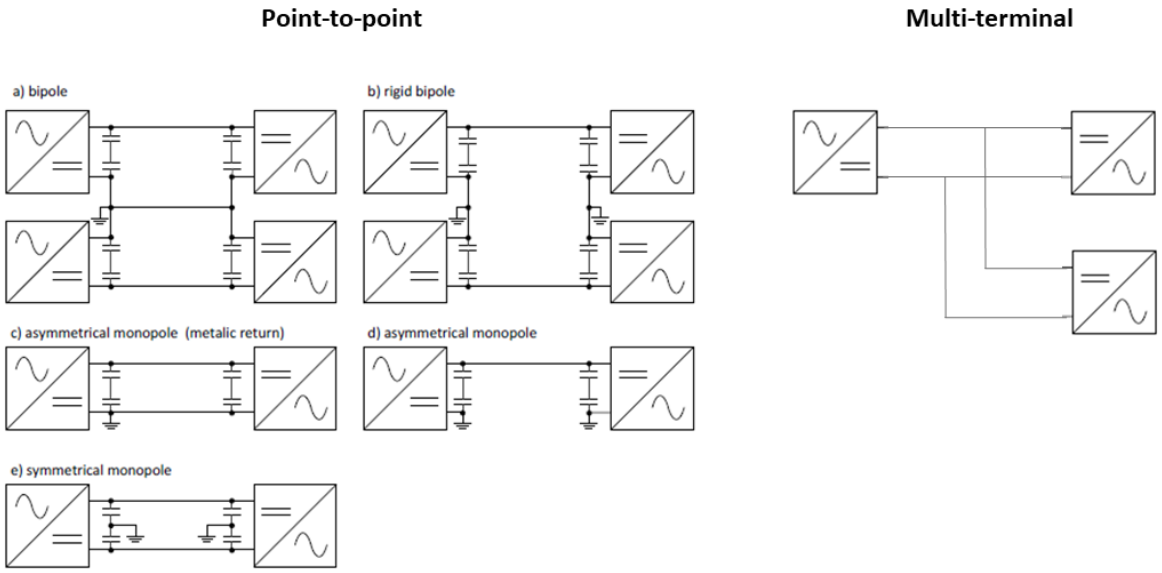

Figure 4.1: Common HVDC topologies (adapted from [11])

4.2.2. Addition of Onshore MMCs

The second step of the upgrade of the model of the HVDC link was to include two offshore MMCs, to replace the two voltage sources used in the initial model (taken from [20]) to represent the onshore terminal of the link. The main reason why onshore MMC models are used instead of ideal voltage sources is that potential major interaction issues between offshore and onshore MMCs (such as the impact of the offshore grid forming control on the onshore DC control, as mentioned in [52]) can be observed. Hence the use of onshore MMCs models allows to properly capture the dynamics in the offshore-onshore power transfer. The implemented topology of the HVDC link can be seen in figure 4.2.

The two onshore MMCs have been named as MMC-3 for the positive pole and MMC-4 for the negative pole. They are connected to an AC source which represents an equivalent of a strong onshore power system. The RSCAD component used for the source and its technical specifications can be seen in figure 4.3. In future work, this source could be replaced by a synchronous generator tuned to model a weak grid, thus assessing the robustness of the link in case of a connection to a weak onshore grid.

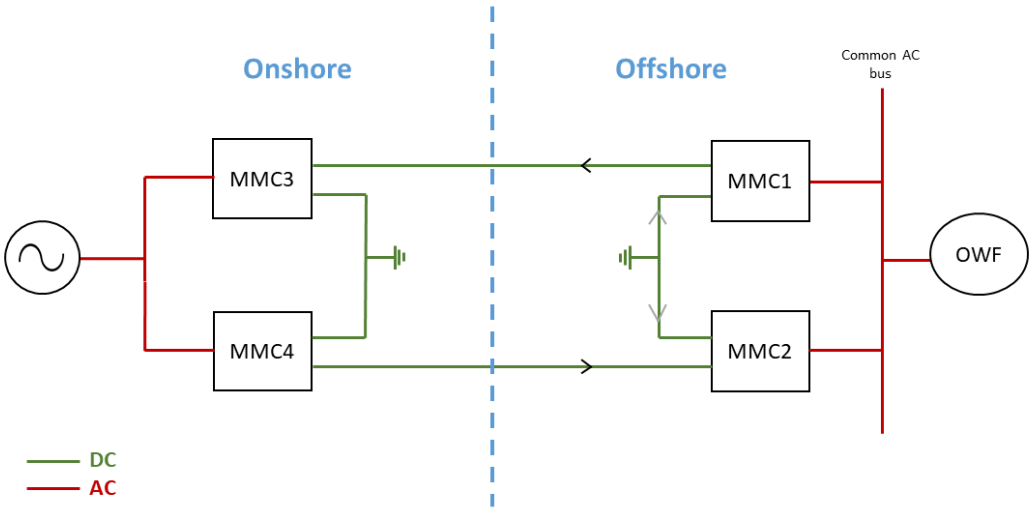

Figure 4.2: Implemented topology of the HVDC link

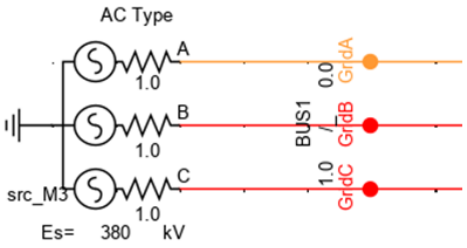

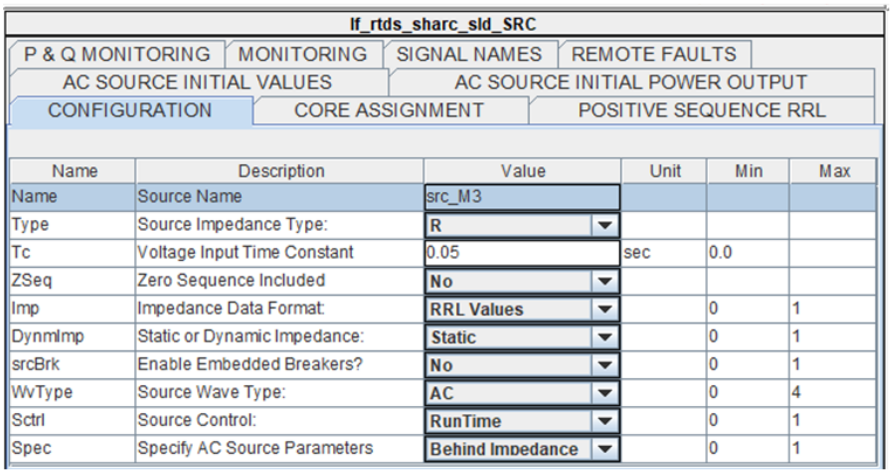

Figure 4.3: RSCAD component used to model the AC source representing an equivalent of an onshore power system ($R = 1.0\Omega$), and its property window

Model and Control

The models of MMC-3 and MMC-4 are identical to the models of MMC-1 and MMC-2 already implemented in [20]. These models are derived from a model developed by RTDS and available in the RSCAD library under Samples>Small time-step>MMC5. Each newly implemented MMC has a nominal capacity of 1 GW, and an architecture visible in figure 2.10. The two onshore converters are controlling the DC voltage at each pole of

the link. MMC-3 and MMC-4 form the onshore terminal of the HVDC link, while MMC-1 and MMC-2 form the offshore terminal. The HVDC link in the completely upgraded configuration is thus a two-terminal, four-converter link.

Core Assignment in RSCAD

There are three NovaCor chassis available at TU Delft (cf. 2.1.2). Initially, the simulation was running on two chassis of four cores each [20]. However, with two additional MMCs, the simulation became too computationally heavy to be run on only 8 cores. Therefore, the use of a third chassis is necessary. To this end, a third subsystem is created in the draft file. More information about the relation between subsystems and chassis can be found in appendix E. The onshore MMCs are placed in this third subsystem, and computed on the third processor, as indicated in figure 4.4.

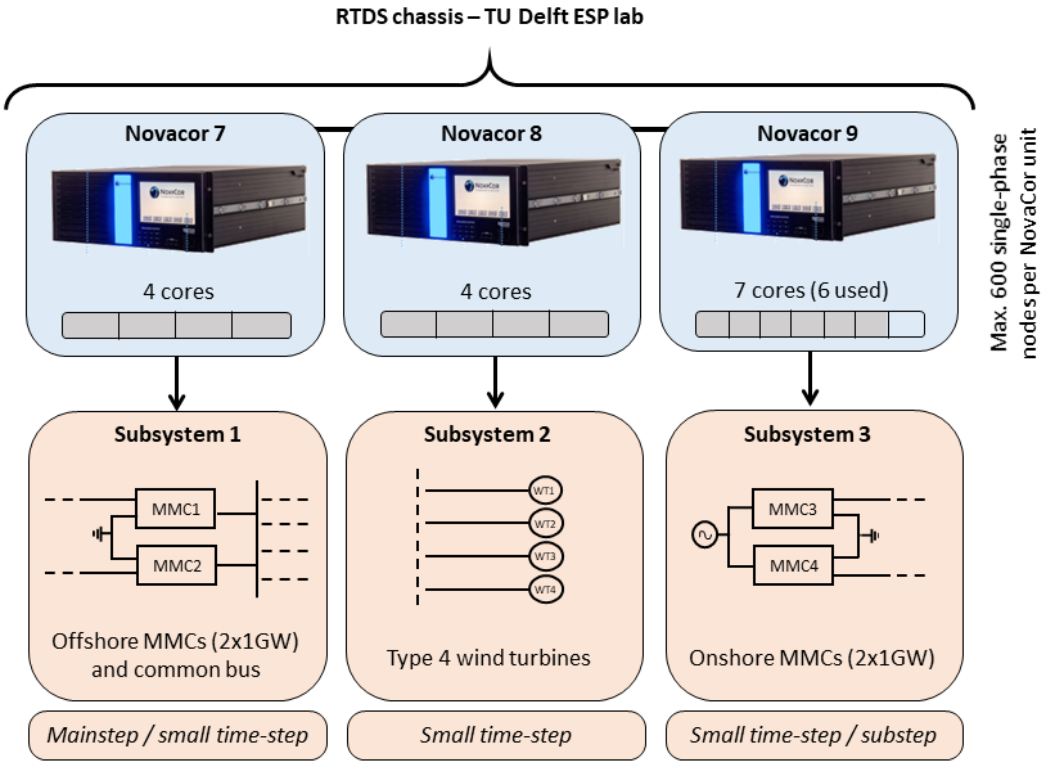

Figure 4.4: Summary of the distribution of the different parts of the network among the NocaCor chassis

4.3. Control Strategies for the Outer Active Current Loop of MMC-2

4.3.1. Active and Reactive Current (i_d/i_q) Decoupling

In the model used as the starting point of this thesis, MMC-1 sets the reference angle of the voltage. Based on this reference, the GSCs (inverters) of the wind generators, which are grid following (in non-islanded mode), modify the local voltage angle at their terminal in order to control the power flowing through the HVAC cables. MMC-2 is grid following. It is responsible for determining the share of active power flowing through each converter. The control strategy used to achieve this power sharing is the decoupling of active and reactive current. Indeed, the total complex power S flowing through one of the MMCs can be written as the product of the complex voltage and complex conjugated current:

$$V = V_d + jV_q, \tag{4.1}$$

$$I = I_d + jI_q, \tag{4.2}$$

$$S = P + jQ = VI^* = (V_d I_d + V_q I_q) + j(V_q I_d - V_d I_q). \tag{4.3}$$

If we now set $V_q = 0$, as it is done in the Phase Lock Loop (PLL), the equation of S is simplified to

$$S = P + jQ = V_d I_d - jV_d I_q, \tag{4.4}$$

from which can be derived the expression of the active power

$$P = V_d I_d. \tag{4.5}$$

It can be seen from equation 4.5 that the active power flowing through MMC-2 P is proportional to the active current I_d flowing through this same MMC. It is therefore possible to control P by changing the active current reference of MMC-2. In order to set this active current reference, an outer loop is created in the controller of MMC-2. The outer loop takes as input active power the set-point required by the user, as well as current and voltage measurements. The outputs of the outer loop are the active (and reactive) current references (the reactive current reference is actually kept equal to 0). These references are then passed on to the inner loop, which outputs the modulation waveforms used to control the submodules of the MMC. This control scheme is depicted in figure 4.5.

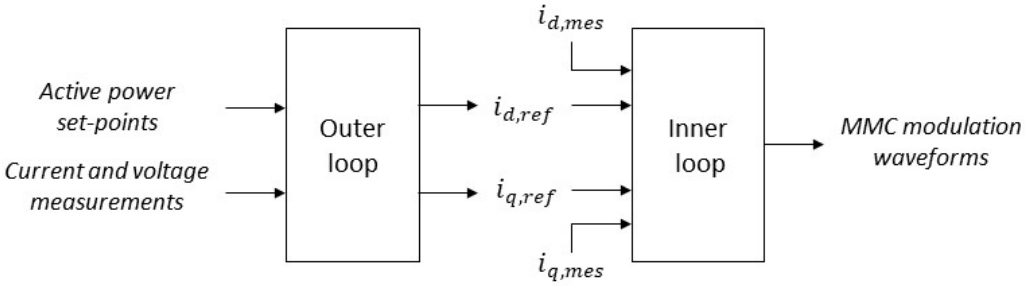

Figure 4.5: Outer and inner loop control scheme

It should be noted that in the baseline model, the outer loop is reduced to:

$$i_{d,ref} = I^d_{ref}, \tag{4.6}$$

$$i_{q,ref} = 0, \tag{4.7}$$

where I^d_{ref} is provided by the user via a slider in Runtime. This simplified mode of operation is kept as such during the initialisation phase of the simulation (see appendix A). A dial is used in Runtime to switch from the simplified outer loop to the more advanced ones, developed in this chapter. It can be seen in figure 4.6.

The higher I^d_{ref}, the more active power flows through MMC-2. The remaining power flows through MMC-1 based on the following equation of nodal power balance:

$$P_{mmc1} = \sum_{n=1}^{4} P_{GSCn} - P_{mmc2}.$$

In case of variable conditions (fault, variable wind speed), the active power flowing through MMC-2 will be constant, while the active power flowing through MMC-1 will vary. There is no power sharing control implemented in the initial model.

The main goal of this chapter is to implement different power sharing strategies in MMC-2 and ascertain their potential. Three strategies are presented in the following sections.

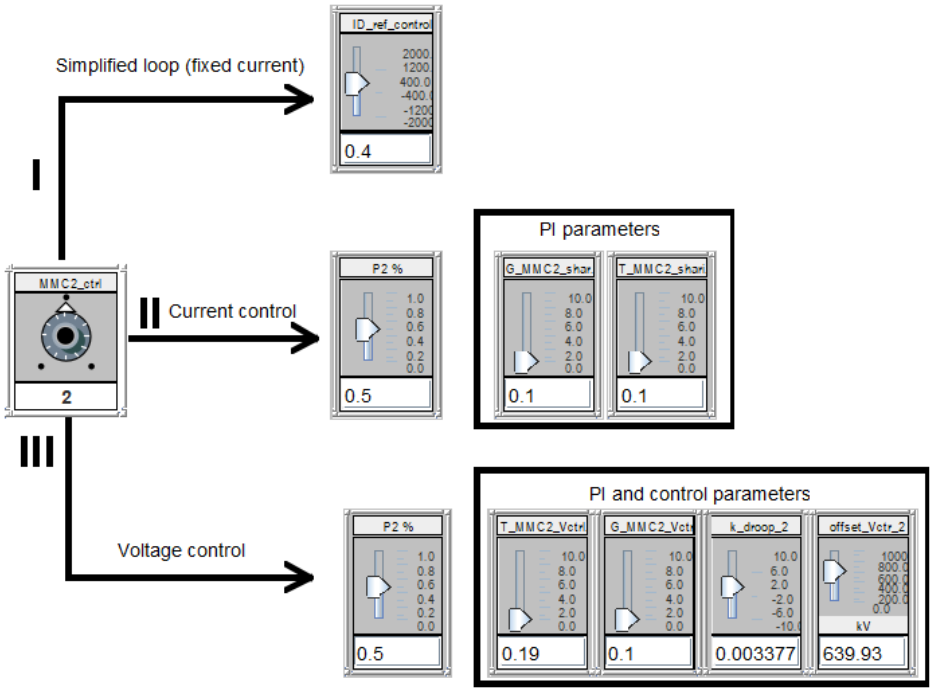

Figure 4.6: Selector for MMC-2 outer loop in Runtime

4.3.2. Direct Power Control and DC Current Control

Control Scheme

A first and straight-forward manner to control the active power flowing through MMC-2 is to directly compare the AC power measurement with the desired power level, and feed the error to a PI controller which generates the active current reference, as shown in figure 4.7 (green inputs). The output of this loop, $i_{d,ref}$, is the reference for the direct current mentioned in equation 4.5. As can also be seen in the same figure, an anti-windup mechanism is added to prevent saturation of the integrator, as explained in appendix C. Without the anti-windup mechanism, oscillations and long settling times are observed.

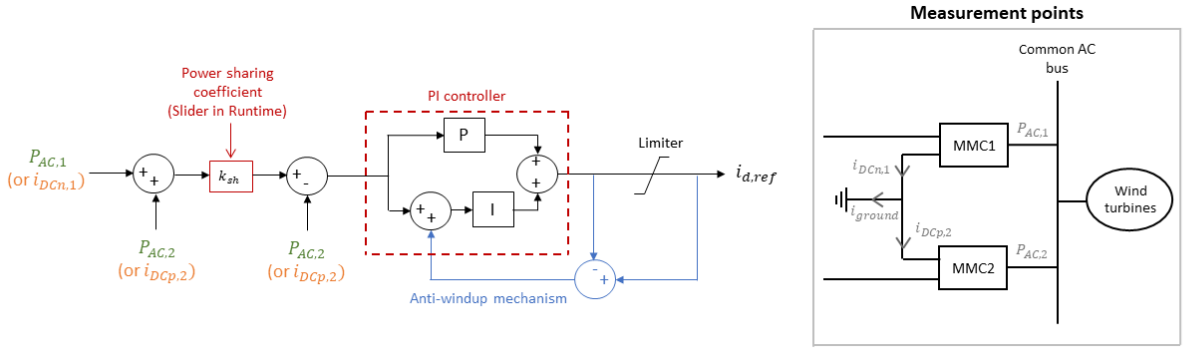

Figure 4.7: Outer loop of MMC-2 for AC power control (in green) or DC current control (in orange) modes

A second control strategy is based on DC current control: the same control structure as previously is kept, but the signals used to generate the reference are now measured on the DC side (orange inputs in parentheses in figure 4.7). The underlying principle is that in balanced operation (i.e. when the same amount of power flows through each converter) the ground current i_{ground} must be equal to zero. In that way, both pole will be operated in a symmetrical manner regarding current, power and voltage. The zero ground current condition

is expressed thanks to the following equation:

$$i_{ground} = i_{DCn,1} - i_{DCp,2} = 0, \tag{4.8}$$

which translates into the following condition on MMC-2 output current:

$$\left(\frac{i_{DCn,1} + i_{DCp,2}}{2}\right) - i_{DCp,2} = 0. \tag{4.9}$$

Therefore, in balanced conditions, the goal of the PI controller in the new control strategy is to nullify the ground current, using equation 4.9. Current measurement points are indicated in figure 4.7.
In order to vary the share of power flowing through each MMC, a coefficient k_{sh} is introduced:

$$\left(\frac{i_{DCn,1} + i_{DCp,2}}{k_{sh}}\right) - i_{DCp,2} = 0, \tag{4.10}$$

with $k_{sh} = 2$ in balanced conditions.

Results

To ascertain the performance of both types of control, a wind speed drop from 15 to 10 m/s is applied over the whole hub, as a step disturbance. The power generated by the offshore hub is therefore decreasing. The goal is to check if the controller is able to maintain an equal share of power flowing through each MMC in spite of the power drop.
As can be seen in figure 4.8, the AC power control does not produce satisfactory results since a lot of oscillations are observed. Indeed, any disturbance from the offshore side is passed on to the DC side because the reference of the controller is generated from disturbed signals. On the contrary, the DC current control performs as expected, the current remains stable and balanced between the two poles. Therefore, in the following work, only the current control is further investigated, along with the voltage control, which is presented in section 4.3.3.

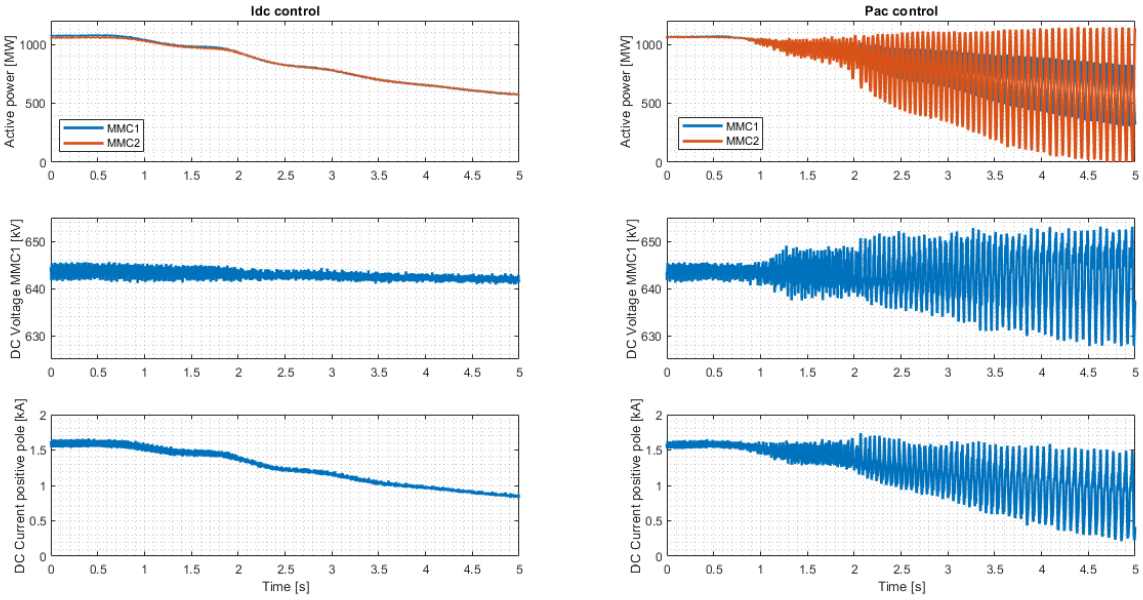

Figure 4.8: MMCs time responses when operating under I_{DC} and P_{AC} control strategies for active current reference generation in MMC-2, under wind speed downward step from 15 to 10 m/s

4.3.3. DC Voltage Control

The power sharing control strategy presented in this section has been developed during this work, and is inspired from the DC voltage droop control, which is the common control strategy used in MTDC systems for power balancing between the multiple converters [32, 53].

The principle of DC voltage droop control is to measure the active power deviation (from a power reference) and adapt the value of the DC voltage to oppose this deviation. The magnitude of the reaction to a power deviation is determined by the droop coefficient k_{droop}, which is negative and selected by the user. In case of a power deviation event, the deviation will be absorbed by all the converters constituting the system in order to remain in a balanced situation. The droop control prevents for example that only one of the converters absorbs all the power deviation. The droop method is based on the proportional relation which can be written between the voltage difference between both ends of a line, and the power flowing through this line [53]:

$$V_{DC,ref} = V_0 + k_{droop} * (P_{mes} - P_0), \tag{4.11}$$

where the subscript 0 indicates the reference value achieved with power flow calculation [32]. The implementation of equation 4.11 in the outer loop of a MMC can be seen in figure 4.9(a).

In the DC voltage control implemented here, however, the goal is not to adapt the DC voltage as response to a power deviation (as for droop control), but to modify the DC voltage in order to achieve a different distribution of the active power between the two offshore converters. In order to do so, the power deviation between an active power reference determined by the user and an initial (arbitrary) reference is calculated, and multiplied by a positive coefficient k_{P-V} in order to produce a DC voltage reference, according to equation 4.12:

$$V_{DC,ref} = V_0 + k_{P-V} * (P_{ref} - P_0), \tag{4.12}$$

where the initial reference point $(V_0, P_0) = (640kV, 0MW)$ has been (arbitrary) chosen to be the origin of the P-V slope which can be seen on the graph 4.10. The power reference is the product of the measured AC active power at the common bus of the hub and a coefficient between 0 and 1 which can be varied by the user thanks to a slider in the Runtime file. The implementation of this control scheme in the outer loop of a MMC can be seen in figure 4.9(b).

The coefficient k_{P-V} has been calculated based on graph 4.10, generated following the method described in figure 4.11. The P_{AC}-$V_{DC,mmc2}$ curve on graph 4.10 was then fitted by a linear function, the coefficient k_{P-V} being the slope of this function.

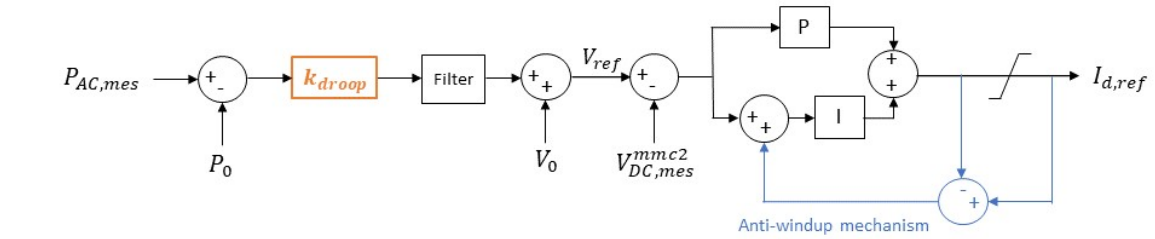

a. Traditional droop control method

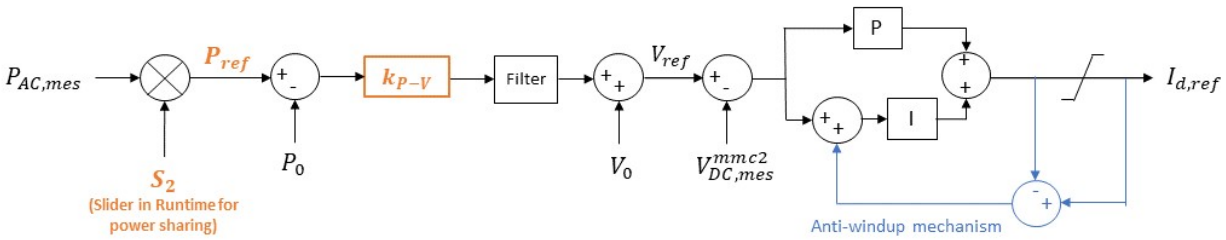

b. Developed P-V control method

Figure 4.9: Outer loop of MMC-2 for DC voltage control mode

It is important to note that the goal of this control strategy differs from the traditional droop control. Indeed, in the traditional droop control, a coefficient is *chosen* so that the converter adapts its voltage according to the incoming power. Here, a coefficient has been *measured* so that the converters transfers the desired amount of power when given a certain voltage reference.

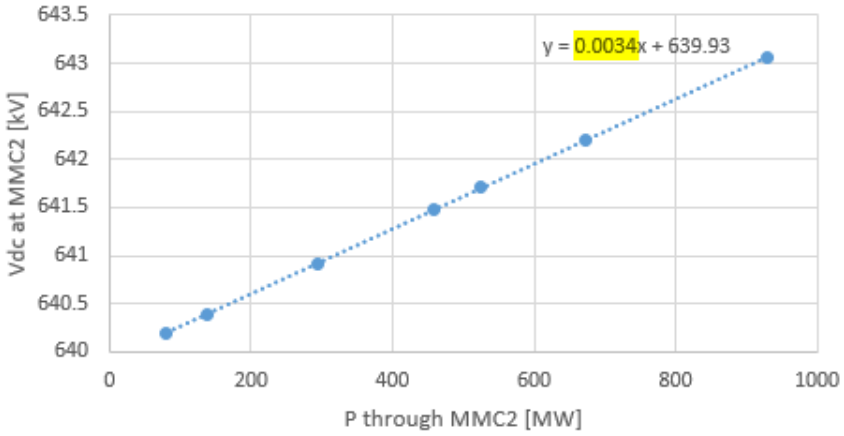

Figure 4.10: Power-Voltage graph for MMC-2 control

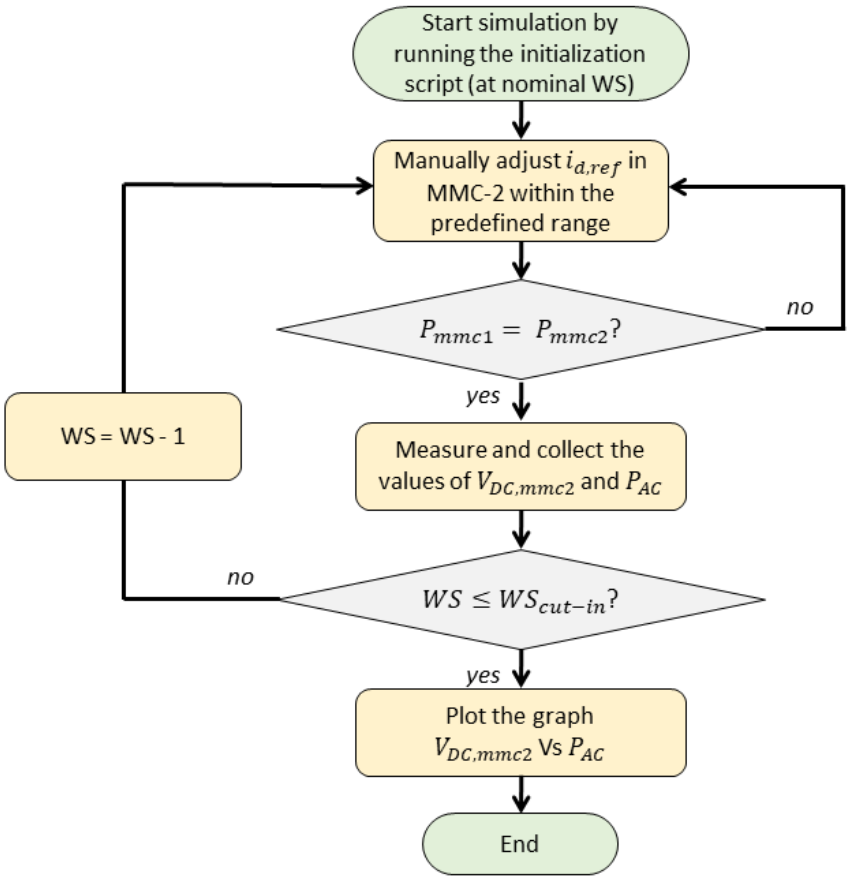

Figure 4.11: Flowchart of the generation process for the P-V graph used in the V_{DC} control method (*WS = Wind Speed*)

4.4. Investigation of the Performance of the Two Control Strategies

In this section, the performance of the I_{DC} and V_{DC} control strategies in terms of stability and response time are ascertained under three severe scenarios:

- **Scenario 1:** large wind speed step. With regard to offshore wind speed data, the height of the step has been chosen to represent very challenging conditions;
- **Scenario 2:** unloading and reloading of MMC-1. This scenario represent an extreme case of power sharing variation control order;
- **Scenario 3:** three-phase fault on one of the HVAC links. This is the most severe AC fault which can happen.

The results for each scenario are presented in the following sections.

4.4.1. Wind Speed Variation

In this scenario, the wind speed is varied as a step function from 10 to 15 m/s (cf. 4.12(a)), while the power sharing between the two MMCs is maintained in balanced conditions. A filter with time constant 0.5 s is used to avoid the discontinuity of the wind speed step while preserving the extreme character of the variation.

The graphs of the different measurements done during this scenario are gathered in figure 4.12. It can be seen that the two different control modes, namely I_{DC} and V_{DC} controls, are both leading to the same expected steady-state. The observed behaviour is very satisfactory: the DC current and voltage increase gently while remaining stable (4.12(c)(d)). The active power in each MMC also increases, but an overshot can be seen in figure 4.12(g)(h). This overshoot is caused by the sudden wind speed increase, which creates a saturation in the pitch controller of the wind generators. The saturation stems from the rate limiter present in the pitch controller, representing the mechanical limitation of the pitch limiter. What should be understood is that the overshoot is not due to the controller implemented in MMC-2 and studied here.

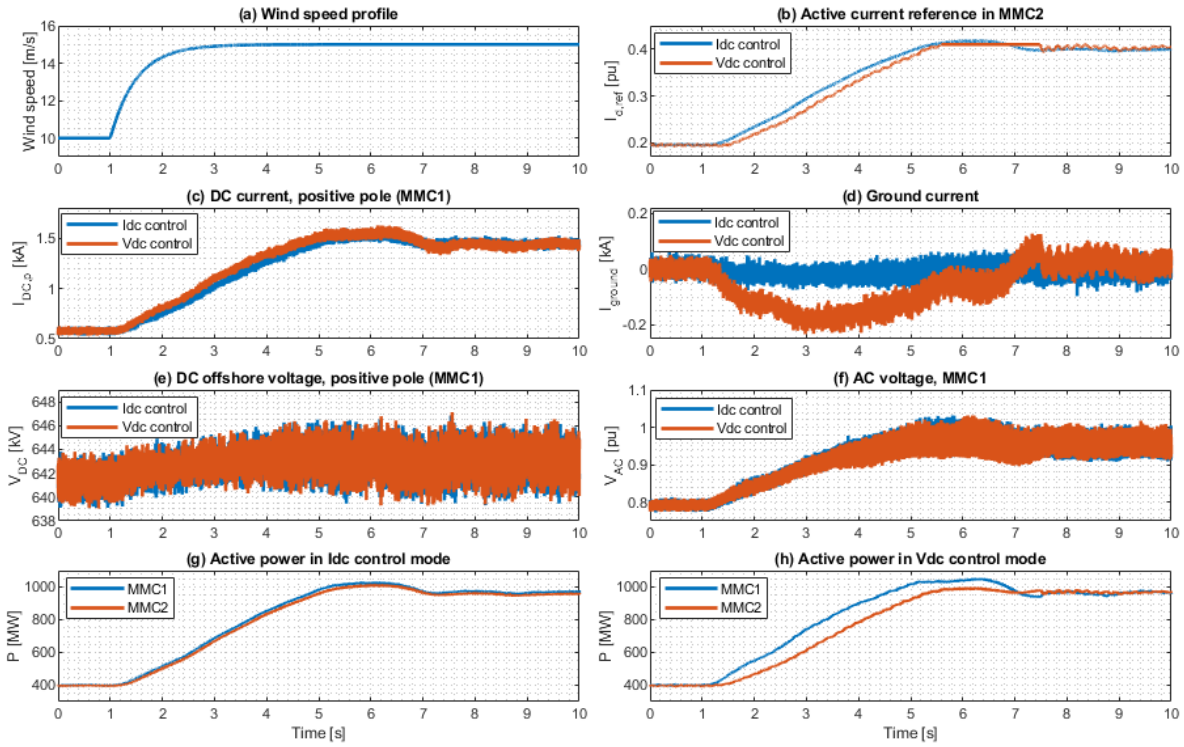

Figure 4.12: MMCs time responses when operating under I_{DC} and V_{DC} control strategies, under a wind speed step from 10 to 15 m/s

Furthermore, it can be noticed that the power sharing is kept in balanced conditions more accurately with

I_{DC} control: the graph of the ground current (4.12(d)) shows more deviation in the case of V_{DC} control mode. Finally, the AC voltage at the common bus (4.12(f)) is increasing from 0.8 to 0.95 pu. Ideally, this voltage should remain constant at 1 pu. The fact that a low AC voltage is observed at low wind speed is independent from the HVDC link control strategy (the same drop was observed while the outer loop of MMC-2 was disabled), and could be improved thanks to a reactive power ($i_{q,ref}$) control loop. Indeed, equation 4.4 shows that the reactive current can be used to control the reactive power consumption of MMC-2. MMC-2 could therefore be controlled to provide some reactive power support to the common bus in case of voltage drop. This is however outside the scope of this study, therefore the reactive power reference was kept fixed at 0 in this work.

4.4.2. Active Power Sharing and Unloading of One Pole

As explained in section 4.2.1, being able to control the power sharing between MMC-1 and MMC-2 can be very useful, when doing maintenance on one pole for example.

Unloading of MMC-1

In this scenario, the wind speed is maintained constant at 10.5 m/s. This value has been chosen because it yields an amount of power equal to half the rated capacity of the system. Hence, the power can be shared as wanted between the two MMCs. Here, the power is initially equally shared between MMC-1 and MMC-2. At 0.5 s, the system is ordered to transfer the total power through MMC-2, therefore unloading MMC-1. The results are shown in figure 4.13: on the left column, the power sharing set-point has been given in the Runtime file as a step function (4.13(S-a)), in order to represent an extreme operation. On the right columns, the set-point has been given as a ramp function (4.13(R-a)), to check if a less extreme operation would improve the results. The results for I_{DC} control are presented in blue, while those for V_{DC} control are presented in red.

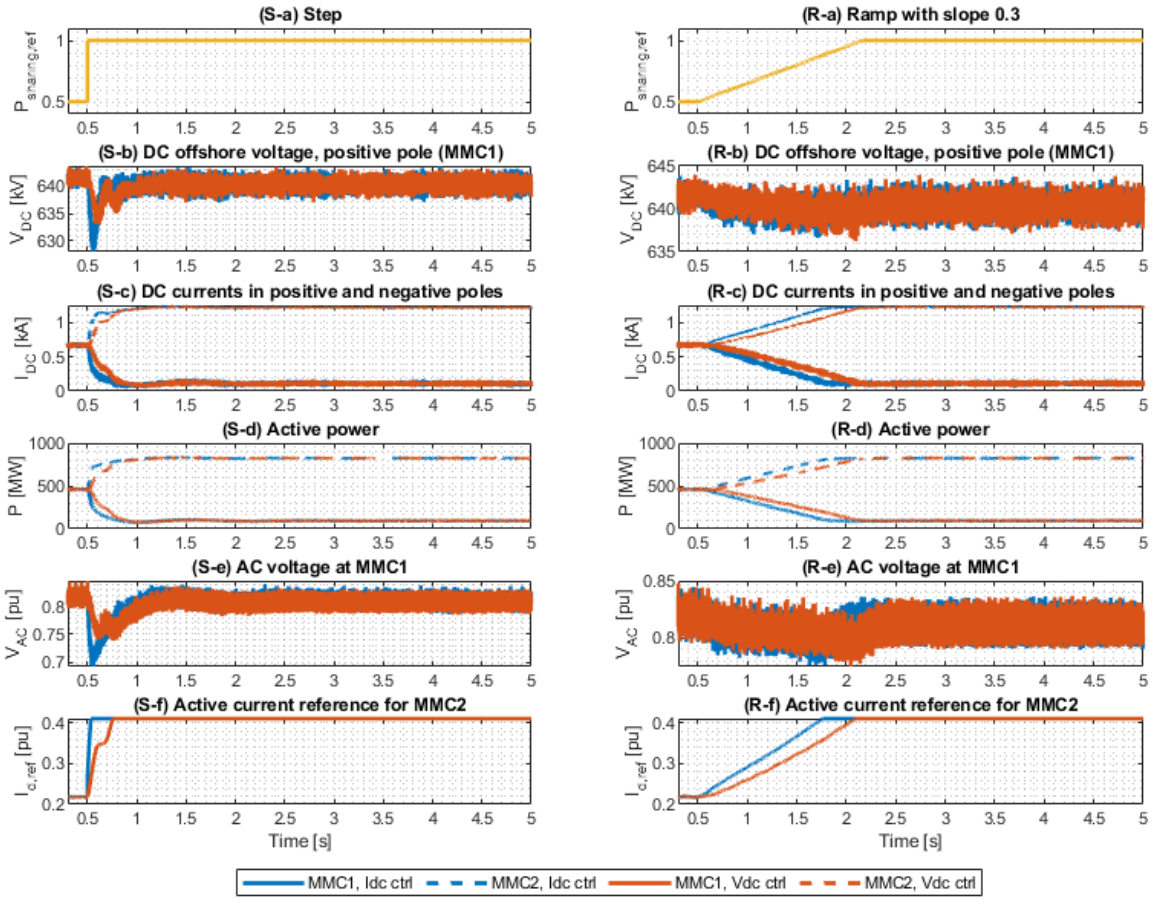

Figure 4.13: MMCs time responses when operating under I_{DC} and V_{DC} control of MMC-2, under unloading of MMC-1, at constant wind speed of 10.5 m/s

Three main observations can be made from these graphs:

- MMC-1 cannot be completely unloaded and remains energised (4.13(S-d)(R-d));
- If the set-point is given as a step function, a voltage drop (both AC and DC) is observed (4.13(S-b)(S-e)), while this drop can be avoided by adjusting the input set-points, using a ramp function (4.13(R-b)(R-e)). We can deduce that discontinuities in the input set-points are not handled properly by the controller and the system;
- Although the two types of control strategies seem to perform very well and almost similarly, the I_{DC} control is slightly faster than the V_{DC} control (4.13(S-f)(R-f)). A broader performance comparison, including optimal tuning of the two options shall be addressed in a future research work.

Re-loading of MMC-1

Starting from the previous scenario, the reverse operation is applied, to bring the system back to an equal sharing of the power between the two MMCs.

The results can be seen in figure 4.14. In this case, a clear difference between the two types of controls can be seen: the V_{DC} control (red lines) leads to large oscillations at a frequency of 5.6 Hz, whereas stable signals are maintained with the I_{DC} control (blue lines). Even if the same steady-state is reached after about 10 seconds, the signals are already settled in less that 1 second in the case of a step set-point with I_{DC} control. The high voltage sensitivity of the link is therefore put forward.

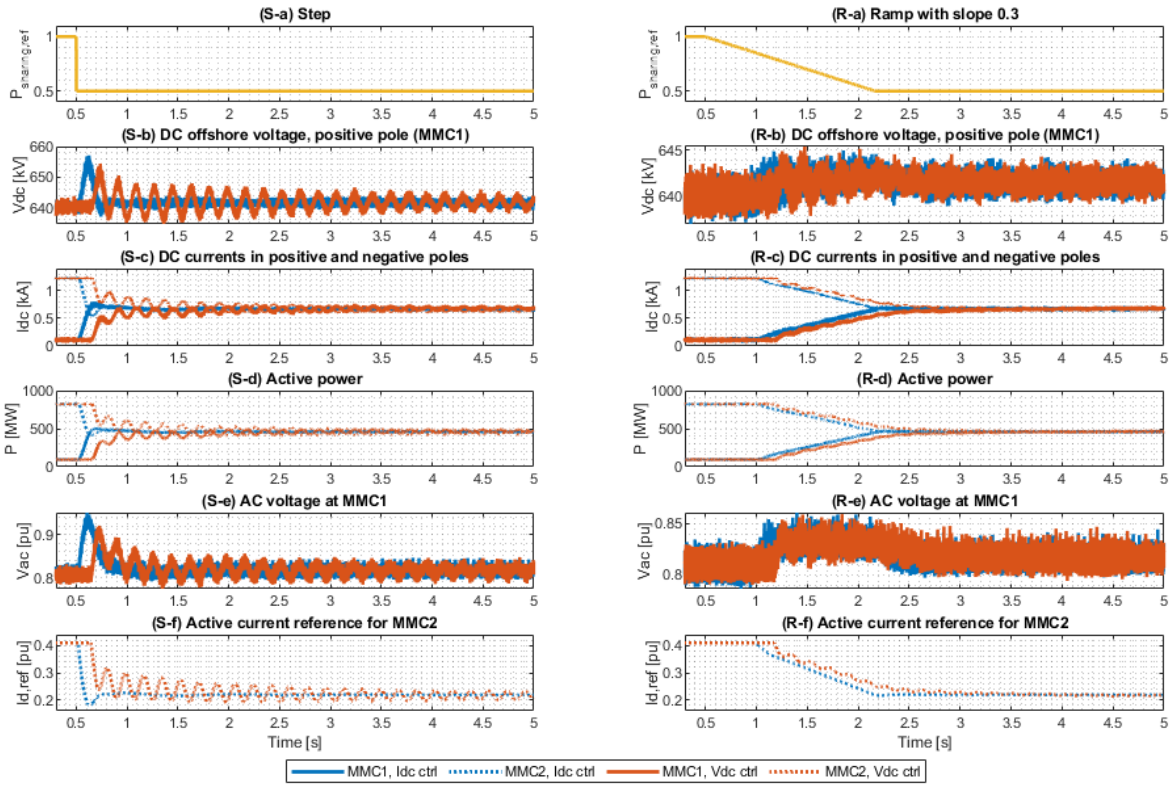

Figure 4.14: MMCs time responses when operating under I_{DC} and V_{DC} control of MMC-2, under re-loading of MMC-1, at constant wind speed of 10.5 m/s

Trajectories

In order to have a better understanding of what happens in the last scenario (re-loading of MMC-1), it is interesting to plot the trajectory followed by the converter. This trajectory is plotted in a phase plot with variables P and V_{DC}, as can be seen in figure 4.15. The green arrows indicate the direction in which the trajectories are evolving over time.

It can be seen on the graphs that the trajectory in the case of I_{DC} control (4.15(a)(c)) is much smoother than in the case of V_{DC} control (4.15(b)(d)), which means that it reaches the equilibrium faster and with smaller chattering. This indicates that in the first case, the converter steady-state operation is reached in a more straight-forward manner.
Additionally, one might think that even in the case of I_{DC} control, the trajectory, which has the shape of a bell, could be flattened to a line between the initial and final states, to achieve a faster response of the system to the control set-points. This could be done by implementing a control strategy which would provide more accurate set-points, for example a strategy inspired from the Droop Line Tracking method developed in [53].

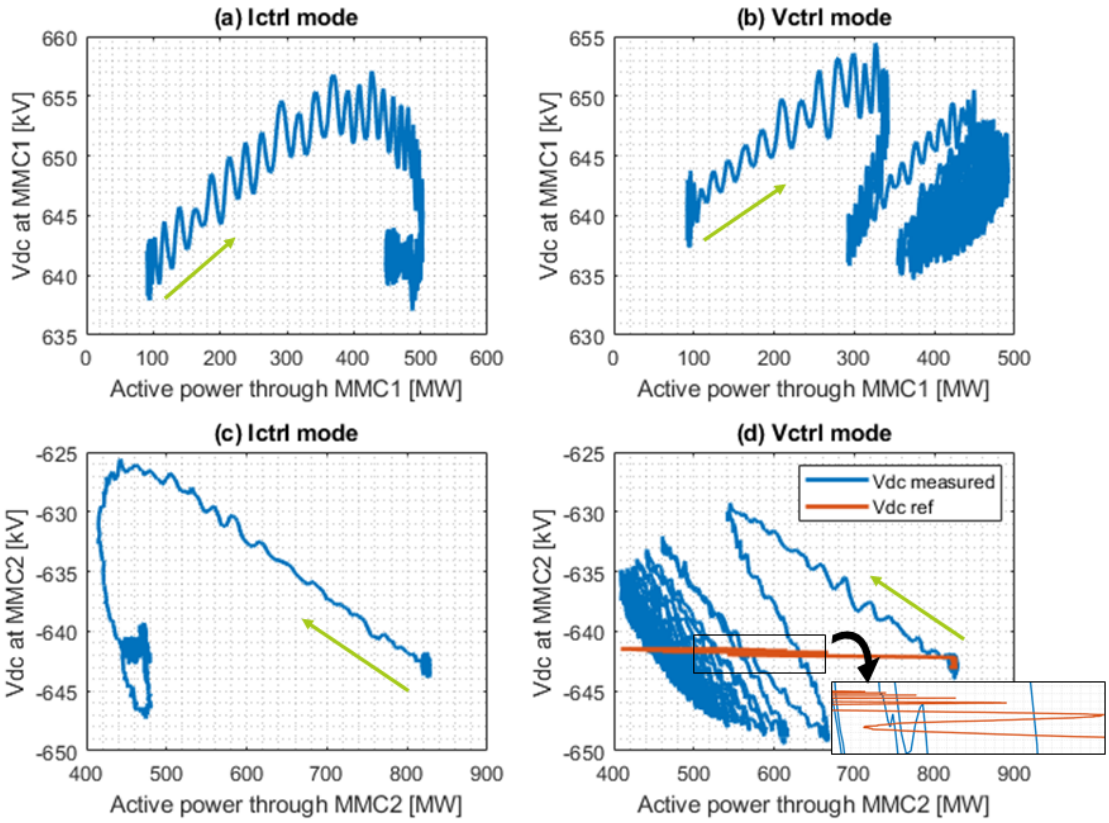

Figure 4.15: P Vs V_{DC} trajectory when re-loading MMC-1 with a step set-point. The green arrows indicate the evolution of the trajectory in time

4.4.3. HVAC Fault

In this scenario, a permanent three-phase-to-ground fault is triggered on the HVAC link connecting wind turbine 1 to the hub, as shown in figure 4.16. An AC circuit breaker is placed on the HVAC line 1, between the fault location and the common bus. This circuit breaker is the only one which is activated, but no reclosing scheme was activated for this simulation. The circuit breakers present on the other HVAC lines have been de-activated, because they were otherwise all triggered by the fault on HVAC-1. It would be possible to implement a control scheme to prevent the circuit breakers 2 to 4 from opening in case of fault on HVAC-1 (by identifying the location of the fault for example), but this was outside the scope of this thesis.
The wind speed is maintained constant at 16 m/s during the simulation. The results are presented in the figure below. As can be seen in figure 4.17(a), the fault is triggered at 1.5 s, and the breaker on HVDC-1 opens 100 ms afterwards.

It is observed that in the case of I_{DC} control, the system recovers quickly from the fault, while in the case of V_{DC}, the oscillatory behaviour is more severely excited (with frequency 5.8 Hz) and no steady-state is reached (4.17(d)). It can be concluded that the voltage control is more sensitive and less robust than the current control in case of fault on the AC side.

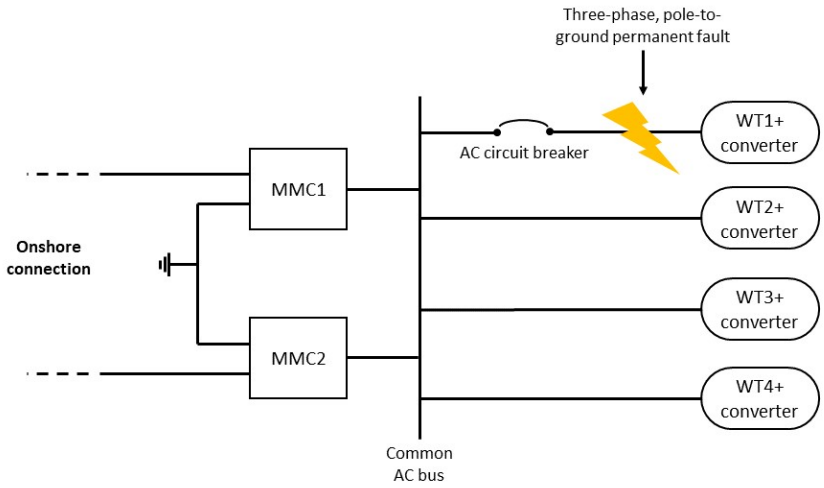

Figure 4.16: Location of the applied fault on HVAC-1

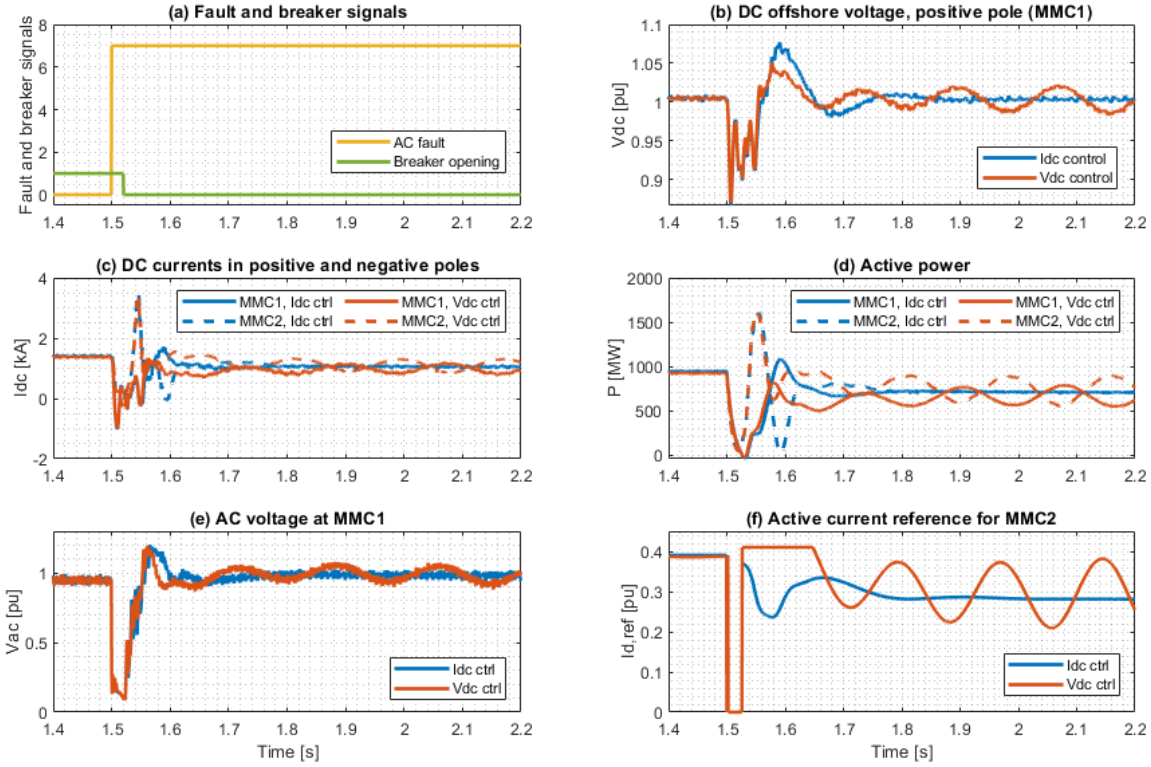

Figure 4.17: MMCs time response under three-phase fault on HVAC cable 1, at constant wind speed of 16 m/s

4.4.4. Conclusion

From the research made in this chapter, it can be concluded that I_{DC} control and V_{DC} control are two control strategies which are worth investigating for the power sharing capabilities of MMC-2. Using DC signals to control the converter was found to generate better results than using direct AC power control, since DC signals are not affected by the perturbation of the AC hub. Hence perturbations from the AC side are not passed on to the control set-points, resulting in a more stable control action.
From the first results obtained in this thesis, it seems that I_{DC} control will perform better than V_{DC} control, in

terms of response time and stability under AC fault. With the V_{DC}, the oscillatory behaviour of the system was more excited than with the I_{DC} control. However, further investigation will be necessary to validate this statement. The PI controllers present in the control structure should first be optimal tuned by using an adequate method. Once this is done, simulating the behaviour of the system under a DC fault (for example a fault-to-ground fault on one pole of the HVDC link) would give more insight on the potentialities and weaknesses of both control strategies.

5

Conclusion

In the first part of this chapter, the main findings of this thesis work are summarized and concise answers to the research questions listed in chapter 1 are provided. In the second part, some ideas for future work which could be carried out in extension of the scope of this thesis are listed.

5.1. Summary of Findings

This thesis focuses on the the challenge of developing power management strategies for offshore renewable energy hubs. Because offshore hubs are zero-inertia networks, EMT simulations are necessary to capture the fast dynamics of the system. The 2 GW EMT model of an offshore wind energy hub developed in [20] is taken as a starting point, an upgraded with respect to two main points of focus. In a first part, electrolysers are integrated into the hub and placed at different locations, in order to identify the potentials and difficulties related to each type of connection. In a second part, the HVDC link, which connects the offshore hub to the shore, is given attention. The monopolar topology found in the initial model ([20]) is changed into a bipolar topology, and power sharing strategies between the two MMCs constituting the offshore terminal of the link are investigated.

Several techno-economic studies, among which the one presented in [13], claim that performing water electrolysis offshore would be beneficial from an economical point of view. Recent studies also found that large scale electrolysers would be suitable for providing ancillary services to the network [10]. However, there is a lack of studies presenting EMT-simulation based stability analysis of offshore-connected electrolysers. In this work, electrolysers were connected to the hub model at two different locations: on the AC common bus of the hub, and on the DC link of the back-to-back converter of the WTs. It was found that the two locations can be beneficial in different aspects. An effective mitigation of sudden active power imbalance can be achieved by placing the electrolyser locally at each wind turbine, or centrally at the common bus of the hub. In case of fault within the hub, e.g. a three phase short circuit near a wind turbine, the connection of an electrolyser to the DC link of the wind turbines (through a buck converter) is convenient to prevent loss of wind power generation due to the islanding of the turbine.

From the literature, it can be understood that a bipolar topology is more advantageous (regarding reliability and flexibility) than a monopolar topology for the HVDC connection. Indeed, in case of failure of one converter or cable, half of the nominal capacity of the link can still be transferred. Aside from fault events, being able to decide of the power sharing between the two offshore MMCs would be useful to un-load one of the poles in case of planned maintenance for example. In order to do so, an outer loop was added in the controller of one of the offshore MMCs, which output is an active current reference given as input to the inner loop. The signals used to generate the current reference in the outer loop are DC signals, either current or voltage. Both options generated promising results, and further research work should be carried out to deeply investigate the robustness of this power sharing strategy.

5.2. Answers to the Research Questions

Concise answers to the research questions framing this thesis are provided below.

- **What are the major numerical issues which should be solved when connecting electrolysers at different locations of the hub to ensure a detailed and trustworthy simulation of the developed model, and how to solve them?**
  When connecting electrolysers and their converters to the hub model, large unrealistic losses were observed in the buck converter. It appeared that those artificial losses stem from the switch model used in the RSCAD software in the small time-step environment. Lowering the switching frequency of the converter (in the case of connection to the DC link of the WTs) or using a substep model (in the case of connection to the AC common bus of the hub) helped to reduce those losses. RSCAD is currently developing a new converter model, with an improved firing pulse generator, which could be relevant to use for this simulation [44].
  Additionally, when connecting an electrolyser to the AC common bus of the hub, oscillations appeared in the hub, due to a resonance phenomenon. Using a RC damper in the transformer connecting the electrolyser enabled to avoid those oscillations.

- **How can electrolysers contribute to manage challenging real-life conditions (e.g. three-phase faults or highly-fluctuating wind profiles), and what are their benefits according to the location where they are connected?**
  Electrolysers are loads which can achieve effective mitigation of sudden active power imbalance in the hub. When an adequate control scheme is implemented, they can help to mitigate the power fluctuations due to wind speed variations, and potentially allow for a downsizing (by the size of the electrolyser system) of the links connecting the hub to the shore.
  Some other benefits are specific to the location of the connection. In case an electrolyser is connected to the DC link of a WT, if this turbine is islanded because of a fault on its HVAC cable, the electrolyser can prevent the loss of the generated power due to dissipation by the DC link chopper. An electrolyser centrally connected to the AC common bus of the hub could be used for example to provide ancillary services (e.g. frequency reserve, reactive power support) to the hub.

- **What are the major drawbacks of a monopolar HVDC link between the offshore hub and the shore, and how to modify it to allow for reliable and flexible power exchange in the future?**
  The major drawback of a monopolar link is its lack of reliability. Indeed, in case of failure of one converter or cable, no power can be transmitted anymore. On the contrary, a bipolar link can still transmit half of its nominal capacity in case of failure of one converter or cable. Another drawback of the monopolar link is that it allows for less transfer capacity for the same amount of cables as a bipolar link. Therefore, we advise to use a bipolar to connect the offshore hub. Nevertheless, the power sharing strategy is one of the key factors that should be studied to exploit to the best the potential of the bipolar topology of the link.

- **What is a conceptually simple and effective strategy to implement power sharing capabilities among the offshore converters?**
  In order to implement power sharing capabilities among the offshore converters, we recommend to use DC-side signals rather than AC side signals. For example the DC current or DC voltage of the HVDC link could be used, but it was observed that the power sharing based on measured DC current is faster, effective, and less prone to cause collateral effects (such as undesirable oscillations of DC voltage and current). Measurements are given as inputs to the outer loop of the grid-following offshore MMC. The output of the outer loop is a direct current reference for the inner loop of the converter. Thanks to this control, the power absorbed by the converter can be monitored. The rest of the power produced by the WTs will flow through the other offshore MMC.

5.3. Future Work

After finalizing this thesis, the author is providing recommendations for future work which could be carried out, using the model developed in the present work as a baseline.

- Optimal initialisation procedure of the dynamic model for hybrid offshore hubs, which is needed to work on possible numerical issues in other studies e.g. focused on energisation and black-start [23];

- Optimal usage of the multi-core capabilities of the RTDS to enable the integration of different parts of the detailed EMT models in a computationally efficient and error-free simulation;
- Investigation of onshore disturbances by using a more detailed representation of the onshore electrical power system;
- Implementation of a reactive power control strategy in the outer loop of MMC-2 to prevent the possible voltage drop at the common bus in case of decreasing wind speed;
- Integration of advanced functionalities (e.g. communication with TSO, reactive power support in case of fault, grid forming capabilities) similar to the ones developed in [12] to the electrolyser model;
- Extension of the present EMT model to an MTDC network. In that case, for the coordination of the controllers, the method proposed in [53] could be used. For the interconnection between various HVDC links with different line topologies, the DC-MMC proposed in [54] could be used.

Appendices

A

Guidelines to Initialise and Run the Simulation Files

A.1. Simulation Folders and Files

There are three simulation folders, which can be seen in figure A.1:

- The folder **WT4_MMC2_RSCAD_Ely_DClink** contains the hub model with a monopolar HVDC link and electrolysers connected to the DC link of the wind turbines, studied in section 3.2;
- The folder **WT4_MMC2_RSCAD_Ely_ACbus_substep** contains the hub model with a monopolar HVDC link and an electrolyser connected to the AC common bus of the hub, studied in section 3.3;
- The folder **WT4_MMC2_RSCAD_Bipolar** contains the hub model with a bipolar HVDC link and two onshore MMCs, studied in chapter 4.

Each folder contains 10 files:

- A .dft file: the draft file containing the model;
- A .sib file: the Runtime file, containing the simulation dashboard and in which the results can be observed;
- A .scr file: the initialisation script;
- Three files 66kV.tli, 66kV.tlo and 66kV.tlx used to model the AC cables in the model;
- Three files DC200Cfd.cli, DC200Cfd.clo and DC200Cfd_out used to model the DC cables in the model;
- A file Three_WindProf containing the wind speed data to run the model with one of the wind speed profiles, as explained in section A.3.

It is explained in section A.2 how those files should be used.

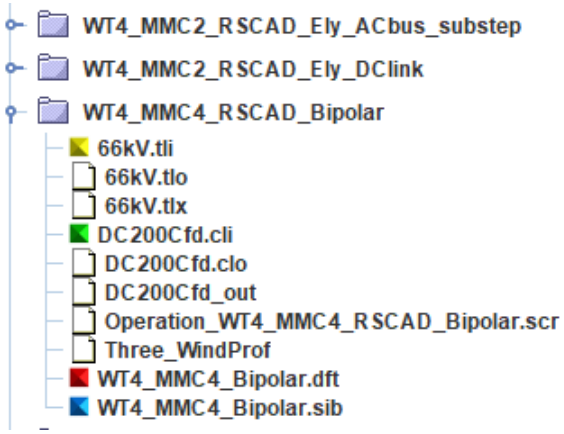

Figure A.1: The three simulation folders

A.2. Basic Simulation

In order to run the simulation properly, the following steps, which are also summarised in figure A.7, should be followed. The guidelines are specific to the TU Delft Electrical Sustainable Power (ESP) laboratory hardware, but can be adapted with minor changes to RTDS hardware located in other laboratories. It is assumed that the RSCAD software is already installed on the computer of the user.

- **1° Connect to the Virtual Private Network (VPN)**
  If connecting to the RTDS hardware remotely, use the OpenVPN Connect software to connect to the TU Delft ESP lab VPN, as shown in figure A.2.

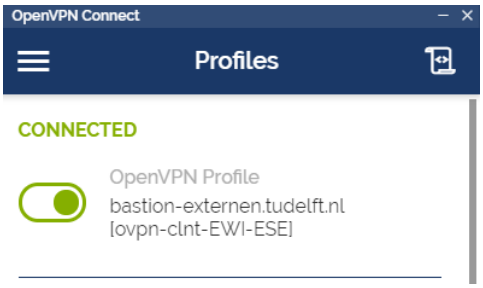

Figure A.2: Connection to the TU Delft ESP lab VPN

- **2° Copy the simulation folder**
  Unzip (if necessary) the simulation folder, and copy-paste it in the folder *RSCAD* > *RTDS_USER* > *fileman* in your computer.
- **3° Open the RSCAD software**
  Double-click on the RSCAD software icon (cf figure A.3) to open the software.

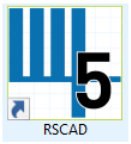

Figure A.3: RSCAD software icon

- **4° Open the simulation files**
  Open the simulation model file (.dft) and Runtime file (.sib) by double-clicking them.

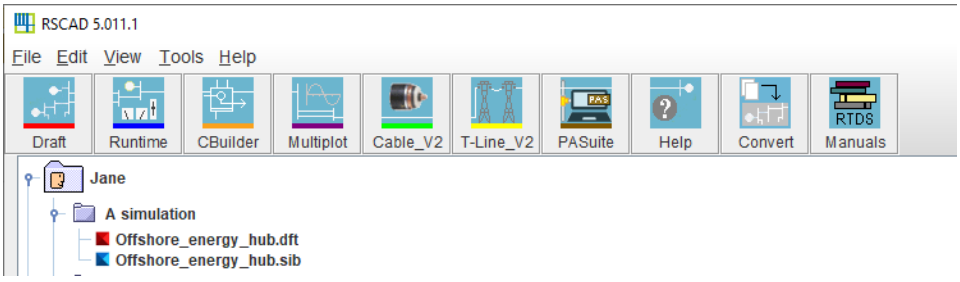

Figure A.4: RSCAD software window

- **5° Compile the draft file**
  In the draft (.dft) file, enter the number of the first rack to be used to run the simulation. Make sure the rack has a NovaCor processor, and that the two next racks also have NovaCor. RSCAD will automatically use the next racks consecutive to the one you entered.
  Compile the draft file by clicking on the icon indicated in figure A.5.

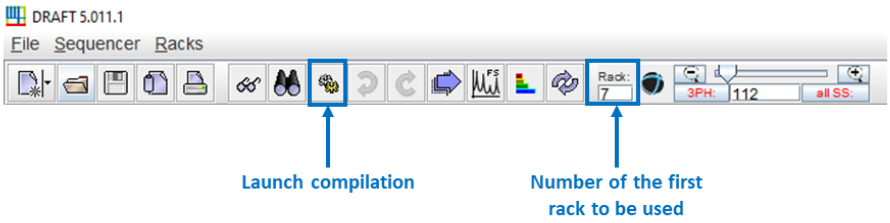

Figure A.5: Draft (.dft) file tool bar

- **6° Run the initialisation script**
  In the tool bar of the Runtime (.sib) file, click *Script* > *Open*, select the file *Operation_WT4_MMC2.scr*, click *Choose scr File* and click the play icon, as indicated in figure A.6.

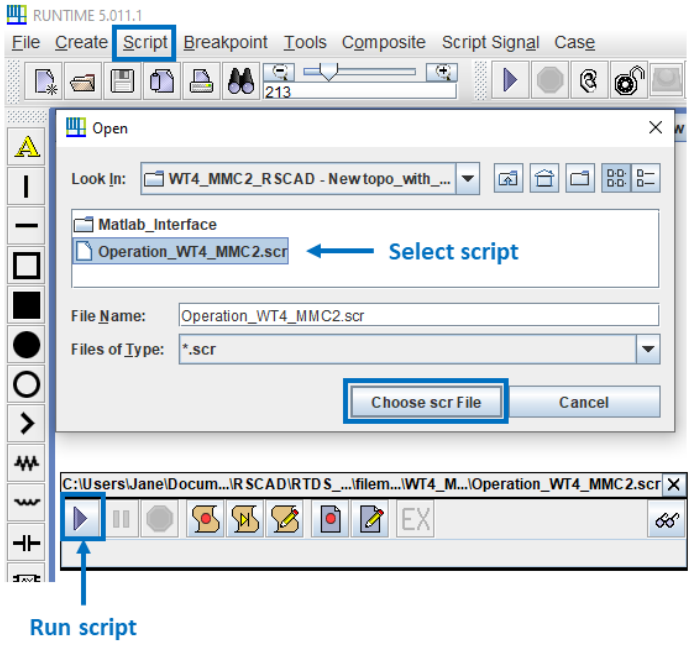

Figure A.6: Running the initialisation script in the Runtime (.sib) file

After step 6, the simulation is running. Values of the dials, switches and sliders can be edited in the Runtime (.sib) file and the plots of interest can be saved. As indicated in figure A.7, if a draft variable needs to be modified, the simulation needs to be stopped first.

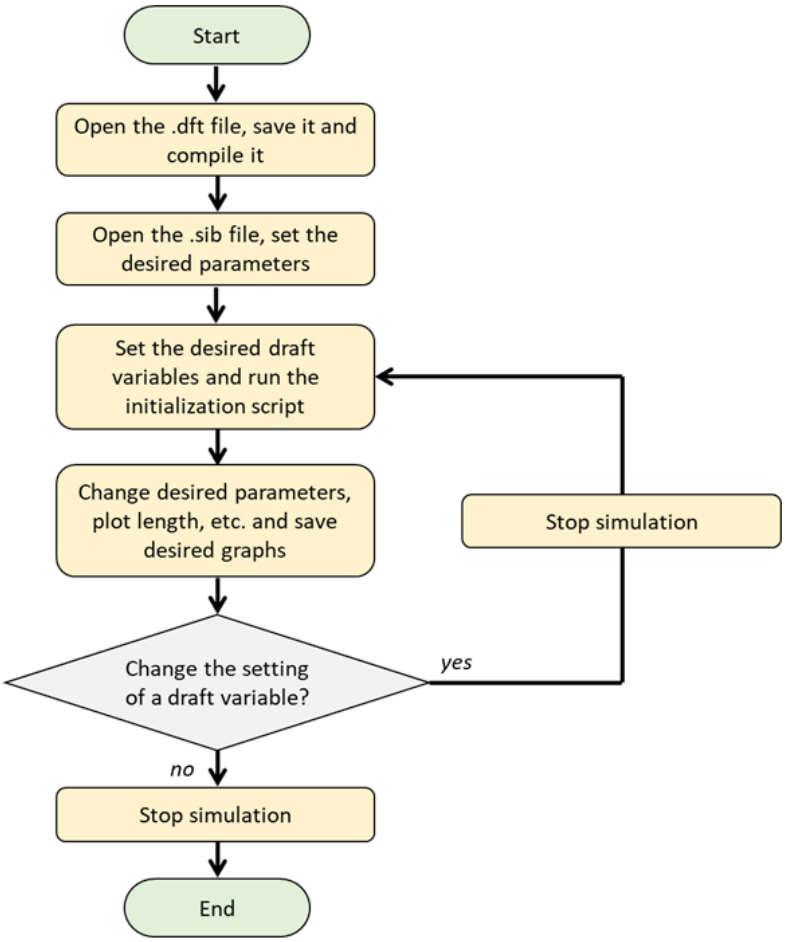

Figure A.7: Process to follow to run the simulation in RSCAD

A.3. Simulation With Wind Speed Profile

In order to run the simulation with one of the predefined wind profiles (see appendix D), a few additional steps should be followed.

- Follow steps 1° to 4° previously described.
- **A° Select the wind speed profile** In "subsystem 2: Wind Turbines" of the draft (.dft) file, double-click on the scheduler component to open the property window, as shown in figure A.8. In the tab *FILE DATA SCHEDULE* select the number of the wind profile to be used and click *Update*. The description of the wind profiles can be seen next to the scheduler component. Note the value of the initial wind speed corresponding to the wind profile of interest.

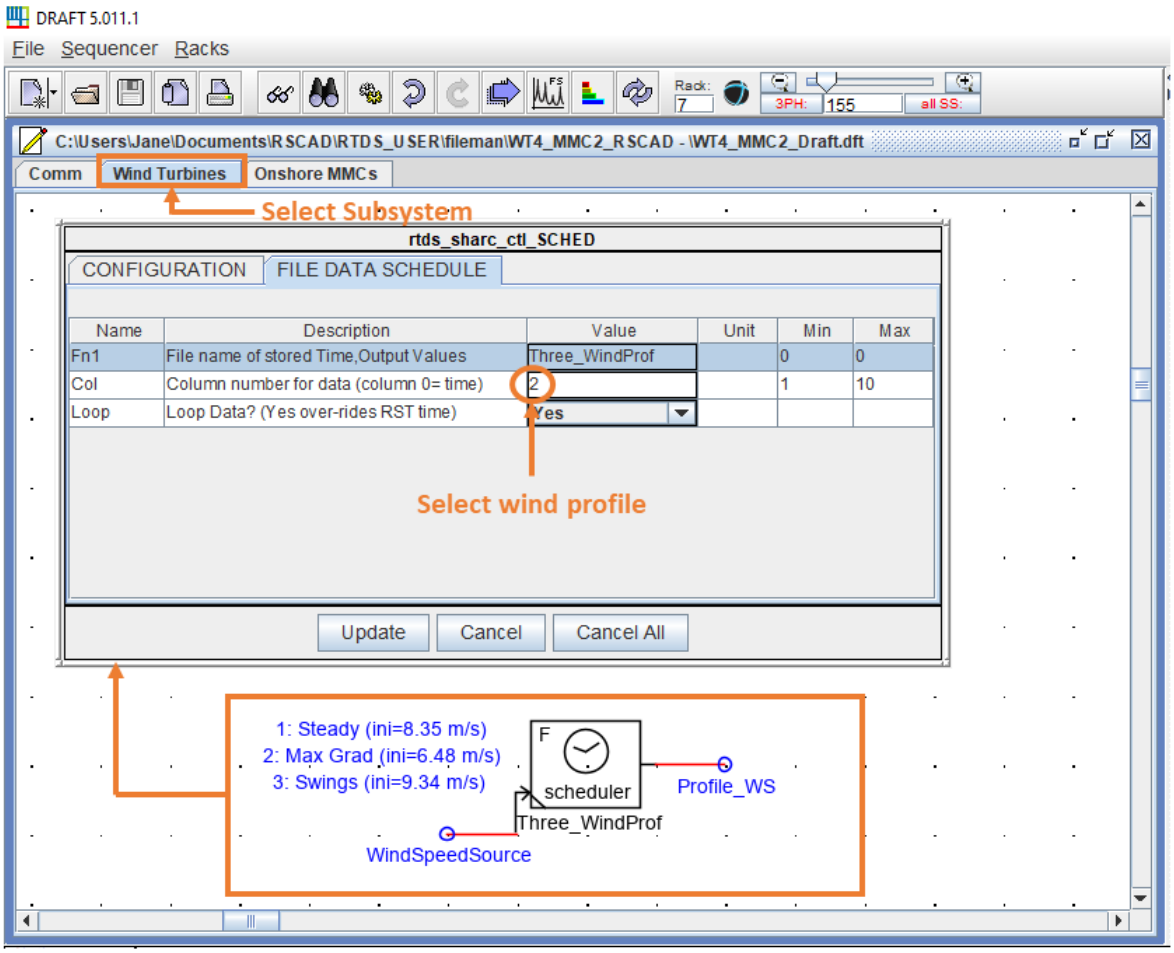

Figure A.8: Selection of the wind profile in the draft (.dft) file

- Follow steps 5° to 6° previously described.
- **B° Set the plotting length** In the tool bar of the Runtime (.sib) file, select *Case* > *Option* and set the finish time to 30 seconds. Click *OK*.

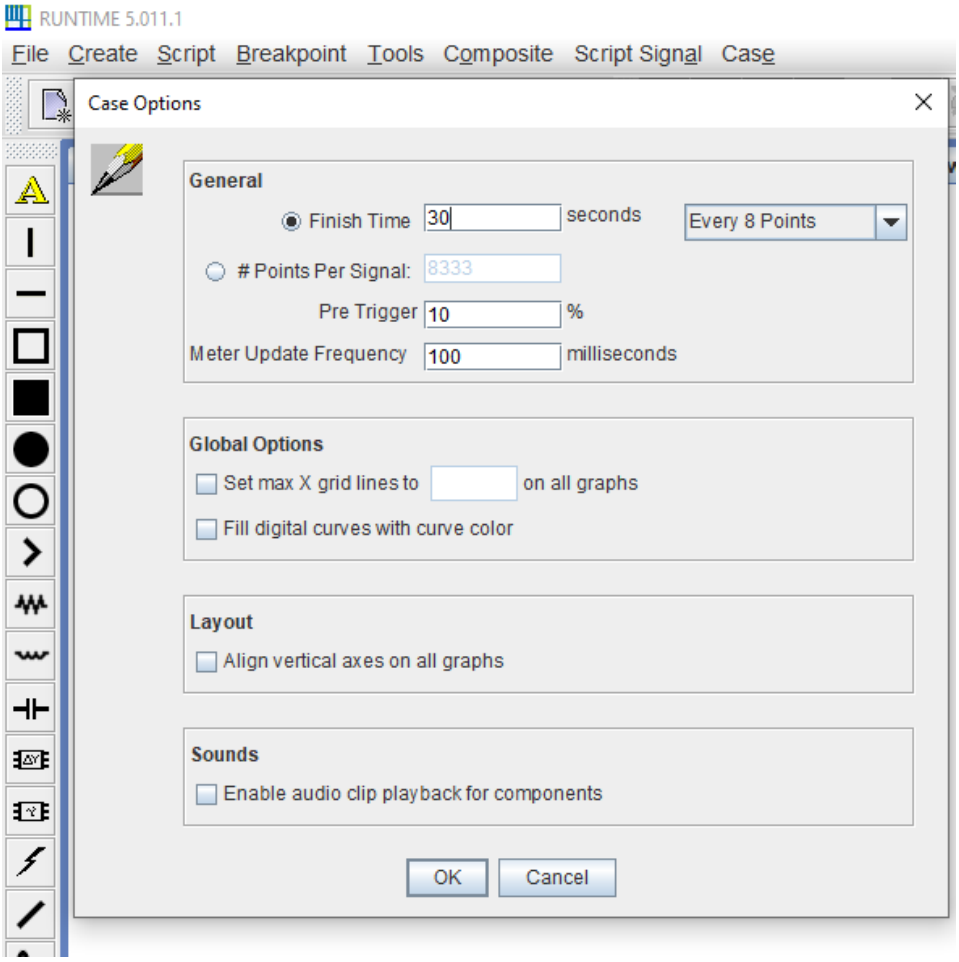

Figure A.9: Modification of the plotting time in the Runtime (.sib) file in RSCAD

- **C° Start the reading of the wind profile data** In the Runtime (.sib) file, set the wind speed (slider *Hub_WS*) to the initial wind speed noted in step A°, and change the switch *Hub_wind* from the position "Manual (1)" to "Profile (0)" by clicking on it.
  Tip: in order to start the plot at the beginning of the wind profile, the switch *Hub_wind* should be clicked when the meter *Time* displays a multiple of 30.

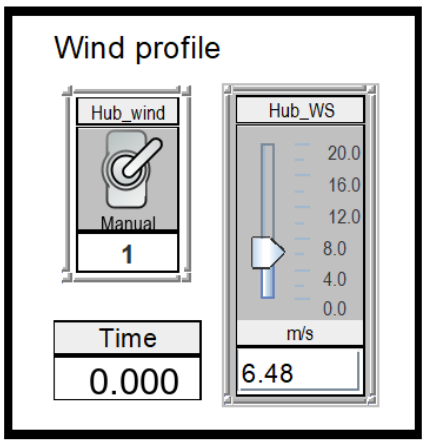

Figure A.10: Starting the reading of the wind profile data in the Runtime (.sib) file in RSCAD

B

PWM in RSCAD

Sinusoidal PWM is the method used in RSCAD to control the switches in the different converters. The converter controller generates a modulation signal (in blue in figure B.1) which is compared to a triangular wave (in orange in figure B.1), produced by a triangular wave generator.

In figure B.1, the example of a one-leg system is considered. The two signals mentioned above are compared by the firing pulse generator. The first switch will be turned off as soon as the value of the triangular wave rises above the value of the modulation signal. When the value of the triangular signal falls below the value of the modulation signal, the first switch will be turned on. The second switch will be control in a complimentary way. The voltage output of the system will be similar to the square signal shown on the figure. Similarly, two other modulation signals can be added to the firing pulse generator to generate the signals for the two other legs of a three-leg converter [42]

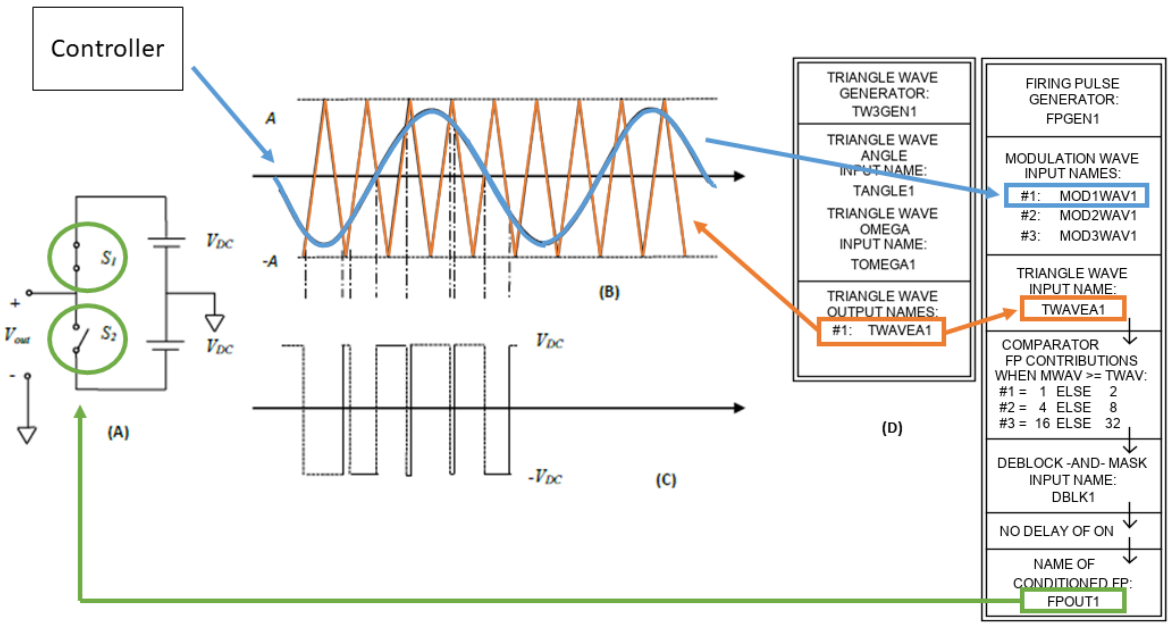

Figure B.1: PWM in RSCAD - (A) Two-switch system (B) Triangular and modulation waves (C) Output voltage (D) Triangular wave and firing pulse generators in RSCAD .dft file (adapted from [42])

C

Anti-Windup Mechanism

Integrator windup is a common problem which may arise when using a PI controller with a limiter at the output. The problem is that the integrator keeps integrating the error, even though the output is saturated. This can result in oscillations, long settling time and/or long rise time [55].

Several anti-windup techniques have been developed, such as back-calculation and conditional integration. In this thesis, only the back-calculation method is used. This technique consists in subtracting to the integrator input the "surplus" of the integrator output. Here the "surplus" refers to the difference between the integrator output signal and the output signal after the the limiter. A proportional coefficient (K) can be added to the anti-windup loop if necessary. The principle of this method is illustrated in figure C.1.

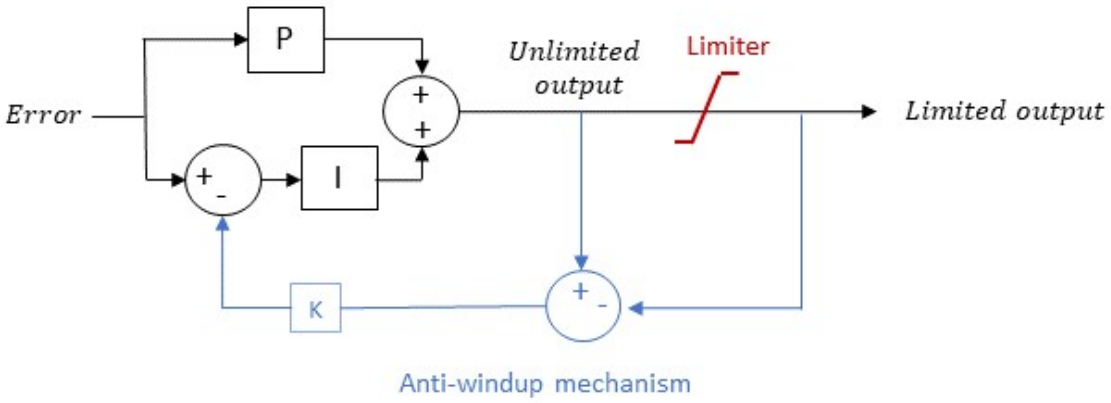

Figure C.1: PI controller with limited output and back-calculation anti-windup mechanism

D

Generation of Reference Wind Speed Profiles

In order to observe and assess the behaviour of the network under real wind conditions, three sample scenarios have been created, based on real wind speed profile. The data have been acquired from for the location 51.95926N 2.94236E shown in figure D.1. Each scenario provides a sample wind speed time series in m/s with a time step of $1 sec$. The three scenarios are described in table D.1.
The second scenario has been selected using a Matlab script which looks for the maximum speed gradient over a time window of 10 s (called sliding gradient).

Figure D.1: Location 51.95926N 2.94236E for the wind speed data

Scenario	Name	Characteristics	Duration
1	Steady conditions	Wind speed within 5% of average speed	$30 sec$
2	Sharp increase	Maximum sliding speed gradient	$30 sec$
3	Swings	Consecutive swings	$30 sec$

Table D.1: The three selected wind speed samples

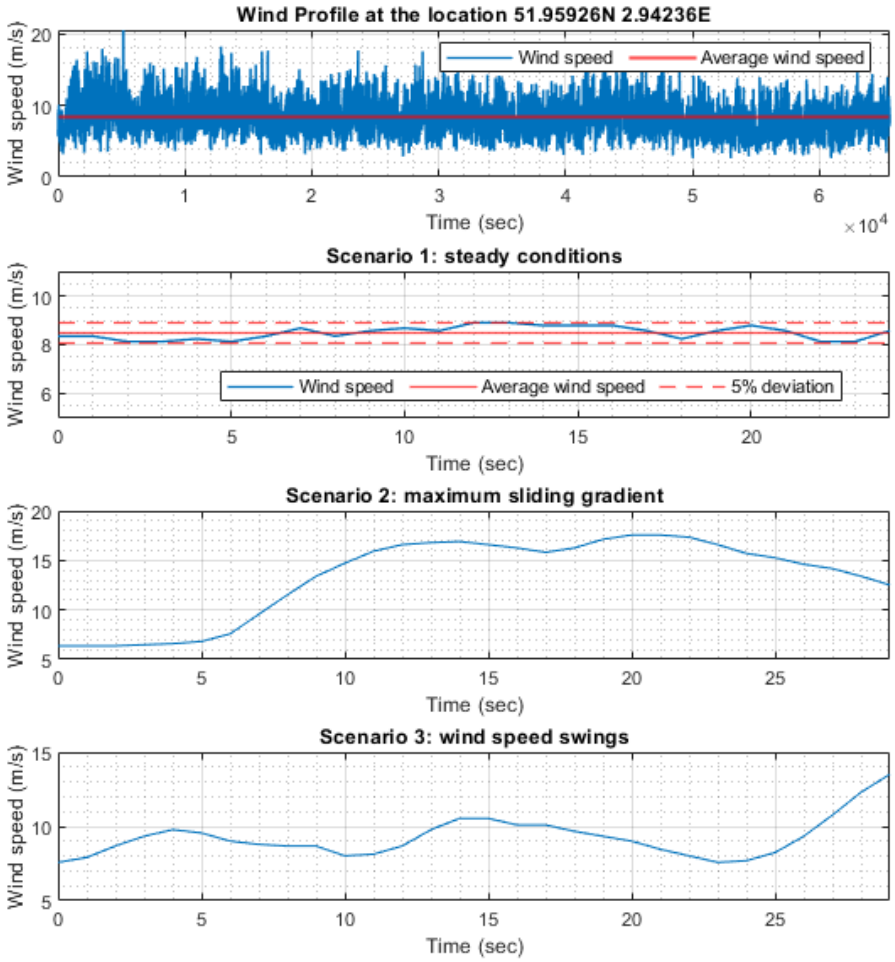

Figure D.2: Graphs of the wind speed scenarios

The wind profile values are then gathered in a file, which can be read by the scheduler component in RSCAD (cf figure D.3). More details on how to run a simulation with one of the wind profiles can be found in A.

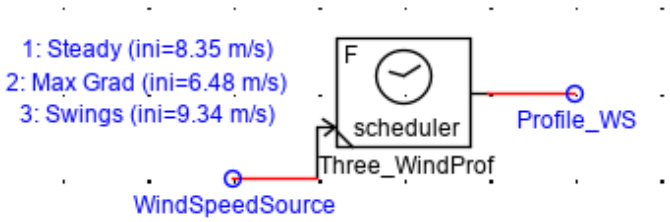

Figure D.3: Scheduler component in the draft (.dft) file in RSCAD

E

Racks, Subsystems and Core Assignment in RSCAD

E.1. Racks and Subsystems

The ESP lab at TU Delft possesses three NovaCor chassis (or rack [1]), all of them being used to run the simulation. The network has been divided into three subsystems, each of them being run on a different NovaCor chassis. Two consecutive NovaCor chassis can communicate between each other, but the consecutive subsystems in the draft files must be connected between each other via transmission lines. A summary of the distribution of the different parts of the network among subsystems and racks can be seen in figure E.1 and E.2 for the model implementing electrolysers on the DC links and an electrolyser on the AC common bus, respectively. The same summary is available for the model implementing the bipolar HVDC link and the two onshore MMCs in figure 4.4.

E.2. Core Assignment

Each chassis has several cores (four for chassis 7 and 8, seven for chassis 9), and each core can be assigned 300 load units. Each chassis can have a maximum of two cores allocated to network solution. The remaining cores are used for power system and control system components [42]. The VSC components can be assigned manually to a core, if desired. The core assignment proposed in [20] for subsystems 1 and 2 has been conserved. For subsystem 3, the core assignment is done automatically, but two cores are explicitly required by using the network solution automatic placement block in RSCAD. As an example, the final core assignment summary for the model implementing an electrolyser on the AC common bus of the hub can be seen in figure E.3.

[1] The term "rack" should be used to refer PB5 processor cards, while the term "chassis" should be used to refer to NovaCor processor. However, for convenience, all processor at the ESP lab are commonly called racks and have been attributed a number

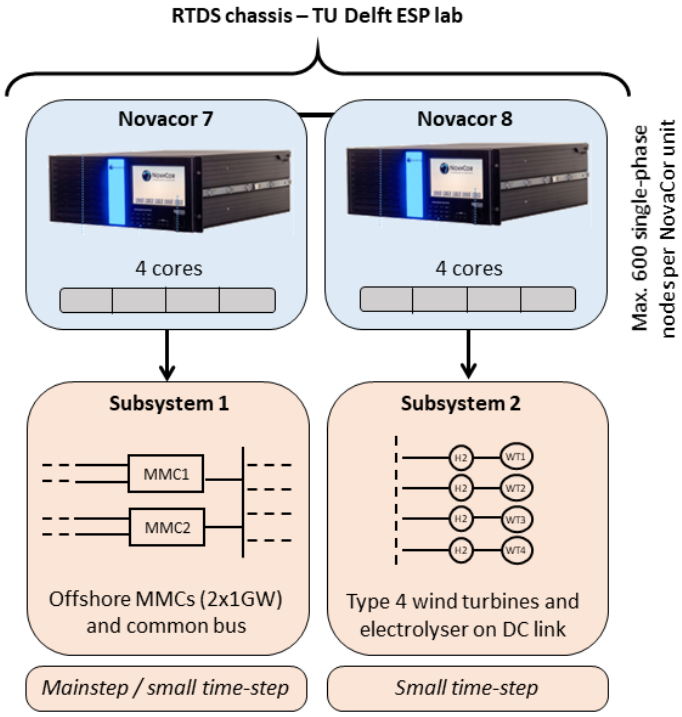

Figure E.1: RTDS racks used to run the simulation and corresponding part of the network assigned to each rack, in the model implementing electrolysers on the DC links of the WTs

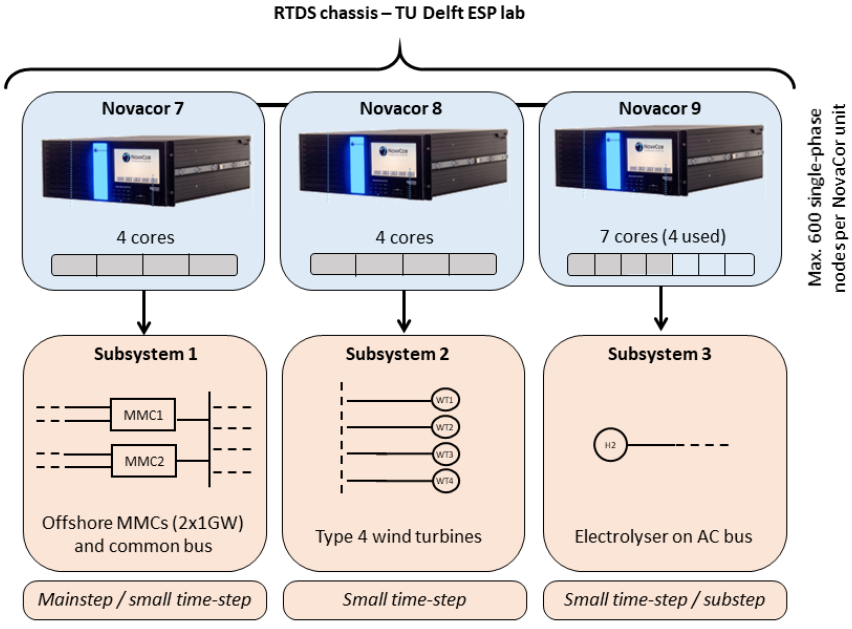

Figure E.2: RTDS racks used to run the simulation and corresponding part of the network assigned to each rack, in the model implementing an electrolyser on the AC bus of the hub

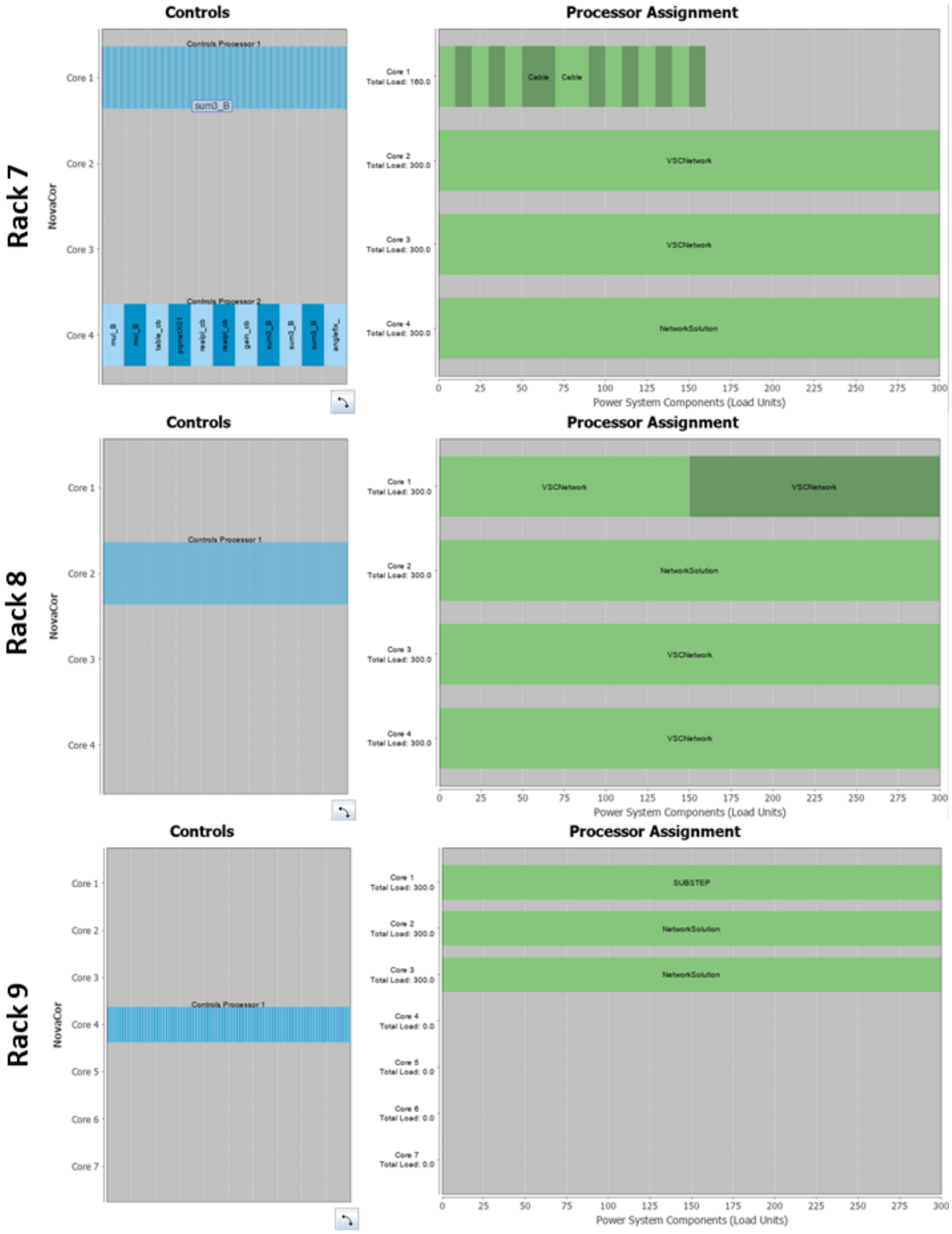

Figure E.3: Core assignment for the model implementing an electrolyser on the AC common bus of the hub

F

MSC Control Scheme

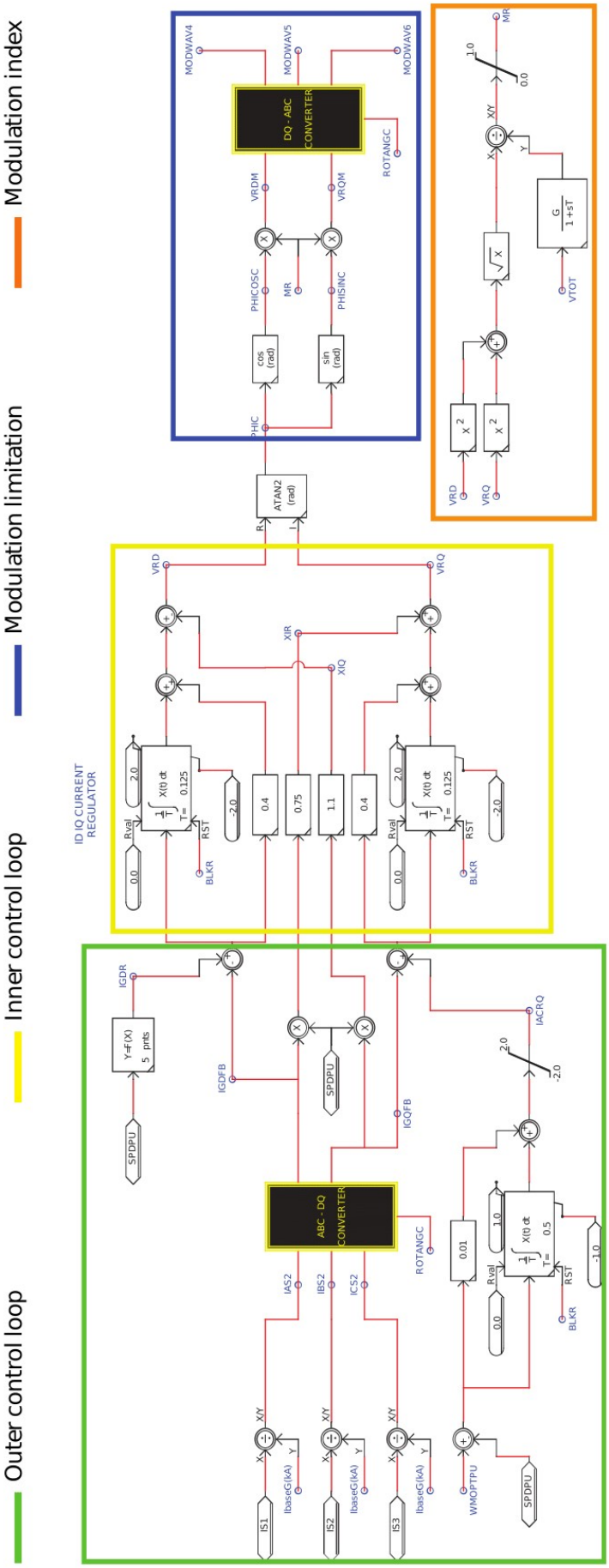

Figure F.1: Control scheme of the MSC in the baseline model [20]

G

GSC Control Scheme in the Case of Electrolyser Connected to the DC Link of the Wind Turbine

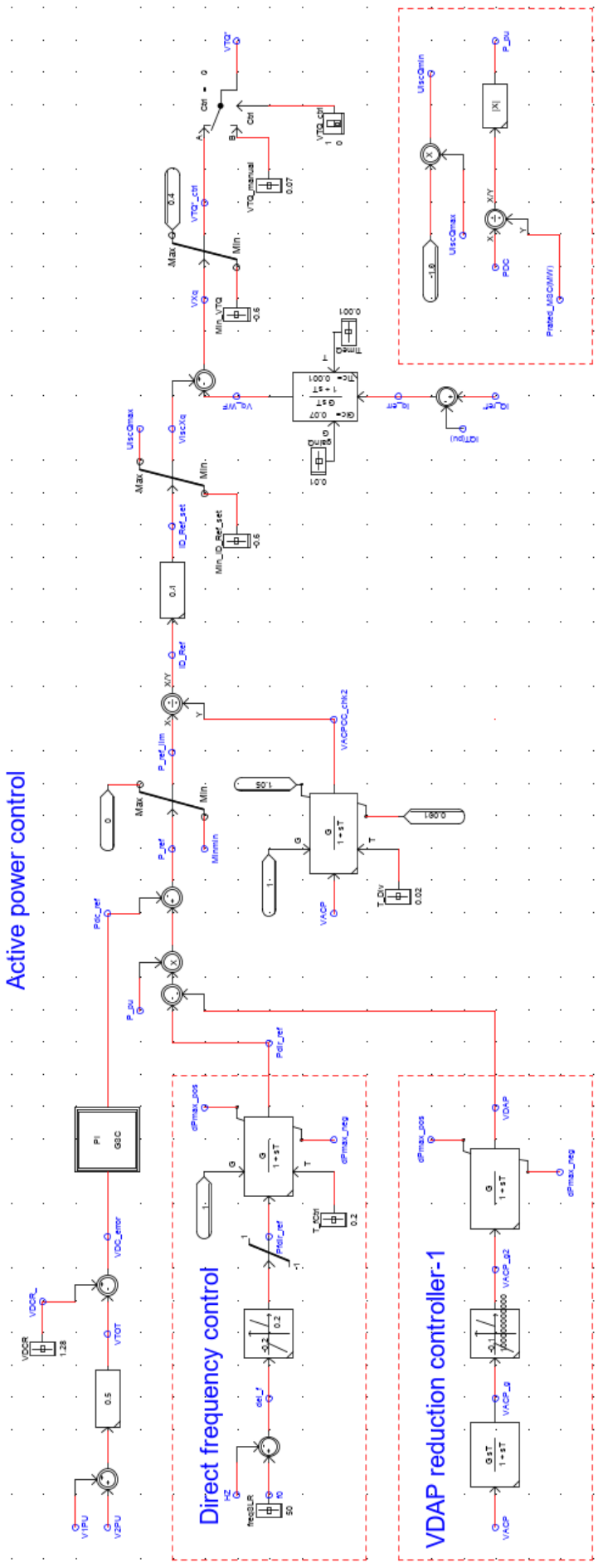

Figure G.1: Adapted control logic for the active power control in the outer loop of the GSC in the case of electrolyser connected to the DC link

Bibliography

[1] United Nations. Paris Agreement. https://unfccc.int/sites/default/files/english_paris_agreement.pdf, 2015. Accessed: 2021-08-03.

[2] North Sea Wind Power Hub. Six concept papers, one storyline. https://northseawindpowerhub.eu/vision/, 2019. Accessed: 2020-12-23.

[3] International Renewable Energy Agency (IRENA). Renewable Energy Statistics 2020. https://irena.org/publications/2020/Jul/Renewable-energy-statistics-2020, 2020. Accessed: 2021-08-03.

[4] S. Few, O. Schmidt, and A. Gambhir. Electrical energy storage for mitigating climate change. Briefing paper, Grantham Institute, 2016.

[5] D. Gulcin Caglayan, N. Weber, H. U. Heinrichs, J. Linßen, M. Robinius, P. A. Kukla, and D. Stolten. Technical potential of salt caverns for hydrogen storage in europe. *International Journal of Hydrogen Energy*, 2019.

[6] G. Kok, M. Renz, M. van Schot, and K. Wouters. North Sea Energy D 3.6 - Towards sustainable energy production on the North Sea - Green hydrogen production and CO2 storage: onshore or offshore ? - As part of Topsector Energy: TKI Offshore Wind & TKI New Gas. Technical Report NSE1-D3.6, New Energy Coalition, 2018.

[7] M. van Schot and C. Jepma. North sea energy - a vision on hydrogen potential from the north sea. Technical Report NSE3-D1.6 D1.7, New Energy Coalition, 2020.

[8] M. Woznicki, G. Le Solliec, and R. Loisel. Far off-shore wind energy-based hydrogen production: Technological assessment and market valuation designs. *Journal of Physics: Conference Series*, 2020.

[9] A. Hassanpouryouzband, E. Joonaki, K. Edlmann, and R. Stuart Haszeldine. Offshore geological storage of hydrogen: Is this our best option to achieve net-zero? *ACS Energy Letters*, 2021.

[10] F. Alshehri, V. García Suárez, J. L. Rueda Torres, A. Perilla, and M. A .M. M. van der Meijden. Modelling and evaluation of PEM hydrogen technologies for frequency ancillary services in future multi-energy sustainable power systems. *Heliyon*, 5(4):e01396, 2019.

[11] ENTSO-E. HVDC Links in System Operations. Technical report, ENTSO-E, Avenue de Cortenbergh 100, 1000 Brussels, Belgium, 2019.

[12] P. K. S. Ayivor. Feasibility of Demand Side Response from Electrolysers to Support Power System Stability. Master's thesis, Delft University of Technology, Delft, NL, July 2018.

[13] A. Singlitico, N.J.B Campion, M. Münster, M. J. Koivisto, N. A. Cutululis, C. J. Suo, K. Karlsson, T. Jørgensen, J. E. Waagstein, and M. F. Bendtsen. *Optimal placement of P2X facility in conjunction with Bornholm energy island: Preliminary overview for an immediate decarbonisation of maritime transport.* Technical University of Denmark, 2020.

[14] P. Mukherjee and V.V. Rao. Superconducting magnetic energy storage for stabilizing grid integrated with wind power generation systems. *Journal of Modern Power Systems and Clean Energy*, 2019.

[15] R. Peters, J. Vaessen, and R. van der Meer. Offshore Hydrogen Production in the North Sea Enables Far Offshore Wind Development. https://doi.org/10.4043/30698-MS, 2020. Accessed: 2021-08-03.

[16] Siemens Gamesa. New era of offshore green hydrogen production unlocked. https://www.siemensgamesa.com/en-int/products-and-services/hybrid-and-storage/green-hydrogen, 2020. Accessed: 2021-05-27.

[17] A. Nauen. Wind industry in the green Hydrogen revolution Siemens - Energy Hydrogen Day. https://www.siemensgamesa.com/en-int/-/media/siemensgamesa/downloads/en/products-and-services/hybrid-power-and-storage/green-hydrogen/210318-siemens-energy-hydrogen-day.pdf, 2021. Accessed: 2021-05-27.

[18] D. van Baarle. Siemens builds electrolyser in offshore wind turbine. https://www.industryandenergy.eu/hydrogen/siemens-builds-electrolyser-in-offshore-wind-turbine/, 2021. Accessed: 2021-06-13.

[19] J. Porst, M. Luther, S. Baumann, and C. Hahn. Energy droop control for mmc based multiterminal hvdc systems. In *2019 IEEE Milan PowerTech*, pages 1–6, 2019.

[20] S. Ganesh. Development of a Generic Model for Real-time Simulation and Assessment of the Dynamic Performance of a Large Scale Offshore Transmission Network. Master's thesis, Delft University of Technology, Delft, NL, October 2020.

[21] P. Tünnerhoff, P. Ruffing, and A. Schnettler. Comprehensive fault type discrimination concept for bipolar full-bridge-based mmc hvdc systems with dedicated metallic return. *IEEE Transactions on Power Delivery*, 33(1):330–339, 2018.

[22] M. Changizian, A. R. Mizani, and A. Shoulaie. Proposed a new voltage rebalancing method for pole-to-ground fault in bipolar two level vsc-hvdc. *IEEE Transactions on Industrial Electronics*, 2021.

[23] A. Jain, O. Saborío-Romano, J. N. Sakamuri, and N. A. Cutululis. Blackstart from HVDC-connected offshore wind: Hard versus soft energization. *IET Renewable Power Generation*, 2021.

[24] Z. Li, R. Zhan, Y. Li, Y. He, J. Hou, X. Zhao, and X. Zhang. Recent developments in hvdc transmission systems to support renewable energy integration. *Global Energy Interconnection*, 2018.

[25] RTDS Technologies. Standardization of Renewable Energy System Modelling, 2020.

[26] G. Lammert, K. Yamashita, L. D. P. Ospina, H. Renner, S. Martınez Villanueva, P. Pourbeik, F-E. Ciausiu, and M. Braun. International industry practice on modelling and dynamic performance of inverter based generation in power system studies. *CIGRE Science & Engineering*, 8:25–37, 2017.

[27] M. Dijokas, DTU. RMS vs EMT: the need for new simulation tools. http://www.multi-dc.eu/wp-content/uploads/2019/09/MatasDijokas_RMSvsEMT-the-need-for-new-simulation-tools.pdf, 2019. Accessed: 2020-12-16.

[28] RTDS Technologies. RTDS website. https://www.rtds.com/, 2020. Accessed: 2020-12-15.

[29] Z. Liu, C. Liu, G. Li, Y. Liu, and Y. Liu. Impact study of pmsg-based wind power penetration on power system transient stability using eeac theory. *Energies*, 2015.

[30] J. L. Rueda Torres, D. Wang. RTDS Training Course of IEPG - DAY 6: MMC and HVDC Example. https://erigrid.eu/wp-content/uploads/2018/10/MMC-and-HVDC-example_Final.pdf, 2018. Accessed: 2021-08-03.

[31] I. Erlich, A. Korai, T. Neumann, M. Koochack Zadeh, S. Vogt, C. Buchhagen, C. Rauscher, A. Menze, and J. Jung. New control of wind turbines ensuring stable and secure operation following islanding of wind farms. *IEEE Transactions on Energy Conversion*, 32(3):1263–1271, 2017.

[32] CIGRE - Working group B4.57. Guide for the Development of Models for HVDC Converters in a HVDC Grid. Technical report, CIGRE, 2014.

[33] C. Thommessen, M. Otto, F. Nigbur, J. Roes, and A. Heinzel. Techno-economic system analysis of an offshore energy hub with an outlook on electrofuel applications. *Smart Energy*, 2021.

[34] TSO2020. Stability Analysis of an International Electricity System connected to Regional and Local Sustainable Gas Systems Final Report. http://tso2020.eu/wp-content/uploads/2020/01/TSO2020_Final_Report_TUD.pdf, 2019. Accessed: 2020-12-24.

[35] B. W. Tuinema, E. Adabi, P. K. S. Ayivor, V. Garcia Suarez, L. Liu, A. Perilla, Z. Ahmad, J.L. Rueda Torres, M. A. M. M. van der Meijden, and P. Palensky. Modelling of large-sized electrolysers for real-time simulation and study of the possibility of frequency support by electrolysers. *IET Generation, Transmission and Distribution*, 2020.

[36] N. Veerakumar, Z. Ahmad, M. E. Adabi, J. R. Torres, P. Palensky, M. van der Meijden, and F. Gonzalez-Longatt. Fast active power-frequency support methods by large scale electrolyzers for multi-energy systems. In *2020 IEEE PES Innovative Smart Grid Technologies Europe (ISGT-Europe)*, pages 151–155, 2020.

[37] A. Ebneali Samani, A. D'Amicis, J. De Kooning, D. Bozalakov, P. Silva, and L. Vandevelde. Grid balancing with a large-scale electrolyser providing primary reserve. In *8th Renewable Power Generation Conference (RPG 2019)*, pages 1–7, 2019.

[38] J. Eichman, K. Harrison, and M. Peters. Novel Electrolyzer Applications: Providing More Than Just Hydrogen. Technical Report NREL/TP-5400-61758, National Renewable Energy Laboratory, National Renewable Energy Laboratory 15013 Denver West Parkway Golden, CO 80401, September 2014.

[39] J. Kee, M. Renz, M. van Schot, F. Howell, C. Jepma, and H. van Maanen. North sea energy - energy transport and energy carriers. Technical report, New Energy Coalition, 2020.

[40] F. Deng, D. Liu, Z. Chen, and P. Su. Control strategy of wind turbine based on permanent magnet synchronous generator and energy storage for stand-alone systems. *Chinese Journal of Electrical Engineering*, 2017.

[41] M. Y. Worku and M. A. Abido. Fault ride-through and power smoothing control of pmsg-based wind generation using supercapacitor energy storage system. *Arabian Journal for Science and Engineering*, 2019.

[42] RTDS Technologies. Real Time Digital Simulation for the Power industry - Manual Set. RTDS library, 2020.

[43] A. Ostadrahimi and A. Radan. Utilization of interleaved converter to improve battery performance in electric and electrical hybrid vehicles. In *The 5th Annual International Power Electronics, Drive Systems and Technologies Conference (PEDSTC 2014)*, pages 624–628, 2014.

[44] RTDS Technologies Inc. The New Universal Converter Model - a Revolution in Real-Time Power Electronics Simulation (Webinar recording). https://www.youtube.com/watch?v=6WGYHhiZg2k, 2021. Accessed: 2021-07-25.

[45] A. Zama, A. Benchaib, S. Bacha, D. Frey, and S. Silvant. High dynamics control for mmc based on exact discrete-time model with experimental validation. *IEEE Transactions on Power Delivery*, 33(1):477–488, 2018.

[46] A. Perez, B. C. Karatas, H. Jóhannsson, and J. Østergaard. Considering wind speed variability in real-time voltage stability assessment using thévenin equivalent methods. In *2017 IEEE Manchester PowerTech*, pages 1–6, 2017.

[47] W. Wu, Z. Lin, Y. Sun, X. Wang, M. Huang, H. Wang, and H. S. Chung. A hybrid damping method for llcl-filter based grid-tied inverter with a digital filter and an rc parallel passive damper. In *2013 IEEE Energy Conversion Congress and Exposition*, pages 456–463, 2013.

[48] M. Cespedes, L. Xing, and J. Sun. Constant-power load system stabilization by passive damping. *IEEE Transactions on Power Electronics*, 26(7):1832–1836, 2011.

[49] M. Büyüka, A. Tana, M. Tümaya, and K. Ç. Bayındır. Topologies, generalized designs, passive and active damping methods of switching ripple filters for voltage source inverter: A comprehensive review. *Renewable and Sustainable Energy Reviews*, 2016.

[50] L. Michi et al. System dynamic behaviour challenges: operating experience and future trends. *2019 AEIT HVDC International Conference (AEIT HVDC)*, 2019.

[51] Siemens AG. High Voltage Direct Current Transmission – Proven Technology for Power Exchange. Technical Report E50001-U131-A92-V2-7600, Siemens AG, Power Transmission and Disttribution High Voltage Division Pstfach 3220 91050 Erlangen Germany, 2011.

[52] R. Mourouvin, K. Shinoda, J. Dai, A. Benchaib, S. Bacha, and D. Georges. Ac/dc dynamic interactions of mmc-hvdc in grid-forming for wind-farm integration in ac systems. In *2020 22nd European Conference on Power Electronics and Applications (EPE'20 ECCE Europe)*, pages P.1–P.9, 2020.

[53] R. Irnawan. *Planning and control of expandable multi-terminal VSC-HVDC transmission systems*. PhD thesis, Aalborg University Denmark, 2018.

[54] D. Gómez Acero, M. Cheah-Mane, J. D. Páez, F. Morel, O. Gomis-Bellmunt, and P. Dworakowski. Dc-MMC for the interconnection of HVDC grids with different line topologies. *IEEE Transactions on Power Delivery*, 2021.

[55] A. Bemporad, University of Trento. Automatic Control 2 - Lecture slides - Anti-windup techniques. http://cse.lab.imtlucca.it/~bemporad/teaching/ac/pdf/AC2-09-AntiWindup.pdf, 2010. Accessed: 2021-06-21.